

## INFORMATION TO USERS

This manuscript has been reproduced from the microfilm master. UMI films the text directly from the original or copy submitted. Thus, some thesis and dissertation copies are in typewriter face, while others may be from any type of computer printer.

**The quality of this reproduction is dependent upon the quality of the copy submitted.** Broken or indistinct print, colored or poor quality illustrations and photographs, print bleedthrough, substandard margins, and improper alignment can adversely affect reproduction.

In the unlikely event that the author did not send UMI a complete manuscript and there are missing pages, these will be noted. Also, if unauthorized copyright material had to be removed, a note will indicate the deletion.

Oversize materials (e.g., maps, drawings, charts) are reproduced by sectioning the original, beginning at the upper left-hand corner and continuing from left to right in equal sections with small overlaps. Each original is also photographed in one exposure and is included in reduced form at the back of the book.

Photographs included in the original manuscript have been reproduced xerographically in this copy. Higher quality 6" x 9" black and white photographic prints are available for any photographs or illustrations appearing in this copy for an additional charge. Contact UMI directly to order.

# UMI

A Bell & Howell Information Company  
300 North Zeeb Road, Ann Arbor MI 48106-1346 USA  
313/761-4700 800/521-0600



**THE UNIVERSITY OF TULSA  
THE GRADUATE SCHOOL**

**HEAT TRANSFER ENHANCEMENT BY STRUCTURED  
TURBULENCE PROMOTERS**

**BY  
Martin de Tezanos Pinto**

**A dissertation submitted in partial fulfillment of  
the requirements for the degree of Doctorate of Philosophy  
in the Discipline of Chemical Engineering  
The Graduate School  
The University of Tulsa  
1997**

**UMI Number: 9723746**

---

**UMI Microform 9723746  
Copyright 1997, by UMI Company. All rights reserved.**

**This microform edition is protected against unauthorized  
copying under Title 17, United States Code.**

---

**UMI**  
300 North Zeeb Road  
Ann Arbor, MI 48103

**THE UNIVERSITY OF TULSA**  
**THE GRADUATE SCHOOL**

**HEAT TRANSFER ENHANCEMENT BY STRUCTURED  
TURBULENCE PROMOTERS**

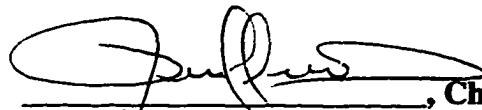

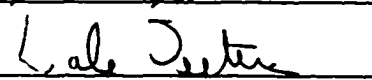

**BY**  
**Martin de Tezanos Pinto**

**A DISSERTATION**

**APPROVED FOR THE DISCIPLINE OF  
CHEMICAL ENGINEERING**

!

**By Dissertation Committee**

  
\_\_\_\_\_, Chairperson  
  
\_\_\_\_\_  
  
\_\_\_\_\_  
  
\_\_\_\_\_

## **ABSTRACT**

de Tezanos Pinto, Martin ( Doctorate of Philosophy in Chemical Engineering )

Heat Transfer Enhancement by Structured Turbulence Promoters. ( 120 pp. – Chapters 5 )

Directed by Professor Ramon L. Cerro

( 324 words )

The enhancement of heat transfer in pipes is relevant to the improvement of performance of cooling or heating devices. The enhancement of heat transfer can be achieved by inclusion of structured promoters in the inside walls of a pipe. Experiments were carried out on industrial pipes provided by a manufacturing company. The type of structured promoters of these pipes were helicoidal ribs. Velocity profiles were measured for both air and water flow using a Laser Doppler velocimeter. The turbulence intensity of air and water flow was measured close to the pipe wall. The temperature profiles on top of the ribbed surface were determined using liquid crystal thermography. The results from the liquid crystal thermography experiments were used in the computation of local heat transfer coefficients on the internal walls of the pipes. The average heat transfer coefficient was calculated for the pipes through integration of the local heat transfer coefficient profiles. The local heat transfer coefficient profiles were analyzed as a combination of two separate phenomena. One section of these profiles was treated as a developing boundary layer. The other section was treated as a cavity flow. The local heat transfer coefficients corresponding to the boundary layer section were correlated to the theory of boundary layer flow. The results of the cavity section were compared with experimental correlations for cavity flow done by previous researchers. The two correlations for boundary layer and cavity flow were put together to define a correlation for the average heat transfer coefficient. The correlation for the average heat transfer coefficient was compared with the experimental results and with results obtained on different pipe models that were provided by the pipe manufacturers. The distribution of friction factors on the pipe was also calculated using

the velocity profiles of the Laser Doppler Velocimetry experiments. The results were analyzed in the same fashion as the local heat transfer coefficients. Two correlations were developed to define the friction factor at the cavity and at the boundary layer region. These two correlations were put together to define the average friction factor in the internal ribbed surface of the pipes. The correlation for friction factor were compared with the smooth pipe correlations and the experimental frictions factors obtained by Laser Doppler velocimetry.



### **ACKNOWLEDGEMENTS**

I would like to thank my advisor, Prof. Ramon Cerro, for all his assistance and guidance. Special thanks to Prof. Ursula Bhom de Bordenave and Prof. Analea Kukierman to whom I owe pursuing graduate studies in U.S.A. Also I would like to thank Prof. Ovadia Shoham, Prof. Dale Teeters and Prof. Martin Abraham. I am also thankful to FINTUBE ltd. Oklahoma and OCAST that provided the necessary financial assistance during this research.

Many thanks to my friends, William Redman, Terry Hudson, Alec Klinhoffer, Sanat Shetty, Luis Smitter, Mike Teal, Mariano Savelski and Federico Papa.

I would like to express my love and endless thanks to the people who mean the most to me: mis viejos, Manuel and my beloved wife, Peggy.



## TABLE OF CONTENTS

	<b>Page</b>	
<b>TITLE PAGE</b>	<b>i</b>	
<b>APPROVAL PAGE</b>	<b>ii</b>	
<b>ABSTRACT</b>	<b>iii</b>	
<b>ACKNOWLEDGEMENTS</b>	<b>v</b>	
<b>TABLE OF CONTENTS</b>	<b>vi</b>	
<b>LIST OF FIGURES</b>	<b>viii</b>	
<b>CHAPTER I</b>	<b>INTRODUCTION</b>	<b>1</b>
	IA Motivation	1
	IB Previous Work	3
	IC Cavity Flow	11
	References	14
<b>CHAPTER II</b>	<b>FUNDAMENTALS</b>	<b>15</b>
	IIA Design Variables	15
	IIB Dimensional Analysis	20
	IIC Developing Boundary Layer	25
	IID Smooth and Rough Pipe Flow	32
<b>CHAPTER III</b>	<b>EXPERIMENTAL TECHNIQUES AND RESULTS</b>	<b>36</b>
	IIIA Experimental Setup	36
	IIIA.1 Water Loop	36
	IIIA.2 Air Loop	38
	IIIB Local Heat Transfer Coefficients	39
	IIIB.1 Liquid Crystals Technique	39
	IIIB.2 Computational Analysis	45

	<b>IIIB.3 Average Heat Transfer Coefficients</b>	58
	<b>IIIC Laser Doppler Velocimetry</b>	59
	<b>IIIC.1 Laser Doppler Technique</b>	59
	<b>IIIC.2 Axial Velocities</b>	65
	<b>IIIC.3 Turbulence Intensities</b>	76
	<b>IIIC.4 Pressure Drop</b>	82
	<b>References</b>	85
<b>CHAPTER IV</b>	<b>ANALYSIS OF RESULTS</b>	86
	<b>IVA Heat Transfer Coefficients</b>	88
	<b>IVA.1 Heat Transfer on Boundary Layer</b>	88
	<b>IVA.2 Heat Transfer on Cavity Surface</b>	93
	<b>IVA.3 Average Heat Transfer Coefficients</b>	97
	<b>IVB Analysis on Friction Factors</b>	105
<b>CHAPTER V</b>	<b>CONCLUSIONS AND RECOMMENDATIONS</b>	120

## LIST OF FIGURES

<b>Figure</b>	<b>Page</b>
IIA.1 Geometry	16
IIA.2 Repeating Units	19
IID.1 Nikuradse's experiments	34
IIIA.1.1 Water Loop	37
IIIA.2.1 Air Loop	38
IIIB.1.1 Heating Block	41
IIIB.1.2 Temperature Profiles	43
IIIB.1.3 Piecewise Temperature Profiles	44
IIIB.2.2 Heating Block Computations	46
IIIB.2.3 Heating Block Contour Plots	48
IIIB.2.4 Heat Fluxes Results	49
IIIB.2.5 Repeating Unit Simulation	50
IIIB.2.6 Smooth vs. Piecewise Approach	54
IIIB.2.7 Local Heat Transfer Coefficients	55
IIIB.2.8 Local Heat Transfer Coefficients	56
IIIB.2.9 Local Heat Transfer Coefficients	57
IIIB.3.1 Average Heat Transfer Coefficients	58
IIIC.1.1 Laser Doppler Setup	60
IIIC.1.2 Mapping	62
IIIC.1.3 Pamperito Cyclone	64
IIIC.2.1 Axial Velocity	66
IIIC.2.2 Axial Velocity	67
IIIC.2.3 Axial Velocity	68
IIIC.2.4 Axial Velocity	69
IIIC.2.5 Axial Velocity	70
IIIC.2.6 Axial Velocity	71
IIIC.2.7 Axial Velocity	72

III.C.2.8 Axial Velocity	73
III.C.2.9 Axial Velocity	74
III.C.2.10 Axial Velocity	75
III.C.3.1 Axial Velocity	77
III.C.3.2 Axial Velocity	78
III.C.3.3 Axial Velocity	79
III.C.3.4 Axial Velocity	80
III.C.3.5 Axial Velocity	81
III.C.4.1 Pressure Drop	82
III.C.4.2 Pressure Drop	83
III.C.4.3 Pressure Drop	84
IV.1 Reattachment Point	86
IV.2 Separation of Regions	88
IVA.1.1 Boundary Layer Log. Plot	91
IVA.1.2 Boundary Layer Linear Plot	92
IVA.2.1 Cavity Log. Plot	95
IVA.2.2 Cavity Linear Plot	97
IVA.2.3 Heat Transfer Coefficients Correlation	98
IVA.2.4 Heat Transfer Coefficients Correlation	99
IVA.2.5 Heat Transfer Coefficients Correlation	100
IVA.2.6 Average Coefficients Correlation	103
IVA.2.7 Average Coefficients Correlation	104
IVB.1 U* Correction Mechanism	106
IVB.1.1 Average Coefficients Correlation	108
IVB.1.2 Average Coefficients Correlation	109
IVB.1.3 Average Coefficients Correlation	110
IVB.1.4 Average Coefficients Correlation	111
IVB.1.5 Average Coefficients Correlation	112
IVB.1.6 Average Friction Factor	113

# I INTRODUCTION

## IA Motivation

Since the mid nineteen thirties one of the main concerns in the design of heat transfer equipment was the relationship between size and performance. Equipment like heat exchangers, burners or reboilers are typical examples in which the idea of reducing size and improving performance is always present. Most commonly this type of equipment involves flow through pipes. The augmentation of heat transfer through pipe walls can be approached in many different ways.

Increasing flow rate increases the amount of heat that is exchanged through the pipe wall. This procedure has obvious limitations and in many cases the maximum flow rates attainable are not enough to achieve the desired amount of heat transfer enhancement. Increasing the length of the pipe, however, causes an increase in pressure drop and reduces the efficiency of the process. Heat transfer rates are higher but it requires more pumping energy, sometimes up to impractical levels. There is another alternative to enhance heat transfer through the walls of a pipes. It consist of changing the flow characteristics. It is known that laminar flows are much less efficient heat transfer wise than those that are turbulent. The flow regime can be changed either increasing the kinetic energy of the flow ( increasing velocity ) or introducing a certain perturbation in the pipe that might prevent the development of laminar flow.

Within the turbulent regime, pressure losses due to form drag are many times larger pressure losses due to viscous forces. As a consequence it is possible , at least from a theoretical standpoint, to introduce perturbations that will increase heat transfer and viscous momentum transfer without increasing ( perhaps reducing ) pressure losses. The capability of perturbations to increase heat transfer rates in a pipe was first noticed when the steam machines started being used at the beginning of this century. Then, it was observed that after cleaning the interior of the

pipes of a boiler and removing sediments and rust from the pipe walls, the boiler would exchange more heat than when it was brand new. The new equipment had smooth pipes newly cast that promoted the existence of laminar flow within them. The rusted and cleaned pipes had imperfections like bumps and dimples in the interior walls that promoted the necessary perturbations for turbulent flow to exist. The relationship between turbulence and heat transfer augmentation was extensively explored in the past.

The type of perturbations that can produce turbulence and heat transfer augmentation can be divided in two : a) Random Roughness: this are the type of turbulence promoters like the ones created by corrosion. It consist of a random distribution of imperfections in the internal pipe walls. The fluid dynamics of this type of pipes was extensively studied by Nikuradse( 1933 ). Nikuradse measured the friction factors at different  $N_{Re}$  of pipes with different degree of random roughness. He called this type of roughness 'sand grain roughness' because of the relative size,  $\epsilon$  , with respect to the pipe diameter ,  $D$  , and the random distribution of the perturbations. b) Structured Promoters: this wide classification group addressed those turbulence promoters with defined geometrical shape and displayed on the pipe walls in an organized manner. Examples of these promoters are sequences of ribs, circular dimples, small strings of bumps or pegs. The diversity of structured promoters in shape and size, can go as far as imagination can go. Although the structured promoters are well proven to be a good device to enhance heat transfer, the physical reasons of the augmentation ar not too clear.

The goal of the present work is to understand the fundamentals of heat transfer augmentation by structured promoters. Heat transfer and fluid dynamics of industrial 'internally ribbed' pipes were analyzed. The results were explained with existing models and theory. The equations that relate flow, design and heat transfer were developed from experimental data an theoretical background. From information learned about the fundamentals of the phenomenon

of heat transfer augmentation by structured promoters, an optimization mechanism was proposed for pipe design.

### IB Previous works

Nikuradse ( 1926 ) extensively studied the dependency of friction factors with flow rate and roughness distribution . He introduced the concept of relative roughness  $\epsilon / D$  , that relates the internal diameter of the pipe,  $D$ , with the average roughness height ,  $\epsilon$  . The results of Nikuradse are usually shown in the Moody( 1944 ) charts of friction factors vs  $N_{Re}$ .

One of the first works done on heat transfer of rough pipes was the one of Dipprey and Sabersky ( 1963 ) . The purpose of Dipprey's thesis was to extend to heat transfer the work of Nikuradse to pipes of commercial roughness. He found that increasing heat transfer coefficient were generally followed by large increases in friction factors,  $f$ . However he found an exception to this behavior for high Prandtl numbers in the transition region from smooth to fully rough of the friction factor. A complete development of equations of this paper is described because of this being the first attempt to correlate turbulence with heat transfer enhancement :

The authors define:

$$f = \frac{\pi^2 D^5 \rho \Delta P}{32 \dot{w}^2} \quad \text{Friction factor}$$

$$C_H = \frac{\dot{q}_0}{\rho \langle u \rangle C_p \Delta T_{ln}} \quad \text{Stanton Number}$$

$\dot{w}$ :	mass flow rate	$C_p$ :	fluid heat capacity
$D$ :	internal diameter	$\rho$ :	fluid density
$\Delta P$ :	pressure drop in test section	$T_{bi}$ :	fluid temperature at point ,i.
$T_w$ :	tube wall temperature	$\dot{q}_0$ :	heat flux through the wall

$$\Delta T_{ln} = \frac{T_w - T_{b1} - T_w - T_{b2}}{\ln\left(\frac{T_w - T_{b1}}{T_w - T_{b2}}\right)} \quad C_H = \frac{h_{loc}}{\rho C_p \langle u \rangle}$$

For the velocity profile in the transition and core region :

$$U^+ = \frac{u}{U^*} = \frac{1}{k_1} \ln(y^+) + k \quad \text{IB.1}$$

$$y^+ = \frac{yU^*}{\nu} \quad U^* = (\tau_w)^{\frac{1}{2}}$$

$$U^* = \langle u \rangle \left(\frac{f}{2}\right)^{\frac{1}{2}} \quad \text{IB.2}$$

For the fully rough region:

$$U^+ = \frac{u}{U^*} = \frac{1}{k_1} \ln\left(\frac{y}{e}\right) + k \quad \text{IB.3}$$

Combining IB.2 and IB.3 at  $y = D/2$  :

$$\left(\frac{2}{f}\right)^{\frac{1}{2}} = -B \ln\left(\frac{2e}{D}\right) + A(\epsilon^*) \quad \text{IB.4}$$

$$\epsilon^* = \frac{eU^*}{\nu} \quad \text{IB.5}$$

Combining IB.4 with IB.2 :

$$\frac{2e}{D} = \frac{2\epsilon^*}{N_{Re}\left(\frac{f}{2}\right)^{\frac{1}{2}}} \quad \text{IB.6}$$



Combining IB.4 with IB.6 :

$$\left(\frac{2}{f}\right)^{\frac{1}{2}} = -B \ln \left( \frac{2\epsilon^*}{N_{Re} \left(\frac{f}{2}\right)^{\frac{1}{2}}} \right) + A(\epsilon^*) \quad \text{IB.7}$$

The total turbulent transport of heat and momentum :

$$\tau_w^{(t)} = (\mu + \mu^{(t)}) \frac{du}{dy} \quad q_w^{(t)} = - (k + k^{(t)}) \frac{d\bar{T}_b}{dy}$$

Assuming that  $\tau_w$  is a linear function of distance from the wall:

$$\frac{\tau_0}{\rho} \left(1 - \frac{2y}{D}\right) = (v + v^{(t)}) \frac{du}{dy} \quad \frac{\dot{q}_0}{\rho C_p} \left(1 - \frac{2y}{D}\right) = \left(\frac{v}{N_{Pr}} + \alpha^{(t)}\right) \frac{d\bar{T}_b}{dy} \quad \text{IB.8}$$

Assuming the validity of :

$$u = U^* \left( \frac{1}{k_1} \ln(y^+) + k \right) \quad \text{in the core region}$$

$$u = U^{*2} \left( \frac{y}{\nu} \right) \quad \text{in the viscous sublayer}$$

Then :

$$\frac{v^{(t)}}{v} = \mathfrak{S}_1 \left( \frac{yU^*}{\nu}; \frac{eU^*}{\nu} \right) \quad \text{IB.9}$$

The Reynolds analogy is valid :

$$\alpha^{(t)} = v^{(t)} \Rightarrow N_{Pr} = \frac{v^{(t)}}{\alpha^{(t)}} = \frac{\delta_m}{\delta_T} = 1 \quad \text{IB.10}$$

This last equation means that the momentum and thermal boundary layer have the same thickness. Applying the two definitions of  $C_H$  :

$$\frac{1}{C_H} = \frac{\rho C_p \langle u \rangle}{\dot{q}_0} (T_w - T_2) + \frac{\rho C_p \langle u \rangle}{\dot{q}_0} (T_2 - \bar{T}_b) \quad \text{IB.11}$$

Where  $T_2$  is the temperature of a point  $y_2$  where stresses are negligible.

From the distribution of stresses IB.8 :

$$\frac{\rho C_p \langle u \rangle}{\dot{q}_0} (T_2 - \bar{T}_b) = \frac{2}{f} + \frac{u_2}{U^* \left(\frac{f}{2}\right)^{\frac{1}{2}}} \quad \text{IB.12}$$

$$\rho C_p \frac{\langle u \rangle}{\dot{q}_0} (T_w - T_2) = \frac{\langle u \rangle}{U^*} \mathcal{F}_3 (y_2^*, \epsilon^*, N_{Pr}) \quad \text{IB.13}$$

Combining IB.12 and IB 13 :

$$\frac{\left(\frac{f}{2C_H}\right) - 1}{\left(\frac{f}{2}\right)^{\frac{1}{2}}} = g(\epsilon^*, N_{Pr}) - A(\epsilon^*) \quad \text{IB.14}$$

Equation IB.14 is still valid for the smooth pipe. In the limit of  $\epsilon^* \rightarrow 0$  :

$$\frac{2C_H}{f} = (N_{Pr})^{\frac{2}{3}} \quad \text{IB.15}$$

Equation IB.15 is the result for smooth pipes predicted by Colburn ( 1933 ). The authors found that  $C_H$  increases with the  $N_{Re}$  in the transition region reaching a maximum near the limit of the fully rough region. Increasing  $N_{Re}$  causes  $C_H$  to decrease monotonically within the fully rough regime. His results are analogous to Nikuradse's. He also shows that the relation between friction and heat transfer can be described by IB.14, showing that this equation is a continuous function at a constant  $N_{Pr}$ .

Webb, Eckert and Goldstein ( 1971) analyzed friction and heat transfer in pipes with repeated rib roughness. The authors extend the results of Dipprey and Sbersky in sand grain roughness to structured turbulence promoters. In this work the most important statement is that repeated-rib roughness may be viewed ( unlike random roughness ) as a problem of boundary layer separation and reattachment. Webb's work showed a collection of flow patterns for different types of rib separation ( pitch ,P ). It pointed out that heat transfer has a maximum in

the vicinity of the reattachment point of the boundary layer. An integral method is used to find an expression for the right hand side of eq. IB.14 :

$$\frac{\left(\frac{f}{2C_H}\right) - 1}{\left(\frac{f}{2}\right)^{\frac{1}{2}}} + U^+_e = g\left(\epsilon^*, \frac{P}{e}\right) \mathcal{F}(N_{Pr}) \quad \text{IB.16}$$

Where :

$$U^+_e = \left(\frac{2}{f}\right)^{\frac{1}{2}} + 2.5 \ln\left(\frac{2e}{D}\right) + 3.75 \quad \text{IB.17}$$

Equation IB.17 is the friction similarity law with  $e =$  rib height.

The variable  $P/e$  is the pitch, or rib separation, divided by the rib height. Equation IB.16 shows the extension of the work of Dipprey and Sabersky on sand grain roughness to a physically defined perturbation like a rib. The correlation is purely experimental however the velocity profiles reported in this work are clarifying of what can be expected for the flow in a ribbed pipe.

Han, Glicksman and Rohsenow ( 1978 ) analyzed the problem of heat transfer and friction factor on ribbed surfaces. This is the first comprehensive paper on helicoidal rib-roughened surfaces, although the experiments were carried out on a parallel plate channel. This paper introduces the concept of angle of attack ( angle of the ribs with respect to the pipe axis ). Also pitch and rib height ratio are analyzed. Instead of using eq. IB.17 the authors find an empirical correlation for the roughness Reynolds number:

$$U^+_e = \frac{4.9\left(\frac{\epsilon^*}{35}\right)^m}{\left(\frac{\phi}{90}\right)^{0.35} \left(10\frac{e}{P}\right)^n \left(\frac{\alpha}{45}\right)^{0.57}} \quad \text{IB.18}$$

$\alpha$  : angle of attack of the ribs.                       $\phi$  : rib shape factor

$m$ , and  $n$ , are calculated experimentally.

In Eq.IB.18 is also included the rib shape in the variable  $\phi$ . This variable is the rib shape angle in degrees. Han et al. calculate the values of the function ,g , on the right hand side of eq. IB.16 using IB.18:

$$g(\epsilon^*) = 8 \left(\frac{\epsilon^*}{35}\right)^i \left(\frac{45}{\alpha}\right)^j \quad \text{IB.19}$$

Where i and j are also calculated experimentally. The authors report to find better heat transfer for a 45° angle of attack than the 90° attack angle. The authors object the work of Webb et al. showing that Webb's correlation breaks down for values of  $P/e < 10$  ( e = rib height ). With respect to friction the authors discuss the concept of geometrical similarity : “ two surfaces are said to have geometrically similar roughness if the geometry of their roughness is the same in all aspects except for a scale factor”. They sustain that keeping angle of attack, rib–shape and  $P/e$  constant, and changing  $e/D$  implies geometrically similar roughness. This statement is a straightforward way to say that the geometry problem can be scaled. The present work strongly disagree with this statement. The phenomenon of heat transfer augmentation with turbulence promoters depends more on the scale of turbulence than on the geometry scale .

An extension of the work done by Han et al. is the paper of Gee and Webb ( 1980 ). This work consisted in a refinement of the correlations outlined by Dipprey and Sabersky ( 1963 ) applied to helically ribbed tubes. It follows the same approach than Dipprey and Sabersky to calculate the an expression for , g, including the attack angle  $\alpha$  in Eq.IB.14 :

$$g(\epsilon^*, N_{Pr}) = \frac{\left(\frac{f}{2C_H}\right) - 1}{\left(\frac{f}{2}\right)^{\frac{1}{2}}} \left(\frac{\alpha}{50}\right)^j \quad \text{IB.20}$$

$$j = 0.37 \text{ for } \alpha < 50^0 \quad j = 0.37 \text{ for } \alpha < 50^0$$

$$g(\epsilon^*, N_{Pr}) = 4.5(\epsilon^*)^{0.28} N_{Pr}^{0.57} \quad \text{IB.21}$$

It reports the results for three rib angles ( 30, 40 and 70 degrees ) in circular tubes and air flow. It is the first work that reports data of circular helically ribbed tubes. Webb uses the same approach of his early work and credits Nikuradse with the roughness function correlation and Dipprey and Sabersky with the heat transfer similarity law. The paper states that better performance is achieved with a 45 degree helix than with 90 degree transverse rib. The final product of this paper is an improved correlation that permits performance prediction for any  $e/D$ . It introduce for the first time the roughness Reynolds number as an optimization parameter. The author establishes that the highest heat transfer performance with minimum friction penalty occurs for values of  $\epsilon^*$  close to 20. This is the transition region from smooth to fully rough according to Nikuradse's experiments. It is interesting the fact that the present work has been performed within this transitional region.

Finally the paper of Nakayama ( 1983 ) also analyze the case of friction and heat transfer of helicoidal ribs in tubes. In this work friction factors and heat transfer coefficients are measured for air and water flow. The helix angles were studied from 0 to 80 degrees and the  $P/e$  ratio from 6.57 to 26.3. The correlation of Webb et al. is verified for helix angles less than 45 degrees and larger than 60. For helix angles between this range other correlations are proposed. This work also introduces the statement that, hydraulically smoothness or transition might not only depend only on  $\epsilon^*$  but also on the  $P/e$  ratio and the rib shape. This concept goes back to the scaling

problem anticipating somehow that the scale of turbulence may be the ruling variable in the phenomenon of heat transfer enhancement. It proposes for future investigations the analysis of the parameter that could define unequivocally smooth and rough regime. Nakayama et al. use eq.IB.16 and 17 to derive a correlation for  $g(\epsilon^*, P/e)$  and  $U^+_e$ :

$$\theta > 60^\circ \quad U^+_e = 4.5 + 5.63 \times 10^{-4} (P/e)^{2.59} \ln(\epsilon^*) \quad \text{IB.22}$$

$$\theta < 45^\circ \quad U^+_e = 5.02 \epsilon^{*0.5} (\theta/45)^{-0.16} \left( \frac{P \sin(\theta)}{e} \right)^{0.1} \quad \text{IB.23}$$

$$45^\circ < \theta < 60^\circ \quad U^+_e = 5.14 \epsilon^{*0.12} (\theta/45)^{-0.8} \left( \frac{P \sin(\theta)}{e} \right)^{0.1} \quad \text{IB.24}$$

The application of these equations to IB.16 yielded the correlations for  $g(\epsilon^*, P/e)$ :

$$45^\circ < \theta < 60^\circ \quad g(\epsilon^*, N_{Pr}) = 4.9(\epsilon^*)^{0.37} N_{Pr}^{0.57} \quad \text{IB.25}$$

$$\text{otherwise} \quad g(\epsilon^*, N_{Pr}) = 4.5(\epsilon^*)^{0.28} N_{Pr}^{0.57} \quad \text{IB.26}$$

Equation IB.26 is identical to Webb et al. IB.16. Another important variable of the structured promoters is the rib shape. One of the best publications on the subject is the one of Hijikata and Mori (1987). Arc, wing and square shape ribs are studied in this work for air flow in a rectangular channel. The values of local velocities and turbulence intensities are reported along the shape of these different ribs. It is a very interesting work because it is one of the first done using non-invasive measuring techniques. In particular, a two dimensional laser Doppler was used to analyze the flow. The results of Hijikata et al. show that the more efficient shape,

with respect to friction factor, was the wing shape. Heat transfer performance is also reported showing that the arc shape has the same heat transfer performance as the other shapes but has the lowest pressure loss. The wing shape is also analyzed in a circular tube flow. It is also reported that the local heat transfer coefficients are closely related to the magnitude of the Reynolds's stresses. This publication emphasizes again the results of Webb et al. , but has very little value from the theoretical point of view.

### IC Cavity Flow

The topic of cavity flow is treated separately because of the importance to the present work. The space that is confined between two ribs can be considered, *a priori*, to be a cavity. This assumption will be extensively explored along the following chapters. A cavity is a flat surface confined to two vertical walls. One of the publications most relevant to our work on cavity flow is the one of Seban ( 1965 ). Seban analyzes flow and heat transfer on a rectangular shallow cavity. He studies the existence of the free shear layer that separates the cavity flow from the main stream. It assumes that the phenomenon can be described by a two dimensional model and that the vertical and horizontal walls of the cavity can be studied separately. In this work the free shear layer developing a part from the point of separation of the boundary layer is treated by analogy with a free jet. For this purpose Seban, refers his analysis to a previous work carried out by Abramovich ( 1963 ). Abramovich presents a solution of the flow down stream of a step. With respect to heat transfer, Seban, makes an analogy between his work and the turbulent flow over a flat plate studied by Colburn ( 1933 ). Seban assumes that the recirculation that occurs in the cavity produces a back flow right on top of the wall of the horizontal face of the cavity. The author treats this flow like a turbulent boundary layer with a considerable success in his predictions of local heat transfer coefficient. Although empirical, this publication opened the

door for a rationalized description of the local heat transfer coefficient on structured promoters. Seban's correlation for cavity flow will be discussed in more detail in Chapter IV. Following the publication of Seban is Lewis' research ( 1965 ).

In this work, Lewis, approaches the problem of a structured promoter analyzing it separately. He considers that the flow on top of a ribbed surface can be explained separately: a) a developing boundary layer on the surface on top of the ribs and b) a cavity similar to Seban's between each pair of ribs. He considers the model of shear flow on top of the structured promoters to be a series of attachments and separations of the boundary layer. He develops a model for both the boundary layer and the cavity flow in a somehow crude fashion. The paper lacks experimental data to verify his approach, and this is the only objection that can be made for this paper. The most important concept elaborated in Lewis work is the separation of the flow on top of a ribbed surface into two distinct regions. This line of thought will be crucial for all the matters that will be discussed in the present work. Lewis also distinguishes between the cases of large and small values of pitch. He proposes three different types of flow according to the value of  $P$ . a) for small values of  $P$  he assumes that the flow will be confined within the ribs to a small recirculating flow. b) an intermediate case in which the boundary layer on top of the rib separates and reattaches on the edge of the down stream rib. c) for large values of  $P$ , the flow reattaches on the valley between the ribs and two zones of recirculation are found. One is the one behind the first rib and the other is the one in front of the down stream rib. It would be fair to say that Lewis' work was one of the most inspiring publications for the present work. It suggested the idea of independent analysis of flow as well as the approaches to attack each individual problem. The present work could be considered an input of very accurate local measurements on top of ribbed surfaces and an extension and generalization of Lewis' ideas.



## **REFERENCES**

- Abramovich, G., **The theory of Turbulent Jets**. *Masachusetts Institute of Technology Press*, ( 1963 ).
- Colburn, A. P., **A Method of Correlating Forced Convection Heat Transfer Data and a Comparison with Fluid Friction**, *AIChE* **29**, 174 ( 1933 ).
- Dipprey, D. F. and Sabersky, R. H., **Heat and Momentum Transfer in Smooth and Rough Tubes at Various Prandtl Numbers**, *Int. J. Heat and Mass Transfer*, **6**, 329–353 ( 1963 ).
- Gee, D. L. and Webb, R. L., **Forced Convection Heat Transfer in Helically Rib-roughened Tubes**, *Int. J. Heat and Mass Transfer*, **23**, 1127–1136 ( 1980 ).
- Han, J. C., Glicksman, L. R. and Rohsenow, W. M. **An Investigation of Heat Transfer and Friction for Rib-Roughened Surfaces**, *Int. J. Heat and Mass Transfer*, **21**, 1143–1156 ( 1978).
- Hijikata, K. and Mori, Y., **Fundamental Study of Heat Transfer Augmentation of Tube Inside Surface by Cascade Smooth Surface-turbulence Promoters**, *Warme und Stoffubertragung*, **21**, 115–124 ( 1987 ).
- Lewis, M. J., **An Elementary Analysis for Predicting the Momentum and Heat Transfer Characteristics of a Hydraulically Rough Surface**, *Journal of Heat Transfer*, **75**, 249–254 ( 1975).
- Moody, L. F., **Friction Factors for Pipe Flow**, *ASME*, **66**, 671 ( 1944 ).
- Nakayama, W., Takahashi, K. and Daikoku, T., **Spiral Ribbing to Enhance Single-Phase Transfer Inside Tubes**, *ASME-JSM*, **1**, 365–372 ( 1983 ).
- Nikuradse, J., **Stromungsgesetze in Rauhen Rohren**, *Forsch. Arb. Ing. Wes.* **361** ( 1933 ).
- Seban, R. A., **Heat Transfer and Flow in a Shallow Rectangular Cavity with Subsonic Turbulent Air Flow**, *Int. J. Heat and Mass Transfer*, **8**, 1353–1368 ( 1965 ).

**Webb, R. L. , Eckert, E. R. G. and Goldstein, R. J. Heat Transfer and Friction in Tubes with Repeated-Rib Roughness, *Int. J. Heat and Mass Transfer*, 14, 601–617 ( 1970 ).**

## **II FUNDAMENTALS**

### **IIA Design Variables**

Three different pipes were analyzed. These pipes were manufactured at FINTUBE in Tulsa, OK. The construction of the pipes involved the folding of a carbon–steel slab into a cylindrical shape. To enhance the overall heat transfer coefficients of the pipes, structured promoters were embossed on the surface of the metal prior to the folding stage. In the case of the pipes that were analyzed in the present work, the type of promoters was a sequence of ribs and valleys. The process of embossing the pattern of ribs on the surface of the metal was achieved by rolling–compression of a cylindrical template on the surface of the metal slab. There are many different types of patterns that can be attained in this manner. However, this work concentrates on those patterns in which the final product was a sequence of ribs and valleys. The sequence was not transverse to the pipe axis but formed an angle with this axis, an angle that may vary from one model to another. Once the pattern was built, the slab was folded and welded by an ‘underwater–high frequency AC’ process. This prevented any alteration of the metal properties due to excessive heating, which might have happened with other conventional welding techniques. This welding stage left a seam in the interior of the pipe that interrupted the turning of the helicoidal array of ribs. To distinguish one model from the other, the manufacturers use a code. This code will be also used in the present work. A distinction must be made between the design variables of the unfolded and the final or folded pattern. This is because the code used by the manufacturers refers to the unfolded pattern. However, the present work will be

concerned with the characteristics of the pattern along the axis of the finished pipe, or, in other words, in the direction of the flow.

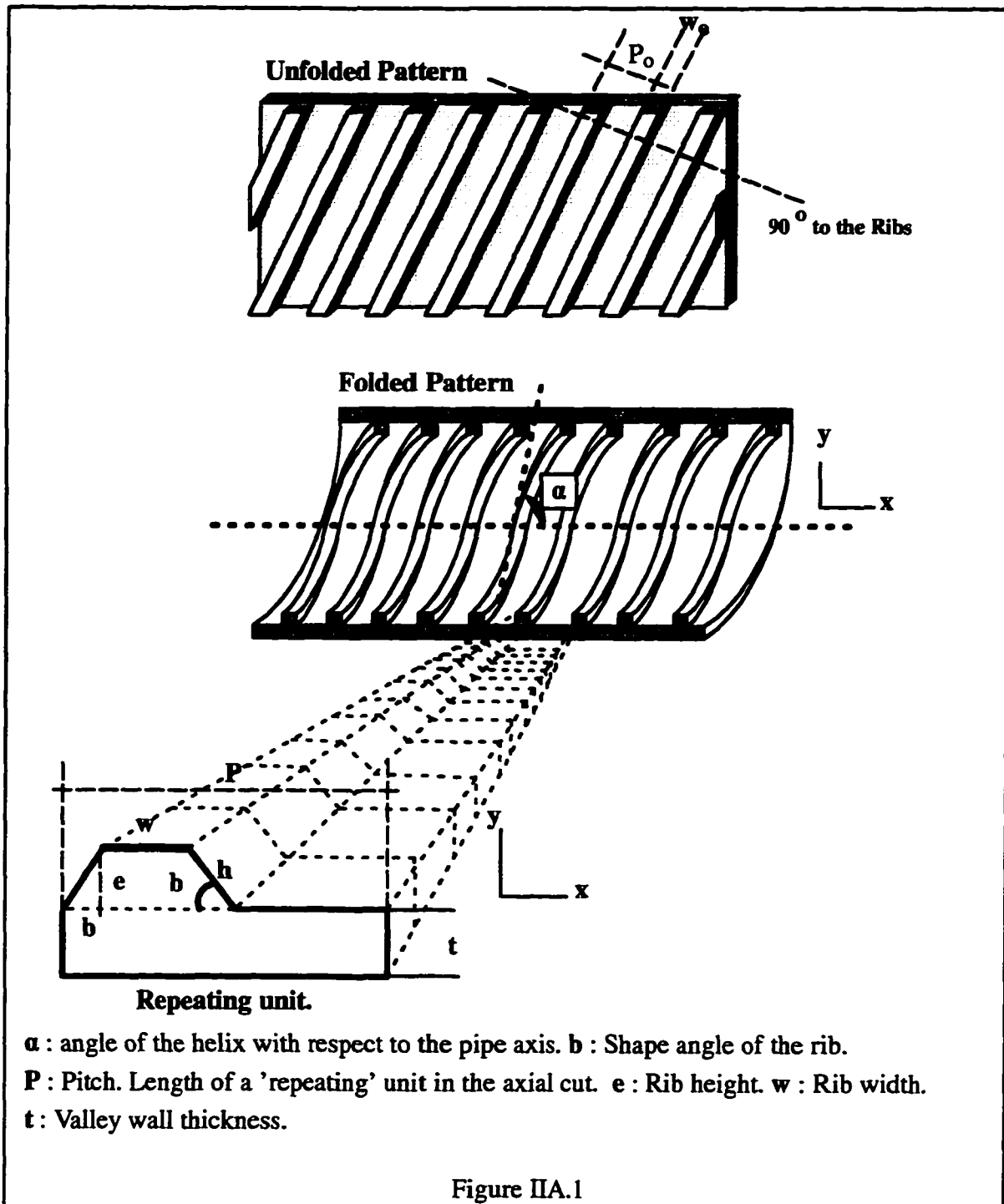
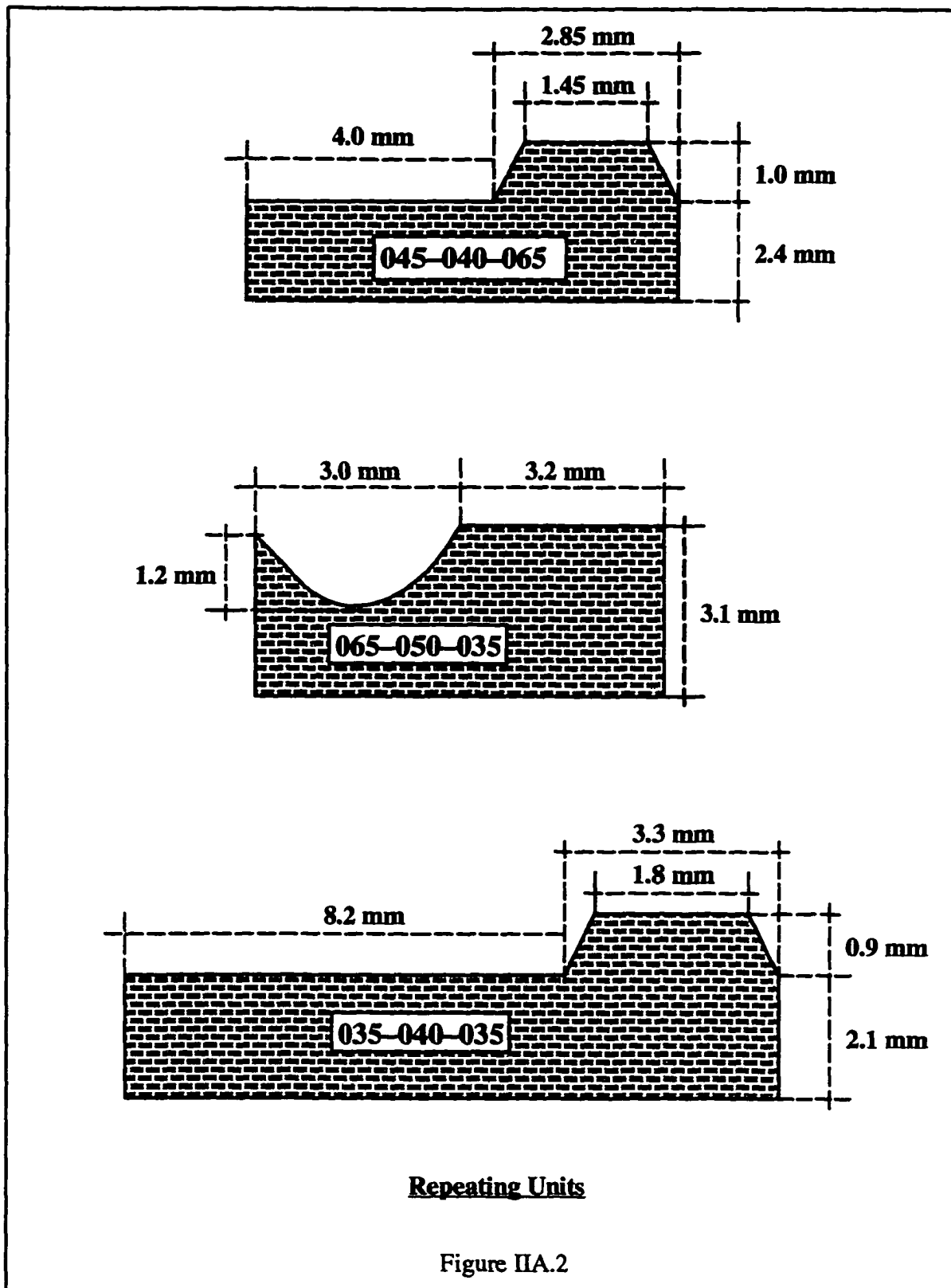


Figure IIA.1 clarifies this situation and depicts both the relationship between folded and unfolded variables and the meaning of the manufacturer's code. Figure IIA.1 also shows the rib shape. In the three models analyzed in this work, the rib shape was trapezoidal with a constant value of  $\beta = 60^\circ$ . The three pipes analyzed in this study had 0.05 m OD and 0.044 m ID when measured from the top of the ribs. As mentioned earlier, the code used by the manufacturers offers information on  $\alpha$  (rib angle respect to the pipe axis—last three digits),  $e$  (rib height in thousands of inch—middle digits), and  $1/P_0$  (pitch of the unfolded pattern measured perpendicular to the ribs in ribs/inch—first digits). It is clear from Figure IIA.1 that, given the pipe code, the values of the variables in the flow direction are related through the  $\sin(\alpha)$ . For the sake of clarity, what follows is an example of the formulas that relate the nominal values of the design variables in the perpendicular direction to the pattern with those in the direction of the flow:

Unfolded Pattern (perpendicular to the ribs)	Pipe Model Code 065-040-035	Flow Direction (folded pattern)
$\alpha = 35^\circ$		$\alpha = 35^\circ$
$\beta_0 = 60^\circ$		$\beta = \arctan(\tan \beta_0 \sin \alpha)$
$b_0 = \frac{e}{\tan(\beta_0)}$		$b_0 = \frac{e}{\tan(\beta_0) \sin(\alpha)}$
$P_0 = \frac{1}{6.5}$ inches/rib		$P = \frac{P_0}{\sin(\alpha)}$
$e = 0.040$ in		$e = 0.040$ in
$w_0 = e$ (according to manufacturer)		$w = \frac{w_0}{\sin(\alpha)}$
$h_0 = e \left[ 1 + \frac{1}{\tan(\beta_0)} \right]^{1/2}$		$h = e \left[ 1 + \frac{1}{\tan(\beta) \sin(\alpha)} \right]^{1/2}$

In spite of the fact that the manufacturers provided the code, it was considered safer to measure the design variables again. The manufacturer's code was created prior to the construction of the pipe and according to the template that would perform the embossment. Certain stages of the manufacturing process will alter the original pattern (code values). Small, but not negligible, discrepancies were found between the design values attained using the code and those measured in the lab. The measuring procedure was very simple. A small section of each of the three pipes analyzed was cut in the axial direction. With the aid of a magnifying lens and a scale, the variables such as  $P$ ,  $w$  and  $e$  were measured. The discrepancies between code and final pipe are due, not to manufacturers calculation errors, but to the complex behavior of the material when submitted to stresses and pressures. These stresses are necessary to emboss the pattern on the slab and can cause, for example, the final rib height  $e$ , to be shorter than the one intended or scheduled in the code. In fact, rib height  $e$ , and rib width  $w$ , were the variables in which the discrepancies code/actual measurement were the highest. These differences could be up to 20% of the code value. Finally, Figure IIA.2 shows what is called, in this work, a repeating unit which means a fragment of one rib and one valley in the direction of the flow. All variables are shown for the three models that were analyzed. Although the values of the variables are those measured in the lab, the manufacturers code number was kept to address each pipe facilitating the communication between the manufacturers and the research lab. These repeating units will be used extensively throughout this work.



### IIB Dimensional analysis

A dimensional analysis is introduced here to illustrate the contribution of the main variables. It is possible to anticipate some results from the relations between the dimensionless numbers that arose from the conversion to dimensionless form of the equations of momentum and energy and their associated boundary conditions. This section introduces the dimensionless equations for momentum and energy that describe the process of heat convection-conduction on the surface of a repeating unit. Prior to describing the equations, the following dimensionless variables are defined:

$$\begin{array}{llll}
 X = \frac{x}{e} & Y = \frac{y}{e} & \delta = \frac{1}{\sin \alpha} & \gamma = \frac{\delta}{\tan \beta} \\
 \eta = \frac{t}{e} & P^* = \frac{P_0}{e} & & \\
 u_y = \frac{u_y}{U_\infty} & u_x = \frac{u_x}{U_\infty} & \mathcal{P} = \frac{\Delta P}{\rho U_\infty^2} & \\
 \Theta = \frac{T - T_b}{T_0 - T_b} & N_{Re} = \frac{\rho U_\infty e}{\mu} & & 
 \end{array}$$

Where :

T<sub>b</sub> : bulk temperature of the fluid.

T<sub>0</sub> : temperature at the external wall of the repeating unit.

After replacing in momentum and energy equation :



Momentum:

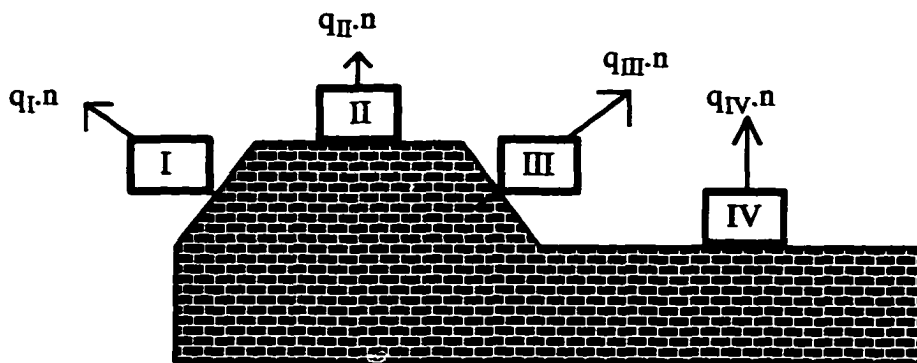
$$x) \quad u_x \frac{\partial u_x}{\partial X} + u_y \frac{\partial u_x}{\partial Y} = -\frac{\partial \mathcal{P}}{\partial X} + \frac{1}{N_{Re}} \left( \frac{\partial^2 u_x}{\partial X^2} + \frac{\partial^2 u_x}{\partial Y^2} \right) \quad \text{II B.1}$$

$$y) \quad u_x \frac{\partial u_y}{\partial X} + u_y \frac{\partial u_y}{\partial Y} = -\frac{\partial \mathcal{P}}{\partial Y} + \frac{1}{N_{Re}} \left( \frac{\partial^2 u_y}{\partial X^2} + \frac{\partial^2 u_y}{\partial Y^2} \right) \quad \text{II B.2}$$

Energy:

$$u_x \frac{\partial \Theta}{\partial X} + u_y \frac{\partial \Theta}{\partial Y} = \frac{1}{N_{Re} N_{Pr}} \left( \frac{\partial^2 \Theta}{\partial X^2} + \frac{\partial^2 \Theta}{\partial Y^2} \right) \quad \text{II B.3}$$

The geometrical regions are:



$q_i \cdot n =$  heat flux through surface ,i .

$h_i =$  average heat transfer coefficient at region ,i .

Equations II B.1 to 3 must be solved subject to the following boundary conditions:

Region I:            B.C.             $0 \leq X \leq \gamma$              $\eta \leq Y \leq 1 + \eta$

$$q_{I,n} = -k\nabla T = h_I (T_{\text{interfaceI}} - T_{\text{air}})$$

where  $q_{I,n}$  is the heat flux at surface ,h, ( see Figure IIA.1 ). This equation defines the local heat transfer coefficient at the interface. The temperature of the interface varies but the air temperature is assumed constant. Finally:

$$-\nabla\Theta.n = \frac{h_I e}{k} \Theta_I = N_{Nu}^I \Theta_I \quad \text{IIB.4}$$

where

$N_{Nu}^I$  : is the Nusselt number at the region I . The characteristic length is rib hight ,e .

$h_I$  : is the average heat transfer coefficient along surface ,h .

k: is the thermal conductivity of the fluid.

Region II :            B.C.             $\gamma \leq X \leq \gamma + \delta$              $Y = 1 + \eta$

$$q_{II,n} = -k\nabla T = h_{II} (T_{\text{interfaceII}} - T_{\text{air}})$$

where

$q_{II,n}$  is the heat flux at surface , w ( see Figure IIA.1 ) assuming constant air temperature. Finally:

$$-\nabla\Theta.n = \frac{h_{II} e}{k} \Theta_{II} = N_{Nu}^{II} \Theta_{II} \quad \text{IIB.5}$$

where

$N_{Nu}^{II}$  : is the Nusselt number at the region II with characteristic length rib hight , e .

$h_{II}$  : is the average heat transfer coefficient along surface , w .

$h_I$  : is the average heat transfer coefficient along surface 'h'.

k: is the thermal conductivity of the fluid.

Region III : this region is analogous to region I.

$$\text{B.C.} \quad \gamma + \delta \leq X \leq 2\gamma + \delta \quad \eta \leq Y \leq 1 + \eta$$

$$q_{\text{III}\cdot n} = -k\nabla T = h_{\text{III}} (T_{\text{interfaceIII}} - T_{\text{air}})$$

where

$q_{\text{III}\cdot n}$  is the heat flux at surface , h ( see Figure IIA.1 ) assuming constant air temperature. Finally:

$$-\nabla\Theta_{\cdot n} = \frac{h_{\text{III}}e}{k}\Theta_{\text{III}} = N_{\text{Nu}}^{\text{III}}\Theta_{\text{III}} \quad \text{IIB.6}$$

where

$N_{\text{Nu}}^{\text{III}}$  : is the Nusselt number at the region III with characteristic length rib hight , e .

$h_{\text{III}}$  : is the average heat transfer coefficient along surface ,h .

Region IV : this region is the bottom surface of the valley ( see Figure IIA.1 ).  
The length of this region is given by  $P-w-2b$ .

$$\text{B.C.} \quad 2\gamma + \delta \leq X \leq \delta P^* \quad Y = \eta$$

$$q_{\text{IV}\cdot n} = -k\nabla T = h_{\text{IV}} (T_{\text{interfaceIV}} - T_{\text{air}})$$

where

$q_{\text{IV}\cdot n}$  is the heat flux through the valley surface assuming constant air temperature. Finally:

$$-\nabla\Theta_{\cdot n} = \frac{h_{\text{IV}}e}{k}\Theta_{\text{IV}} = N_{\text{Nu}}^{\text{IV}}\Theta_{\text{IV}} \quad \text{IIB.7}$$

where

$N_{\text{Nu}}^{\text{IV}}$  : is the Nusselt number at the region IV with characteristic length rib hight , e .

$h_{\text{IV}}$  : is the average heat transfer coefficient along the valley surface.

Finally, the heat transfer process is expressed according to the dimensionless variables as:

$$\begin{aligned}\Theta_I &= \Theta_I(X, Y, N_{Re}, N_{Pr}, \gamma, \eta) \\ \langle N_{Nu}^I \rangle &= N_{Nu}^I(N_{Re}, N_{Pr}, \gamma, \eta)\end{aligned}\quad \text{II B.8}$$

$$\begin{aligned}\Theta_{II} &= \Theta_{II}(X, Y, N_{Re}, N_{Pr}, \gamma, \delta, \eta) \\ \langle N_{Nu}^{II} \rangle &= N_{Nu}^{II}(N_{Re}, N_{Pr}, \gamma, \delta, \eta)\end{aligned}\quad \text{II B.9}$$

$$\begin{aligned}\Theta_{III} &= \Theta_{III}(X, Y, N_{Re}, N_{Pr}, \gamma, \delta, \eta) \\ \langle N_{Nu}^{III} \rangle &= N_{Nu}^{III}(N_{Re}, N_{Pr}, \gamma, \delta, \eta)\end{aligned}\quad \text{II B.10}$$

$$\begin{aligned}\Theta_{IV} &= \Theta_{IV}(X, Y, N_{Re}, N_{Pr}, \gamma, \delta, \eta, P^*) \\ \langle N_{Nu}^{IV} \rangle &= N_{Nu}^{IV}(N_{Re}, N_{Pr}, \gamma, \delta, \eta, P^*)\end{aligned}\quad \text{II B.11}$$

Equations II B.8,9,10 and 11 show the dimensionless variables that can be expected in the solution of the heat transfer phenomenon on top of the repeating unit. The average Nusselt number for the totality of the repeating unit can be calculated as follows:

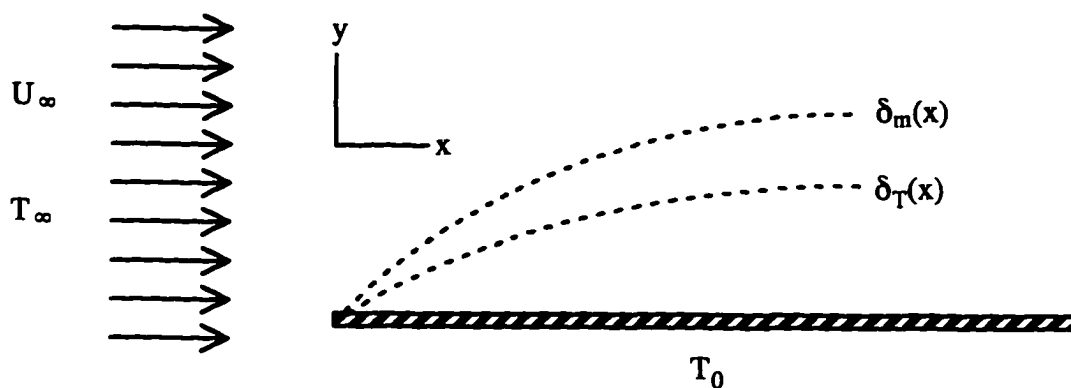
$$\ll N_{Nu} \gg = \frac{\langle N_{Nu}^I \rangle h + \langle N_{Nu}^{II} \rangle w + \langle N_{Nu}^{III} \rangle h + \langle N_{Nu}^{IV} \rangle (P - w - 2b)}{(P - 2b + 2h)}$$

$$\ll N_{Nu} \gg = \text{Overall Nusselt number for the repeating unit.} \quad \text{II B.12}$$

### IIC Developing Laminar Boundary Layer Equations

A succession of perturbations like the repeating units will produce a sequence of separation and reattachment of the boundary layer. Separation consists in the detachment of the boundary layer from the pipe wall. The condition for separation is that  $dU/dy|_{y=0} = 0$ . The point of zero velocity ( $U_x = 0$ ) is no longer at the wall but somewhere between the wall and the main stream. At this point it is said that the boundary layer breaks down. A condition for separation is the existence of back flow between the zero velocity point and the wall of the pipe and a positive pressure gradient. This region is usually called wake. The decelerated fluid produces large drag forces commonly found behind immersed bodies. When the wake disappears and the point of zero velocity is the last one of the velocity profile at the wall, it is said that the boundary layer starts developing again. This point is usually called point of reattachment of the boundary layer. The two concepts of separation and reattachment of the boundary layer are essential for the understanding of the present work.

The process of heat transfer on a repeating unit consists of breaking and developing boundary layers. For this purpose, the equations that define the heat transfer coefficients and friction factors for a developing boundary layer are introduced. This is a description of the general case of a developing boundary layer on a plate and must not be mistaken with the analysis performed in section IIB. The analysis is as follows:



$\delta_m(x)$  : Momentum boundary layer.

$\delta_T(x)$  : Thermal boundary layer.

Continuity:

$$\frac{\partial u}{\partial x} + \frac{\partial v}{\partial y} = 0 \quad \text{ПС.1}$$

Momentum:

$$u \frac{\partial u}{\partial x} + v \frac{\partial u}{\partial y} = \mu \frac{\partial^2 u}{\partial y^2} \quad \text{ПС.2}$$

Energy:

$$u \frac{\partial T}{\partial x} + v \frac{\partial T}{\partial y} = \alpha \left( \frac{\partial^2 T}{\partial x^2} + \frac{\partial^2 T}{\partial y^2} \right) \quad \text{ПС.3}$$

Boundary conditions:

- B.C.1  $u = U_\infty ; v = 0$  at  $x < 0$   
 B.C.2  $T = T_\infty$  at  $x \rightarrow \infty$   
 B.C.3  $u = v = 0$  at  $y = 0 \quad \forall x$   
 B.C.4  $T = T_0$  at  $y = 0 \quad \forall x$   
 B.C.5  $u \rightarrow U_\infty ; T \rightarrow T_0$  when  $y \rightarrow \infty$

Dimensionless variables:

$$X = \frac{x}{L} \quad Y = \frac{y}{L}$$

$$\varrho_u = \frac{u}{U_\infty} \quad \varrho_v = \frac{v}{U_\infty} \quad \Theta = \frac{T - T_0}{T_\infty - T_0}$$

Applying Blasius ( Schlichting 1968 ) similarity transformation:

$$\eta = y \left( \frac{U_\infty}{\nu x} \right)^{1/2} \quad \psi = f(\eta) ( \nu x U_\infty )^{1/2}$$

$$f' = \frac{df}{d\eta} \quad \Theta' = \frac{d\Theta}{d\eta}$$

Momentum:  $2f''' + ff'' = 0$  III.C.4

Thermal:  $2\Theta'' + N_{Pr} f\Theta' = 0$  III.C.5

B.C.6  $f = f' = \Theta = 0$  at  $\eta = 0$

B.C.7  $f' \rightarrow 1 ; \Theta \rightarrow 1$  when  $\eta \rightarrow \infty$

The numerical solution of Howarth( Schlichting 1968 ) is:

$$f''(h=0) = 0.33206$$

$$f'(h=0) = 0.99155$$

The shear stress acting on the plate is :

$$\tau_{xy} = \mu \frac{\partial u}{\partial y} \Big|_{y=0} = \mu U_{\infty} f'' \frac{\partial \eta}{\partial y} = \mu U_{\infty} \left( \frac{U_{\infty}}{\nu x} \right)^{\frac{1}{2}} f''(0) \quad \text{II.C.6}$$

Defining the Fanning friction factor as:

$$f_{(x)} = \frac{\tau_{xy}}{\frac{\rho U_{\infty}^2}{2}}$$

Replacing  $\tau_{xy}$  by eq. II.C.6 and Howarth's solution :

$$f_{(x)} = \frac{\mu U_{\infty} \left( \frac{U_{\infty}}{\nu x} \right)^{\frac{1}{2}}}{\frac{\rho U_{\infty}^2}{2}} \quad \text{and} \quad N_{Re} = \frac{\rho U_{\infty} x}{\mu}$$

$$f_{(x)} = 2 f''(0) (N_{Re}|_x)^{-\frac{1}{2}} \quad \text{II.C.7}$$

$$f_{(x)} = 0.664 (N_{Re}|_x)^{-\frac{1}{2}} \quad \text{II.C.8}$$

Eq. II.C.7 can be integrated for a plate of length ,L , to get  $\langle f \rangle$  :

$$\langle f \rangle_{bl} = \frac{1}{L} \int_0^L f_{(x)} dx = \frac{0.664}{L} \int_0^L \left( \frac{U_{\infty}}{\nu} \right)^{-\frac{1}{2}} x^{-\frac{1}{2}} dx$$

$$\langle f \rangle_{bl} = 1.328 (N_{Re}|_L)^{-\frac{1}{2}} \quad \text{II.C.9}$$



Equation IIC.5 can also be integrated between  $0 \rightarrow \eta$  :

$$\int_0^\eta \frac{\Theta''}{\Theta'} d\eta = -\frac{N_{Pr}}{2} \int_0^\eta f d\eta$$

$$\ln(\Theta') = \ln[\Theta'(\eta = 0)] - \frac{N_{Pr}}{2} \int_0^\eta f d\eta$$

$$\Theta'(\eta) = \Theta'(\eta = 0) e^{-\frac{N_{Pr}}{2} \int_0^\eta f d\eta} \quad \text{IIC.10}$$

Eq. IIC.10 can be integrated a second time:

$$\Theta(\eta) = \Theta(\eta = 0) + \Theta'(\eta = 0) \int_0^\eta e^{-\frac{N_{Pr}}{2} \int_0^\eta f d\eta} d\eta \quad \text{IIC.11}$$

Recalling :            B.C.6         $\Theta(\eta = 0) = 0$

                          B.C.7         $\Theta(\eta \rightarrow \infty) \rightarrow 1$

$$\Theta(\eta \rightarrow \infty) = 1 = \Theta'(\eta = 0) \int_0^\infty e^{-\frac{N_{Pr}}{2} \int_0^\eta f d\eta} d\eta$$

$$\Theta'(\eta = 0) = \frac{1}{\int_0^\infty e^{-\frac{N_{Pr}}{2} \int_0^\eta f d\eta} d\eta} = \Theta'(N_{Pr} f) \quad \text{IIC.12}$$

Applying  $\Pi C.12$  into  $\Pi C.11$  :

$$\Theta(\eta, N_{Pr}) = \frac{\int_0^\eta e^{-\frac{N_{Pr}}{2} \int_0^\eta f \, d\eta} \, d\eta}{\int_0^\infty e^{-\frac{N_{Pr}}{2} \int_0^\eta f \, d\eta} \, d\eta} \quad \Pi C.13$$

Define now:

$$h(x)(T_0 - T_\infty) = -k \frac{\partial T}{\partial y} \Big|_{y=0} \quad \Pi C.14$$

In dimensionless form:

$$\frac{\partial \Theta}{\partial Y} \Big|_{Y=0} = \left( \frac{\partial \Theta}{\partial \eta} \Big|_{\eta=0} \right) \frac{\partial \eta}{\partial Y} = \frac{h(x)L}{k} = N_{Nu}L$$

Since  $\frac{\partial \eta}{\partial Y} = \left( \frac{N_{Re}L}{x} \right)^{\frac{1}{2}}$  and  $\Theta'(\eta = 0) = \Theta'_0(N_{Pr})$  then:

$$\frac{h(x)L}{k} = \Theta'_0(N_{Pr}) \left( \frac{\rho U_\infty L}{\mu} \right)^{\frac{1}{2}} \left( \frac{L}{x} \right)^{\frac{1}{2}} \quad \Pi C.15$$

$$N_{Nu}(x) = \Theta'_0(N_{Pr}) (N_{Re}L)^{\frac{1}{2}} \left( \frac{L}{x} \right)^{\frac{1}{2}} \quad \Pi C.16$$

Eq. IIC.15 can be integrated to obtain the average value for the heat transfer coefficient and Nusselt number:

$$\langle h \rangle = \frac{k}{L} \Theta'(\eta = 0) \left( \frac{\rho U_{\infty}}{\mu} \right)^{\frac{1}{2}} \int_0^L \left( \frac{1}{x} \right)^{\frac{1}{2}} dx$$

$$\langle h \rangle = \frac{k}{L} 2 \Theta'(\eta = 0) \left( \frac{\rho U_{\infty}}{\mu} \right)^{\frac{1}{2}} L^{\frac{1}{2}}$$

$$\langle h \rangle = \frac{k}{L} 2 \Theta'(\eta = 0) (N_{Re}|_L)^{\frac{1}{2}} \quad \text{IIC.17}$$

$$\langle N_{Nu} \rangle = 2 \Theta'(\eta = 0) (N_{Re}|_L)^{\frac{1}{2}} \quad \text{IIC.18}$$

It is important to remember that the dependency with  $N_{Pr}$  is included in :

$$\Theta'(\eta = 0) = \mathcal{F}(N_{Pr})$$

In this way also :

$$\langle N_{Nu} \rangle = \mathcal{F}(N_{Pr}, N_{Re}) \quad \text{IIC.19}$$

In this way, friction and heat transfer were defined on the developing boundary layer. The former analysis will be of the utmost importance in understanding the phenomenon of heat transfer on a repeating unit. All the former equations will be recalled during the next sections.

### IID Smooth and Rough Pipe Flow

Turbulence in a fluid is caused by the lost of stability due to perturbations. The size of these perturbations is a function of both the kinetic energy and the physical size of the perturbing body . ( Schlichting 1968). The magnitude that measure the comparative value of both kinetic energy and physical size of the perturbation is the roughness Reynolds number  $\epsilon^*$ :

$$\epsilon^* = \frac{e U^*}{\nu}$$

$$U^* = \left( \frac{\tau_w}{\rho} \right)^{\frac{1}{2}} \quad \text{frictional velocity} \quad e : \text{roughness height}$$

$$\tau_w : \text{shear stress at the wall}$$

The smoothness or roughness of a pipe not only depends on the characteristics of its internal surface, but also on the flow regime. Because of this, a pipe is said to be “ hydraulically smooth” or “ hydraulically rough”. This means that, in spite of the fact that a pipe can have a certain physical roughness on its surface, the pipe can behave like a smooth one for low enough Reynolds numbers. On the contrary, a physically smooth pipe can behave like a rough one for large enough Reynolds numbers. The two regimes are separated by a transition region. The dimensionless friction ,  $\epsilon^*$  , is the number that will indicate, *a priori*, if a pipe can be considered hydraulically smooth or rough depending on the flow conditions. The limits of both regions and  $\epsilon^*$  are described as follows:

$0 \leq \epsilon^* \leq 5$	Hydraulically smooth regime.
$5 \leq \epsilon^* \leq 70$	Transition regime.
$70 \leq \epsilon^*$	Hydraulically rough.

The equations that represent the velocity profile in the near wall region are the Law of the Wall and Nikuradse's experiments (Schlichting 1968). These equations are related to each other in the following manner:

$$\frac{u}{U^*} = 2.5 \ln\left(\frac{y U^*}{\nu}\right) + 5.5 \quad \begin{array}{l} \text{Law of the Wall} \\ \text{(hydraulically smooth)} \end{array} \quad \text{IID.1}$$

$$\frac{u}{U^*} = 2.5 \ln\left(\frac{y}{e}\right) + 8.5 \quad \begin{array}{l} \text{Nikuradse} \\ \text{(completely rough)} \end{array} \quad \text{IID.2}$$

Adding and subtracting  $2.5 \ln\left(\frac{e U^*}{\nu}\right)$  to IID.1 :

$$\frac{u}{U^*} = 2.5 \ln\left(\frac{y}{e}\right) + 5.5 + 2.5 \ln\left(\frac{e U^*}{\nu}\right)$$

It can be said then, that the only equation is :

$$\frac{u}{U^*} = 2.5 \ln\left(\frac{y}{e}\right) + B \left(\frac{e U^*}{\nu}\right) \quad \text{IID.3}$$

and that B changes according to the regime:

$$B \left(\frac{e U^*}{\nu}\right) = 5.5 + 2.5 \ln\left(\frac{e U^*}{\nu}\right) \quad \begin{array}{l} \text{Law of the Wall} \\ \text{(hydraulically smooth)} \end{array} \quad \text{IID.4}$$

$$B = 8.5 \quad \begin{array}{l} \text{Nikuradse} \\ \text{(completely rough)} \end{array} \quad \text{IID.5}$$

In fact this is what occurs. Figure IID.1 illustrates the way in which B evolves according to the values of  $\epsilon^*$ :

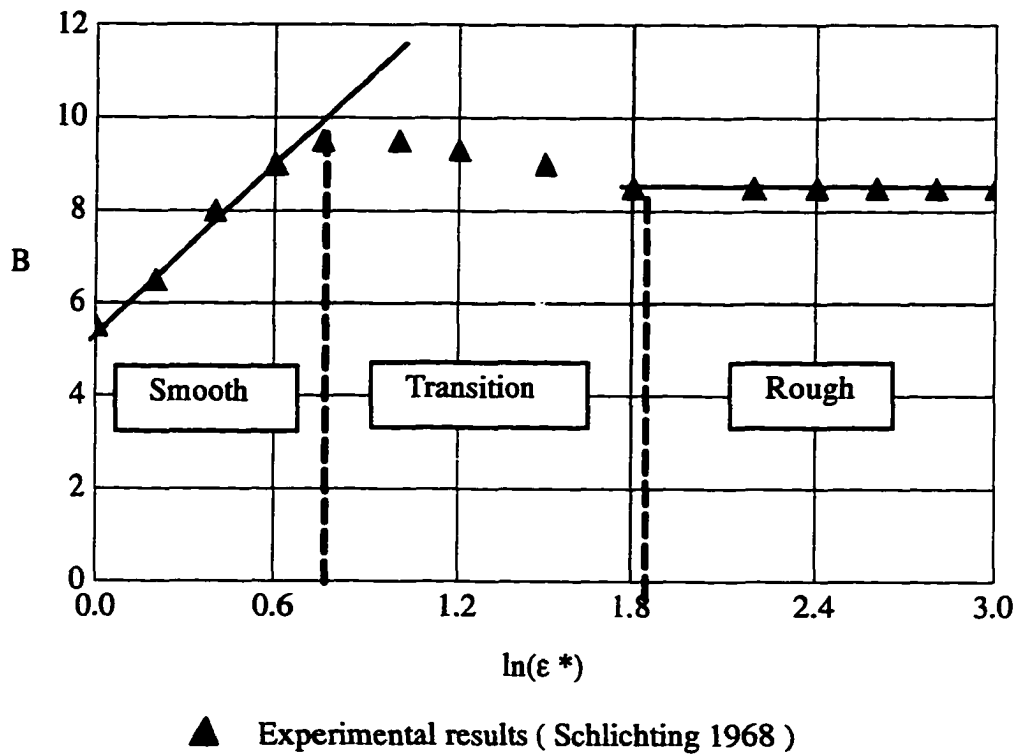


Figure IID.1

The results of this analysis will be used extensively in coming sections.

**REFERENCES**

Schlichting, H. , **Boundary – Layer Theory**, Mc Graw Hill Company, New York, ( 1968 ).

## III EXPERIMENTAL TECHNIQUES AND RESULTS

### III.A Experimental Setup

Experiments for flow and heat transfer study were carried out in two different setups for both air and water.

#### III.A.1 Water Loop

Figure III.A.1.1 The experimental setup for the analysis of water flow consisted of a 3m loop that was placed on top of an ORIEL optical table. The upper branch of the loop was a 2.74 m section of the industrial pipe to be tested. This array provided a value of  $L/D = 62$  (  $L$  = length,  $D$  = pipe ID ). The downstream end of the testing pipe was connected to an INVALCO ( Tulsa, OK ) turbine mass flowmeter model 3330 to measure the mass flow rate. This instrument was able to measure from 0 to 30 gal/min with an accuracy of 0.5 gal/min. An orifice plate was placed at the end of the testing pipe, connected to an oil manometer of accuracy 1 mm of oil. The purpose of the orifice plate was to allow for a higher degree of accuracy in the measurements of the flow rates and repeatability. After the orifice plate, and following the flow direction, a reservoir plastic tank of 50 gal. was placed before the intake of a 5HP centrifuge pump. The tank prevented possible cavitations of the pump when working at very low flow rates. A system of flow control was added to the pump. It consisted simply of a by-pass from the intake to the outlet of the pump where globe valves were placed to control the flow rate. At the impelling end of the pump a 4 micron mesh filter was placed parallel to the pipe line for periodic removal of debris and rust prior to operation. Right after the filter section a de-aeration tank was placed to keep bubbles of air that might enter the system and interfere with the measurements out of the water. The de-aeration tank joined the testing pipe with an elbow. After the elbow, a 1/4 inch pitch aluminum honeycomb was placed to guarantee the development of the flow once the fluid



reached the test section. Two taps separated at a distance of 2.43 m were added to the testing pipe for pressure drop measurements. These two taps were connected to an DWEYER (Tulsa, OK) inclined branch manometer that was filled with oil (specific gravity 1.91) that measures with an accuracy of 0.01 inches of oil. Downstream of the testing pipe and 0.2 m before the turbine flowmeter, an observation window was carved through the wall of the testing pipe. The dimensions of the window measured 2.5cm x 1cm. The window was covered with glass that was glued to the pipe allowing its removal if necessary. Additionally magnesium anodes had to be added to the system to protect it from corrosion. Corrosion was a major problem until the anodes were added because an iron oxide film started to cover the valleys and ribs. This problem occasioned turbidity of the water and, consequently, difficulty of implementation of the experimental techniques. The magnesium rods were electrically connected to the testing pipe and the pump and were immersed in the water at the reservoir tank. The anodic protection served as an excellent solution to stop the corrosive degradation of the system.

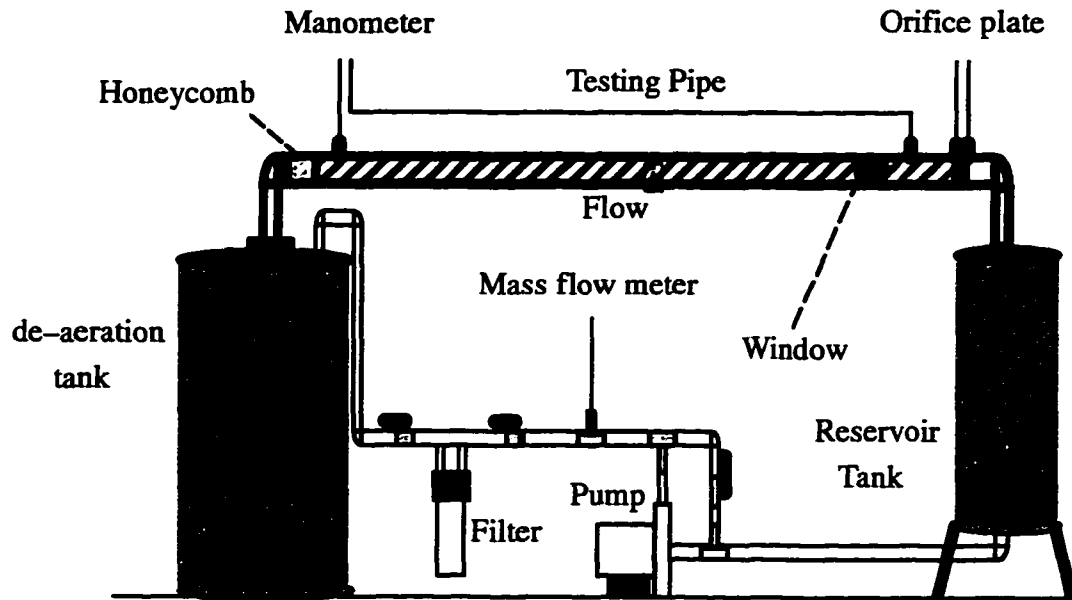


Figure IIIA1.1

### III.A.2 Air Loop

Figure IIIA.2.1 The experimental setup used for air flow was conceptually the same as the one for water. The same length of testing pipe was used with taps for pressure measurement including the observation window. The pump and tanks for the water setup were replaced with a DYTON model 5C088 air blower with a capacity of delivering 15 m/s of air velocity. The loop was closed with a carbon steel smooth pipe of the same length as the testing pipe. The honeycomb at the upstream section of the testing pipe was also included and an OMEGA air mass flowmeter model HHF300 was placed at the end of the testing pipe section with a globe valve for flow rate control right before a returning elbow. The HHF300 flow meter measured from 0 to 10 m/s of air with an accuracy of 0.1 m/s. The pressure drops were measured with the aid of a DWEYB's inclined manometer filled with oil 0.96 specific gravity of accuracy 0.01 inches of oil. No further changes were needed other than the fact that, for obvious reasons, the anodic protection was not necessary on the air loop. Finally, a thermocouple was placed downstream of the observation window to measure the air temperature  $T_a$ . The thermocouple measure the air stream temperature with an accuracy of 0.1  $^{\circ}\text{C}$ .

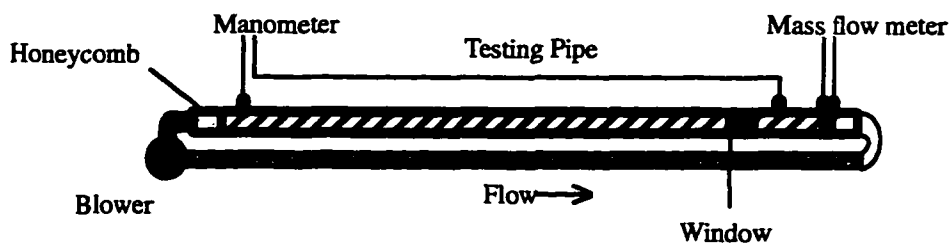


Figure IIIA.2.1

Some other features of the experimental setup will be described in the next section where each of the experimental techniques is described. Each of the experiments required additional equipment that will be more easily understood as a part of a certain data acquisition system.

### IIIB Local Heat Transfer Coefficients ( $h_x$ )

#### IIIB.1 Liquid Crystals Technique for Temperature Profile Acquisition

The object of these experiments was to measure the temperature profiles on the internal ribbed walls of the pipe under different air-flow/heating rate conditions. This was achieved through the use of a technique that was called Liquid Crystals (LC). The observation of temperature profiles by the use of LC technique was first implemented by Fergason ( 1964 ) and extensively applied by Baughn ( 1994) to measure local heat transfer coefficients. The liquid crystals are chiral nematic polymers in water solution. Because the LC are soluble in water, this technique could only be applied to air flow. The LC have the capability of existing in different crystalline forms according to their temperature. The different crystalline forms have different colors and these colors are associated with temperature ranges. Given that these changes of colors occur for very small changes in temperature, the LC method is an excellent way to measure small temperature changes. Moreover, the changes of temperature expected on a small heated section of the pipe with air flow at room temperature were also expected to be very small, in fact, undetectable by any other method of analysis. The aqueous solution of crystals is applied like a paint using an air brush on top of a black background paint of high thermal conductivity ( HALLCREST, Glenview, Illinois). Each color has a temperature assigned by the manufacturer, and they are as accurate as 0.05 °C for a restricted range. In the case of the present work a commercial LC solution manufactured by HALLCREST( Glenview, Illinois)

was used. On Table IIIB1.1 the range of the color scale of the LC and the corresponding values of temperature are shown.

**Table IIIB1.1**  
**Liquid Crystals Scale used in the present work.**

Visible Starts	—————	44.7 °C
Red Starts	—————	45.0 °C
Yellow Starts	—————	45.2 °C
Green Starts	—————	45.4 °C
Blue Starts	—————	46.0 °C

The LC were first calibrated. This calibration consisted in painting a small slab of steel painted with the LC on one face. On the other face a small heating resistance was attached. While heating, the colors on the slab were recorded with a CCD camera and displayed on a color monitor. The colors perceived by the naked eye were compared to those seen on the screen of the monitor. In this way the differences between the real colors and the ones displayed on the screen were explored. The CCD camera controls were adjusted to achieve no difference between the monitor screen and the real colors on the slab.

The interior of the testing pipe in front of the observation window was painted with a thin coat of LC . To record the changes in temperature under different flow/heating rates, this small section of pipe was heated from the outside with the device shown on Figure IIIB.1.1 This device consisted of an aluminum solid block in which a curvature was carved to match that one of the testing pipe. The aluminum block functioned to distribute the heat evenly. In this manner, the approximation of constant heat flux on the external wall of the pipe was possible. On the other side of the aluminum block, a groove of 25.4 mm x 76.2mm and 3mm deep was carved. On this groove an OMEGALUX srfg 103/10p heating resistance ( $R = 480 \Omega$  ) was placed. The total area

of the resistance was  $3 \text{ in}^2$ . The electric power was provided to the resistance with an AC variac that allowed the delivery of controlled voltage to the resistance and, therefore, the heat transferred to the aluminum block. To ensure the accuracy of the voltage measurement, a digital voltmeter was connected parallel to the variac.

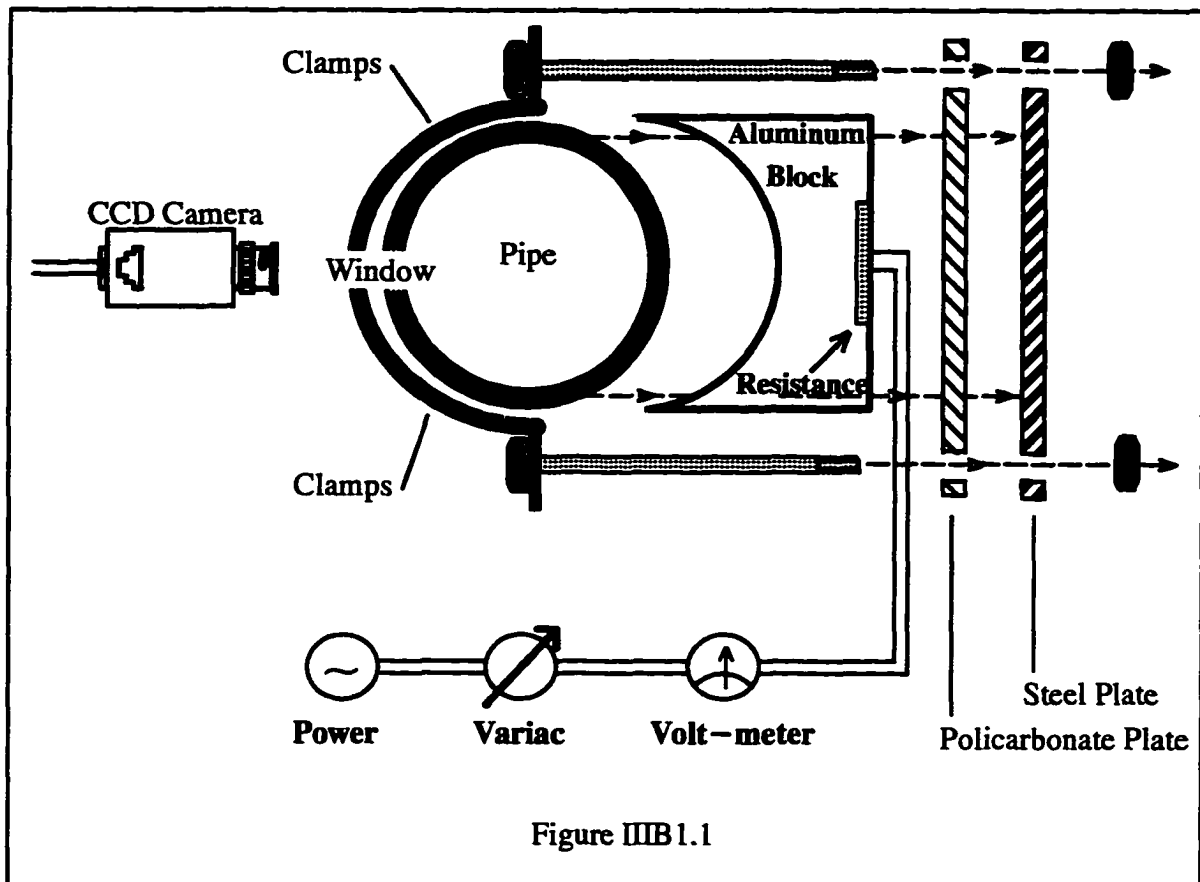


Figure IIB 1.1

The rest of the heating block was insulated with fiber glass and the resistance was held in place with a polycarbonate slab. In such a way it was assumed that all the heat generated by the resistance was carried out into the aluminum block. Given the high thermal conductivity of Al ( $150 \text{ watts/m } ^\circ\text{C h}$ ), the losses for natural convection through the insulation were minimal granting that the maximum amount of heat generated was reaching the pipe. However, these losses were taken into consideration, as shown later. Two clamps held the block in contact with

the external wall of the pipe. To ensure that this contact was thermally optimal, a conductive paste of aluminum powder and silicon oil was placed in between the block and the pipe. Once the clamps were tied the excess paste squirted out of the joint leaving the necessary amount to guarantee good heat conduction. The changes in color of the LC on the internal wall of the testing pipe were recorded through the observation window. For this purpose a CCD color camera with a 50 mm lens was placed in front of the window and connected to a Panasonic 7350 VCR and a SONY Trinitron color monitor. Because of the restriction of the LC temperature range, a wide sweep of flow rates at constant applied voltage on the resistance was not possible. If the flow was increased too much at a constant heating rate, the colors would disappear. Obviously this was because the air was cooling the internal wall to temperatures below the LC range. It was found however, that by changing both flow rate and voltage, consistent color patterns would appear. In other words, a single temperature profile on the ribs of the pipe repeated for different values of voltages and flow rates. Of course, a pattern that was completely red or completely blue was not the optimum because it would only yield one temperature. What was needed was the highest span of colors present on the same pattern. In this way a higher amount of points on top of the rib/valley surface could be assigned a temperature. Once this color pattern was found, by adjusting flow and heat flux, the corresponding voltage and air velocity were recorded. The next step was to reduce the voltage arbitrarily and then reduce the flow rate until the same color pattern appeared on top of the ribs. The procedure was repeated until the minimum possible flow rate was achieved. The voltages were turned into heat fluxes according to:

$$Q_i = \frac{V_i^2}{AR} \quad \text{Heat flux generated by the resistance and incoming the aluminum block at } N_{Rei}. \text{ [watts/m}^2\text{]}$$

Where ' $V_i$ ' is the voltage download to the resistance through the variac. ' $A$ ' is the area of the resistance in  $m^2$  and ' $R$ ' is the electrical resistance in  $\Omega$ .

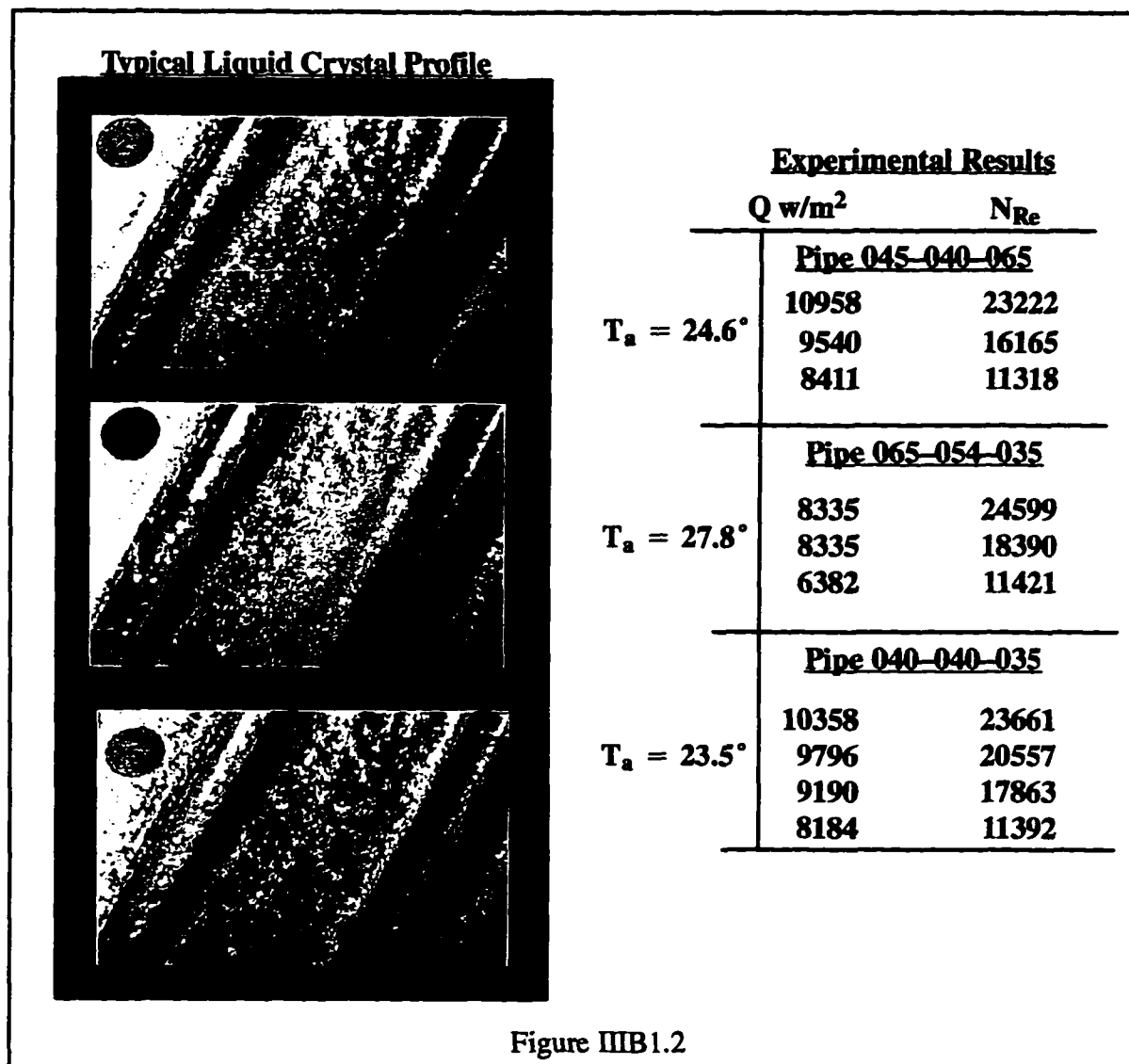


Figure IIIB1.2 shows the color patterns recorded for the pipes that were analyzed. Also included are the corresponding sequences of Heat Fluxes ' $Q_i$ ' and  $N_{Rei}$  with the ambient temperature at the moment of the experiment. From the colors of each picture the temperatures on top of a repeating unit were obtained. Figure IIB1.3 shows the three repeating units with the values of temperature taken from the LC pictures that were called  $T_{c_x}$ . Also on this graph are plotted matching curves joining the points. The reason for plotting a smooth curve and a piece-wise curve will be explained in the following section, as will the reason for choosing a piece-wise

approach over a smooth one. Finally, for all these experiments, the air loop was operated with the suction of the blower open to the ambient. In this way it was possible to assume that the temperature of the air stream,  $T_a$ , was fairly constant and equal to the ambient temperature.

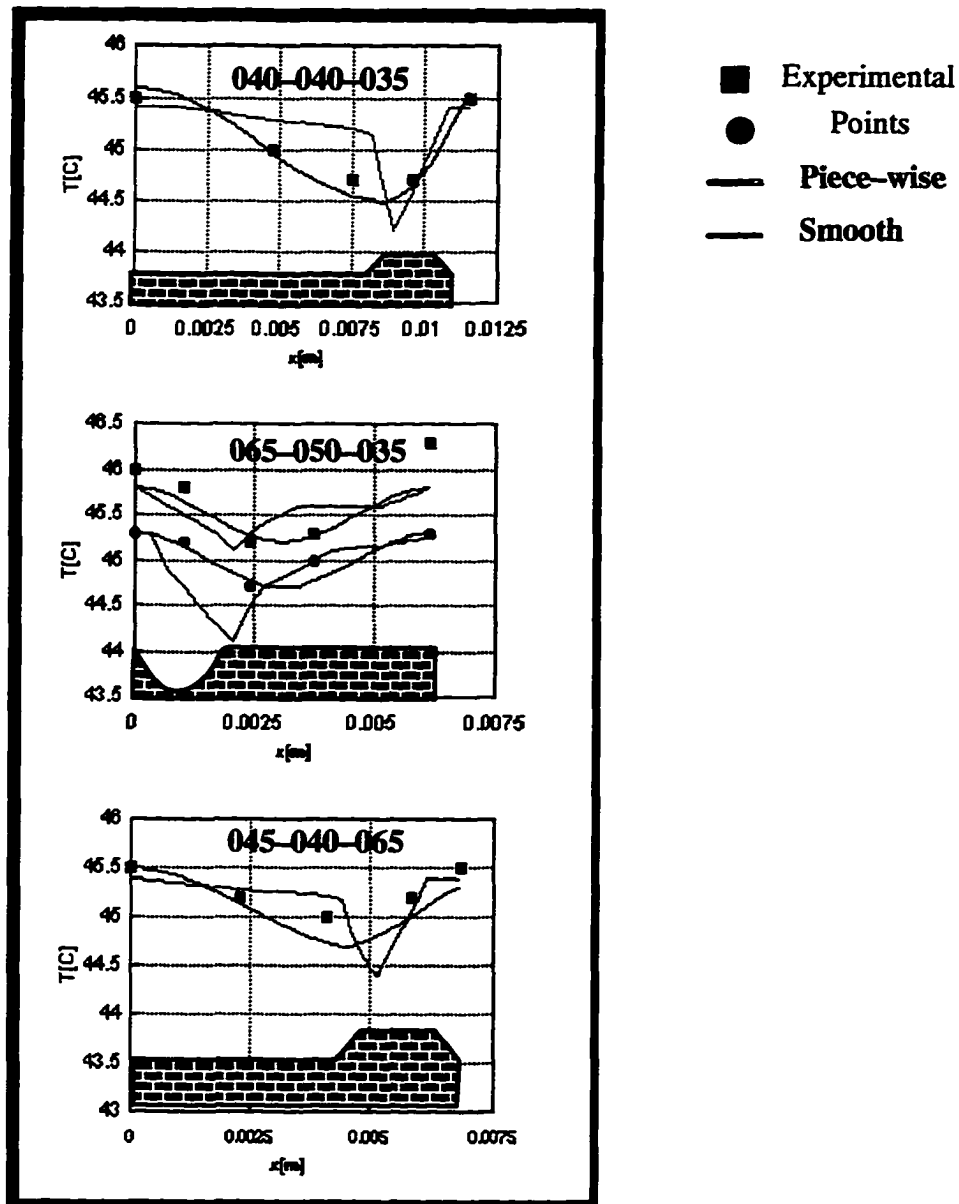


Figure IIB1.3



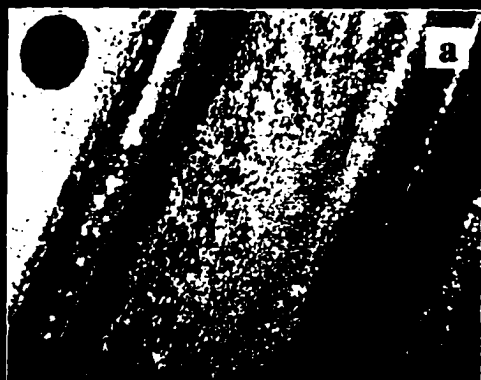
### III.B.2 Computational Analysis of LC Results

Figure III.B.2.1 shows the basic stages of the computations as well as the boundary conditions that were used. The final product of this procedure were the profiles of local heat transfer coefficients for the three repeating units. The computations were carried out with the aid of FLUENT, a commercial software capable of solving the heat conduction equations. Figure III.B.2.1 shows four different stages: a) Acquisition of the LC pictures at different air flow rates and different heat fluxes provided by the heating element. b) Construction of a temperature profile from the LC pictures. Prior to continue to the next stage it was necessary to calculate the total heat flux on top of the repeating unit. Not all the heat generated in the heating element reached the internal walls of the pipe. Therefore, it was necessary to calculate the heat flux on the repeating unit for each voltage applied on the heating element. This calculation required an additional global computation that accounted for losses to the environment and axial conduction through the pipe. This computation procedure will be described in detail in the next section. c) This stage consisted in the computation of the heat fluxes distribution on top of the repeating unit. The boundary conditions were the temperature profiles from stage ( b ) and the total heat flux for a repeating unit calculated in the global computation mentioned above. d) This final stage consisted in the calculation of local heat transfer coefficients from the distribution of heat fluxes of stage (c).

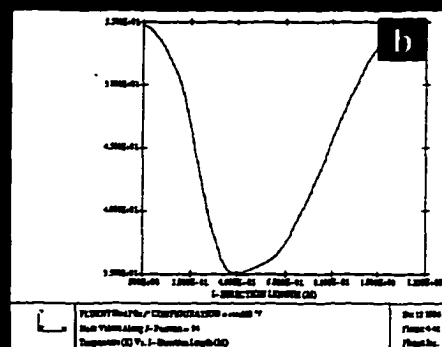
Following Figure III.B.2.1 is the detail explanation of the two types of computations that were performed; the global one for the computation of total heat flux on the repeating unit and the local one for the distribution of heat fluxes on a repeating unit.

## Local Heat-Transfer Coefficients Computation Scheme

Liquid Crystals Picture.



T profile for 1 repeating unit.



'FLUENT' Solution of Conduction.



hloc profile for 1 repeating unit.

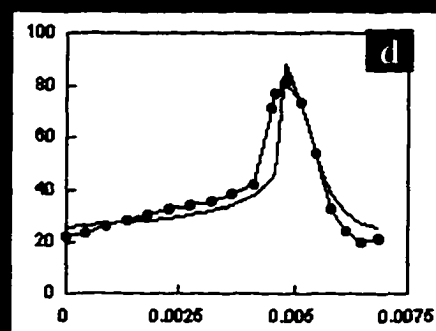
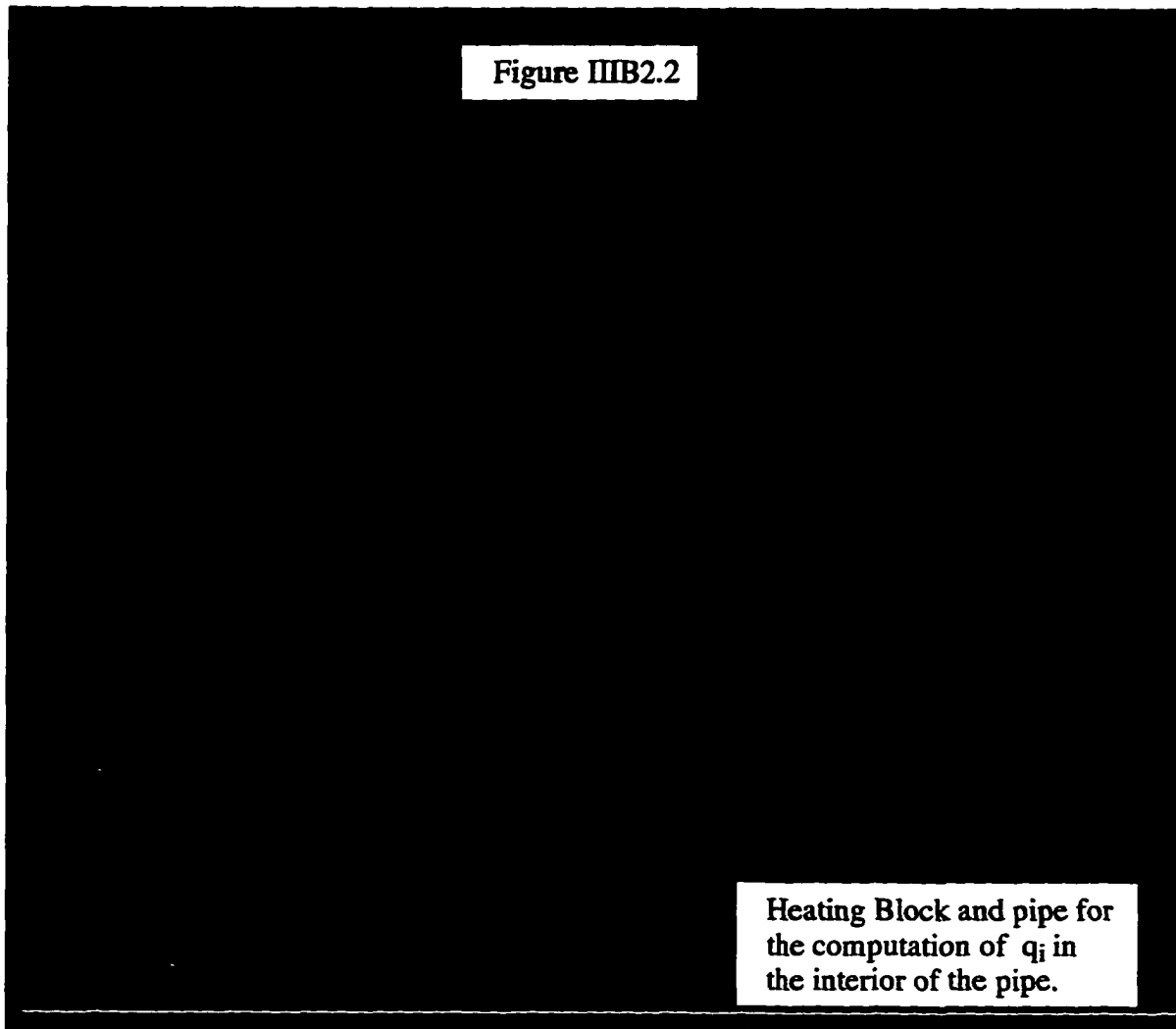


Figure IIB2.1

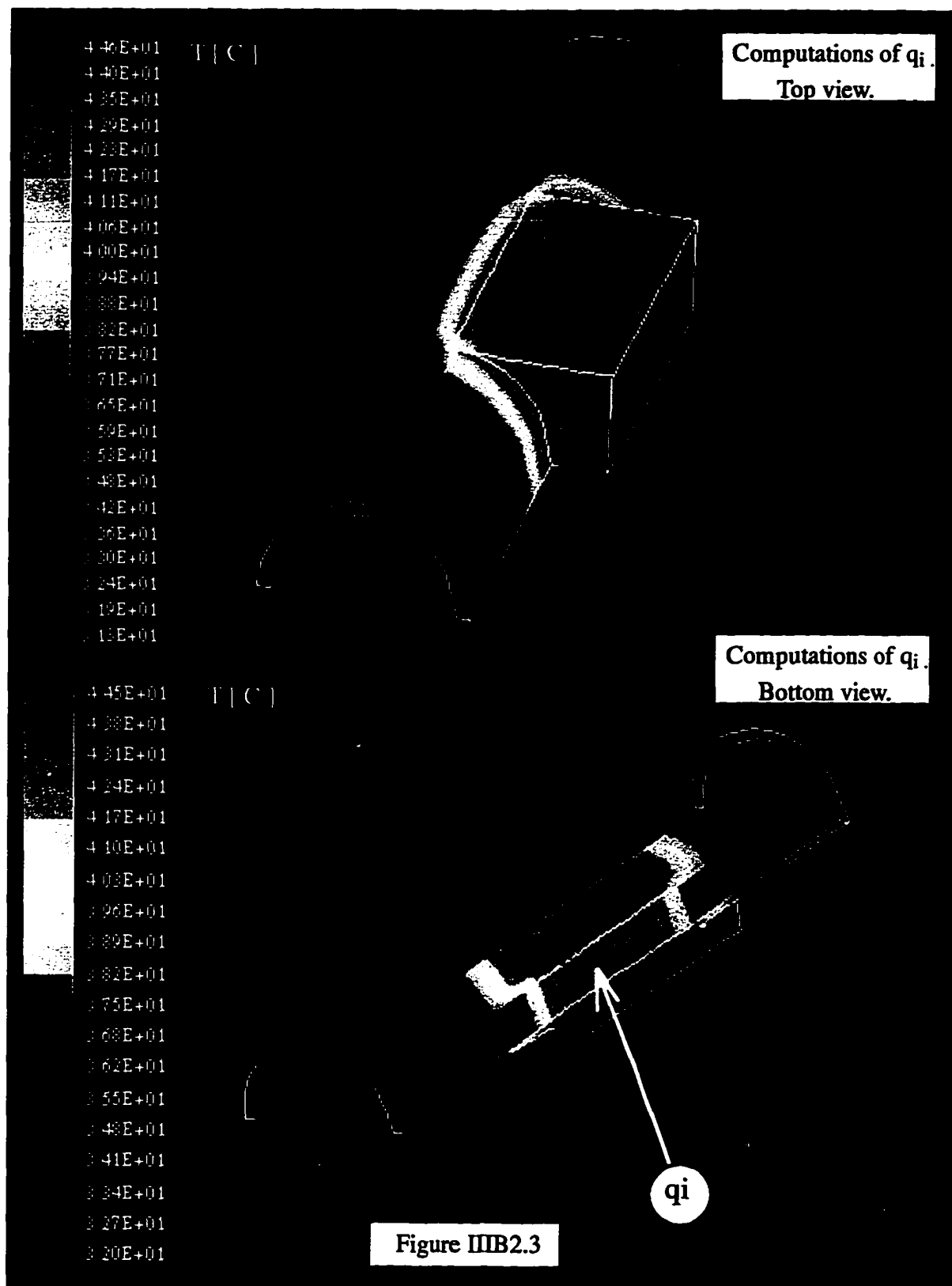
a) Computations of heat flux on internal wall of the pipe: As described in section IIIB1, the heating block provided the heat necessary for the LC to show a temperature profile on the internal wall of the pipe. Prior to associating these temperature profiles to local heat transfer coefficients ( $h_x$ ), it was necessary to calculate the heat flux present at the internal surface of the pipe. In order to obtain the  $h_{loc}$  on a repeating unit from the LC temperature profiles, it was necessary first to calculate the values of the heat flux on that repeating unit. For this purpose the first type of computations was carried out. It consisted of a 3D simulation based on the geometry shown on FigureIIIB2.2.



Given the radial symmetry existing on the array shown on Figure IIIB1.1, it was enough to consider half of the physical domain to perform the computations. Also, the ribs and valleys were not included in the interior of the pipe since this was a simulation about the global  $q_i$  on the internal wall and not its localized distribution. As shown on Figure IIIB2.2, two additional sections of half pipe were added, (compared to Figure IIIB1.1), to account for conduction in the axial direction. Also, a thin layer of  $30\mu$  of LC was included directly in front of the heating block on the interior of the pipe.

The boundary conditions applied to the problem were as follows: a) External wall of the pipe and aluminum heating block : a global natural convection  $\langle h_o \rangle$  was assumed on the external walls of the pipe as well as on the exterior of the heating block. The value of  $\langle h_o \rangle = 1$  [watts/m<sup>2</sup>K] was taken to be the same for all the computations. The thermal conductivity of the aluminum block was  $k_{Al} = 120$  watts/m K. For the carbon-steel pipe, and according to data of composition provided by the manufacturers, the thermal conductivity for the pipe was  $k_p = 50$  watts/m K. b) Heating resistance: the values of voltages, provided  $Q_i$  to be assigned to the resistant for each one of the experiments at a given  $N_{Re}$ . c) Interior of the pipe and LC coating: The thermal conductivity of the LC was 0.1 watts/m K and the coating was simulated to be 12mm x 50mm in size. The internal heat transfer coefficient in the pipe  $\langle h_i \rangle$  was adjusted until the temperature of the LC surface coincided with that one on the corresponding picture. Of course it was necessary to take an average temperature  $\langle T_{c_x} \rangle$  of the LC on each one of the pictures that was analyzed. This approximation did not damage the accuracy of the method given that the differences of temperatures found on the LC were very small. d) Air stream temperature  $T_a$ : the air stream temperature was the thermocouple read-out ( section IIA.2 ).

Finally, upon running the program, the values of  $q_i$  were recorded. Figure IIIB2.3 shows a typical contour plot of the model from two different perspectives and shows the region from where  $q_i$  was taken.



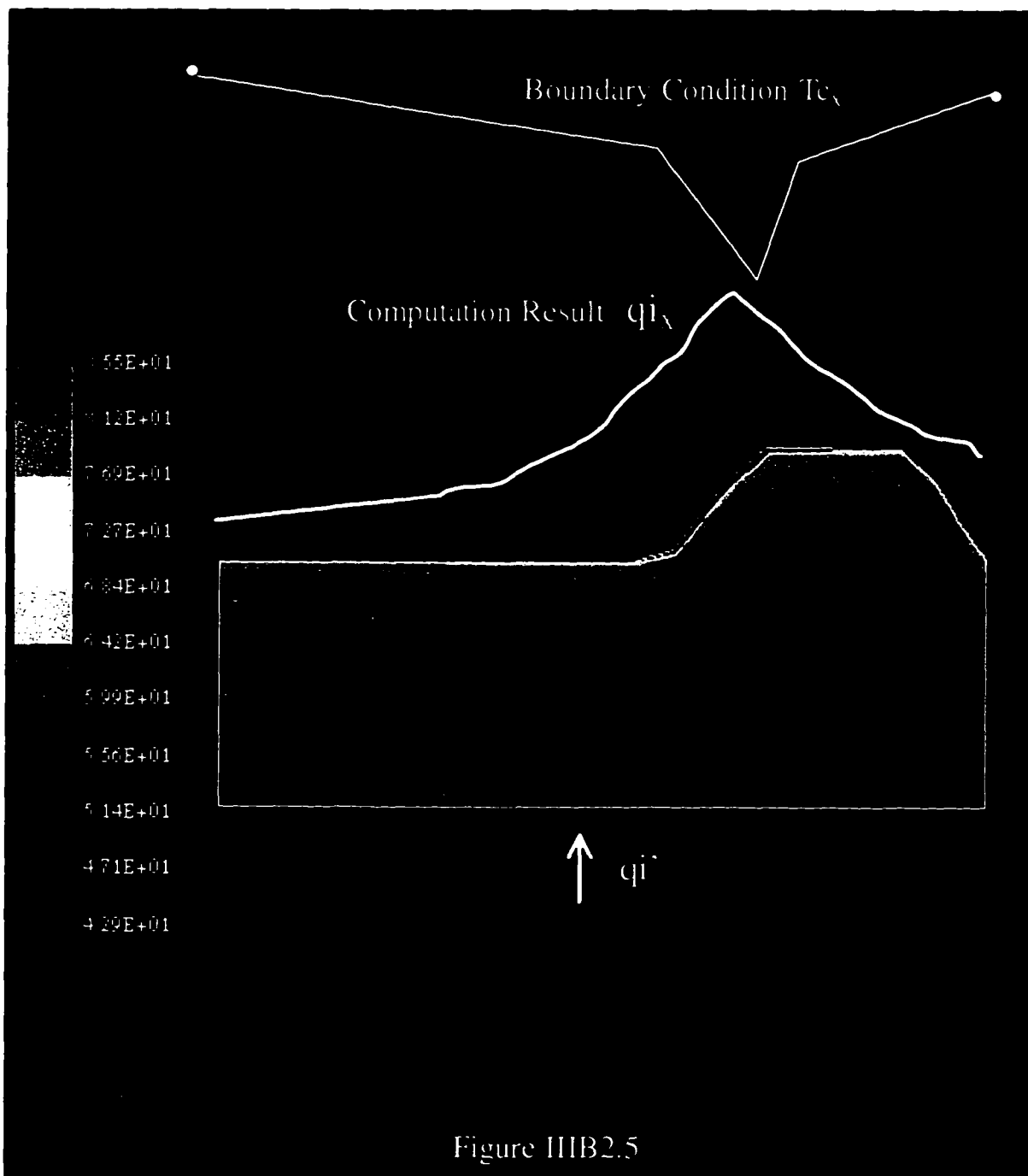
The  $q_i$  was taken to be the value of heat flux at the point shown on Figure IIIB2.3 . Also Figure IIIB2.4 shows the results of this first computation including the values of  $Q_i$ ,  $N_{Re}$  and  $q_i$  for the three different pipes. It is important to point out that changes in  $\langle h_o \rangle$  of up to 100% resulted in no more than 0.1 % change in  $q_i$  . The product of these computations were the heat fluxes on top of a repeating unit for the three pipes. These heat fluxes  $q_i$  were the main boundary condition in the computation of  $h_{loc}$  profiles on top of a repeating unit.

$Q$ [w/m <sup>2</sup> ]	$N_{Re}$	$q_i$ [ w/m <sup>2</sup> ]
<b><u>Pipe 045-040-065</u></b>		
10958	23222	1083.7
9540	16165	824.4
8411	11318	681.0
<b><u>Pipe 065-054-035</u></b>		
8335	24599	813.5
8335	18390	698.5
6382	11421	461.0
<b><u>Pipe 040-040-035</u></b>		
10358	23661	946.2
9796	20557	860.2
9190	17863	797.5
8184	11392	521.5

Figure IIIB2.4

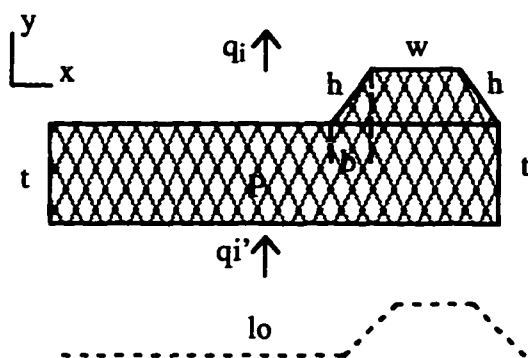
b) Computation of local heat transfer coefficients  $h_x$ : These computations consisted of the calculation of  $h_x$  on top of a repeating unit given  $q_i$  and the  $Tc_x$  profile. The model used for these simulations was basically of the same shape as those repeating units on Figure II2 of section II. It consisted of a 2D model of the pipe wall including one rib and one valley in which the depth was taken to be the unit. Also a thin layer of LC 30 $\mu$  was added on top of the pattern to account

for conduction through this material as it was done on the former computations. Figure IIB2.5 shows the model with a schematic of boundary conditions and results.



The physical properties of the steel and the LC were the same as those explained in section IIB2.a. The basic boundary conditions for this analysis were:

i)  $q_i'$  heat flux at the bottom of the repeating unit: This heat flux must not be mistaken with  $q_i$ . The  $q_i$  is the heat flux entering the air stream on top of the repeating unit through the surface  $A_c$ . This surface is the length the whole pattern of rib and valley  $l_o$ , multiplied by the unit. The  $q_i'$  is the heat flux entering the repeating unit at the bottom wall or exterior of the pipe. This  $q_i'$  flux is transferred through the surface  $A_o$ , that is simply the value of  $P$  (pitch) multiplied by a unit depth. The procedure to obtain this  $q_i'$ , prior to applying it as a boundary condition, was very simple:



$$q_i' = \frac{A_c}{A_o} = q_i \frac{(P - 2b + 2h)}{P}$$

Assuming that the heat losses at 't' were negligible.

$$l_o = P - 2b + 2h$$

ii) Temperature profile  $T_{c_x}$  from LC: As mentioned in section IIIB1, there are alternative interpretations of the LC pictures. Joining the points of different temperatures by a smooth or a piece-wise curve resulted in dramatic differences in the solution. iii) the boundary conditions at 't' were, as the software denominates, 'periodic boundary'. This means that the software solves the equations at these points considering that whatever occurs on the left 't' wall has to be reflected on the right 't' wall. It means that, not only temperature, but first and second derivatives of temperature are considered to be of the same value.



The output of the computations was the distribution of  $q_i$  on top of the repeating unit along  $x$ , that was called  $q_{i_x}$ . In this manner, from the LC temperature profile a profile of local heat fluxes was calculated. The values of  $h_x$  were calculated dividing the local fluxes  $q_{i_x}$  by the local temperature  $T_{c_x}$  on the surface minus the air stream temperature  $T_a$ :

$$h_x = \frac{q_{i_x}}{T_{c_x} - T_a}$$

Again, the assumption of constant air temperature is supported by the fact that the test section is small enough that the temperature of the air will be constant at any point of the loop. This can be shown in an order of magnitude analysis of the overall heating process:

In the most unfavorable case,  $Q_i$  and mass flow rate were:

$$Q_i = 10 \text{ watts} \quad \dot{m} = 8 \text{ g/s} \quad C_{p_{\text{air}}} = 1.007 \text{ J/gC}^\circ$$

The value of  $\Delta T$  along the heating region was:

$$\Delta T = \frac{Q_i}{C_{p_{\text{air}}} \dot{m}} = 1.24 \text{ C}^\circ$$

This result was not alarming because it was the temperature build-up along the pipe wall in the direction of the flow. The length of the heated region is the same as the length of the heating block, ( section IIIB.1) and equal to 76.2 mm. The temperature build-up per unit length was:

$$\frac{\Delta T}{\text{Heated Length}} = 0.016 \frac{\text{C}^\circ}{\text{mm}}$$

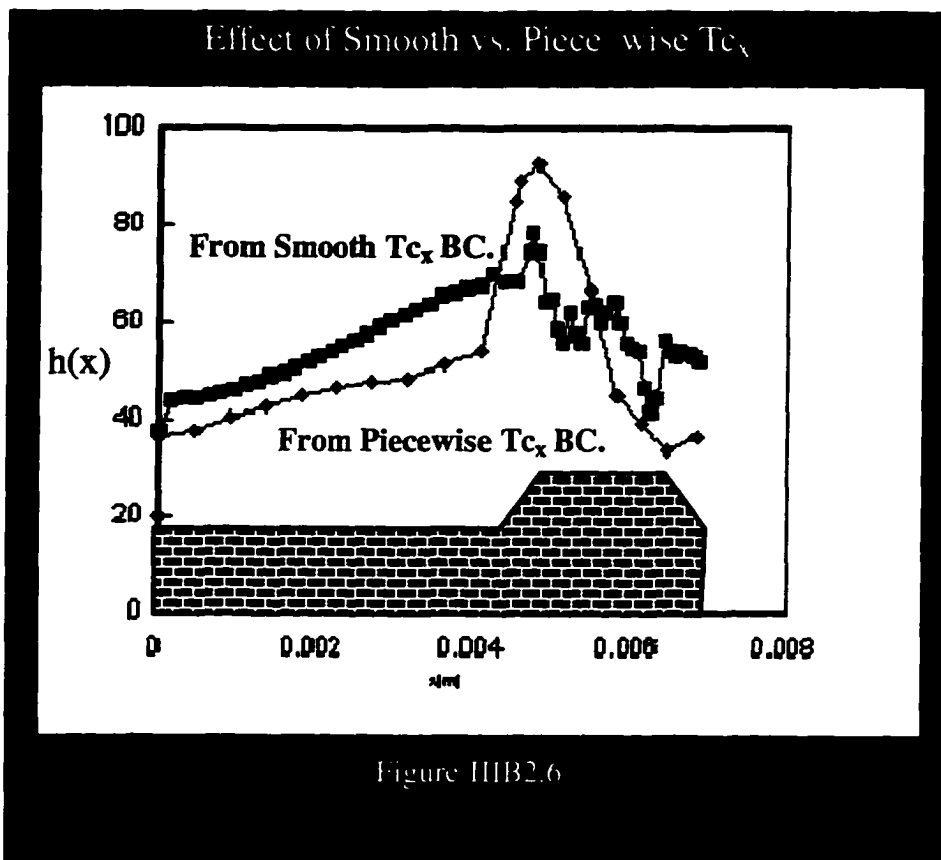
This means that for the longest repeating unit analyzed (  $P = 11.5 \text{ mm}$  ) the temperature would increase in:

$$\Delta T_{11.5 \text{ mm}} = 0.016 \frac{\text{C}^\circ}{\text{mm}} \times 11.5 \text{ mm} = 0.18 \text{C}^\circ$$

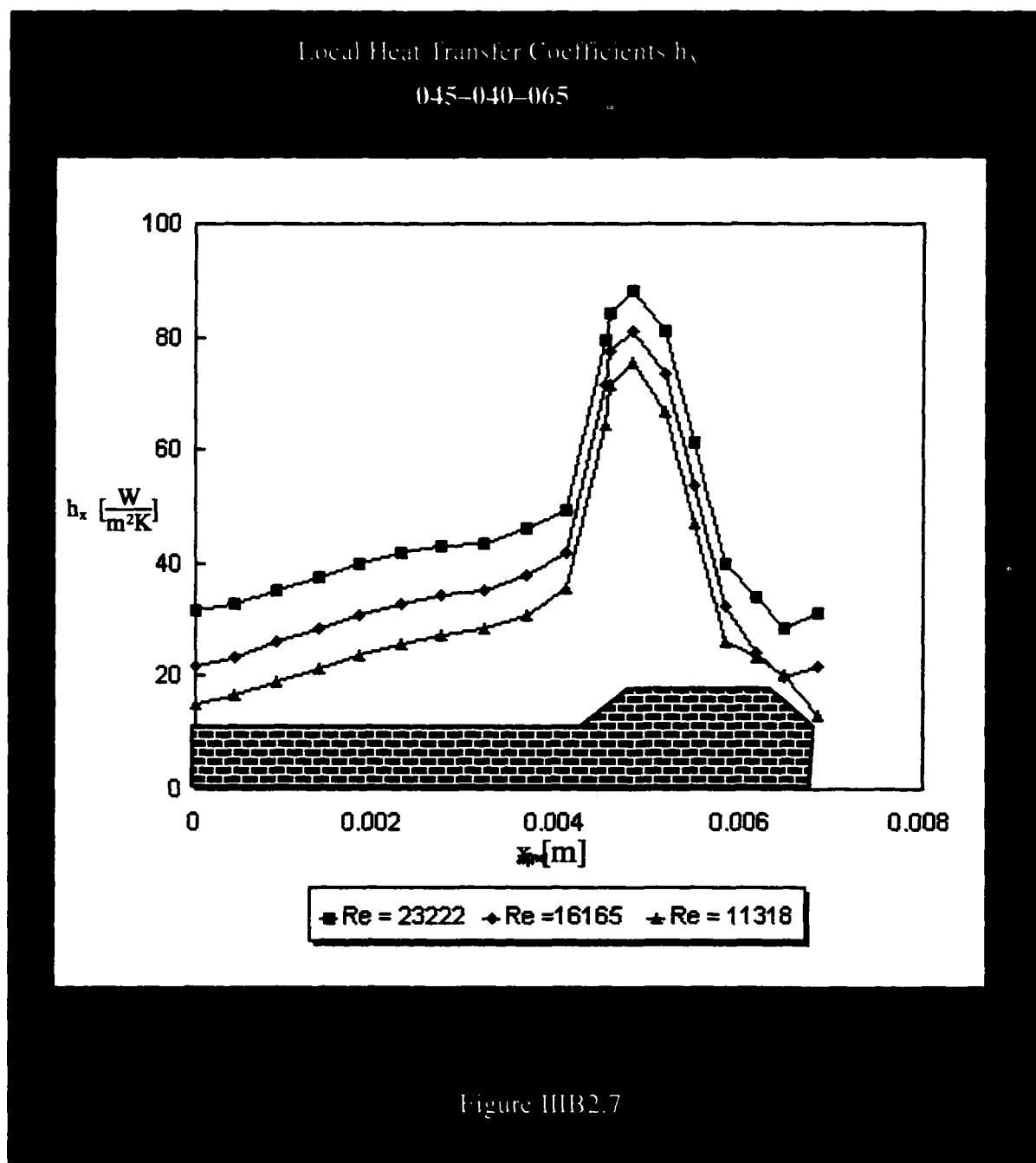
This is a very small value that supports the assumption of constant air temperature. Because the measurements were done at the mid-point of the heating block length, the correction of temperature should be  $0.6 \text{ C}^\circ$  from the measurement of the thermocouple in the air stream. It is also important that no losses to the environment were considered in the former analysis. If the consideration of losses to the ambient is made the resulting temperature build-up will be yet smaller.

The first attempt to run these computations was to input a smooth curve for the temperature on top of the repeating unit. The results showed an excessive amount of noise in the output values of  $q_{i_x}$ . This effect was much higher on points right on top of corners and diverging section of the geometry. The problem was solved by using a piecewise function to describe  $T_{c_x}$ . Because the upper part of the repeating unit has a piecewise continuous boundary, the numerical solution was smoother when a piece-wise temperature profile was used.

This was pointed out by Gibbs's ( Carslaw , 1950 ) phenomenon in the use of Fourier series to solve harmonic equations. The fact is that with the use of the piece-wise function the profiles of  $q_{i_x}$  turned out to be very smooth and lacked any noise at those critical points. To illustrate the difference between the two different approaches (smooth and piece-wise) Figure IIB2.6 shows the  $h_x$  profile for the repeating unit of the pipe 045-040-065 that was obtained with the two different procedures.



Finally, Figures IIB2.7,8,9 show local heat transfer coefficients  $h_x$  for all the experiments carried out. Also included on the figures are the  $N_{Re}$  corresponding to each experiment and the geometry of the repeating unit over which  $h_x$  develops.



Local Heat Transfer Coefficients  $h_x$   
040-040-035

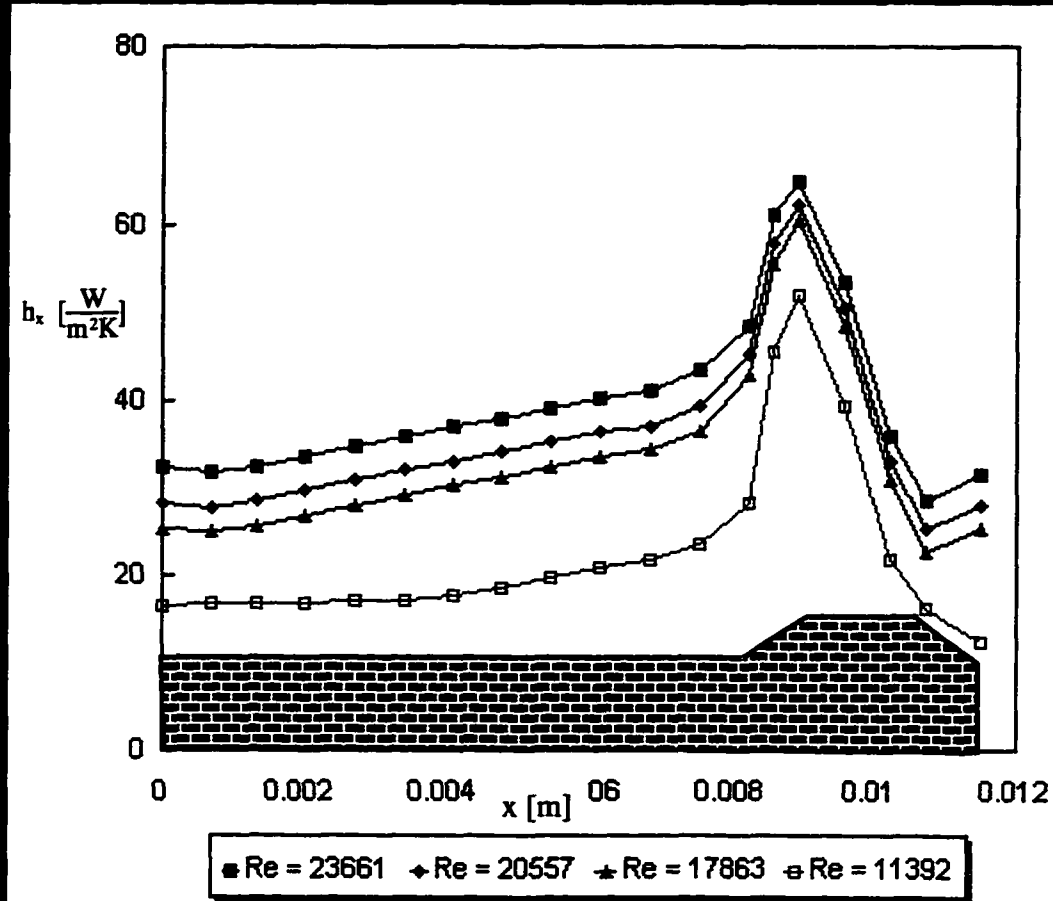
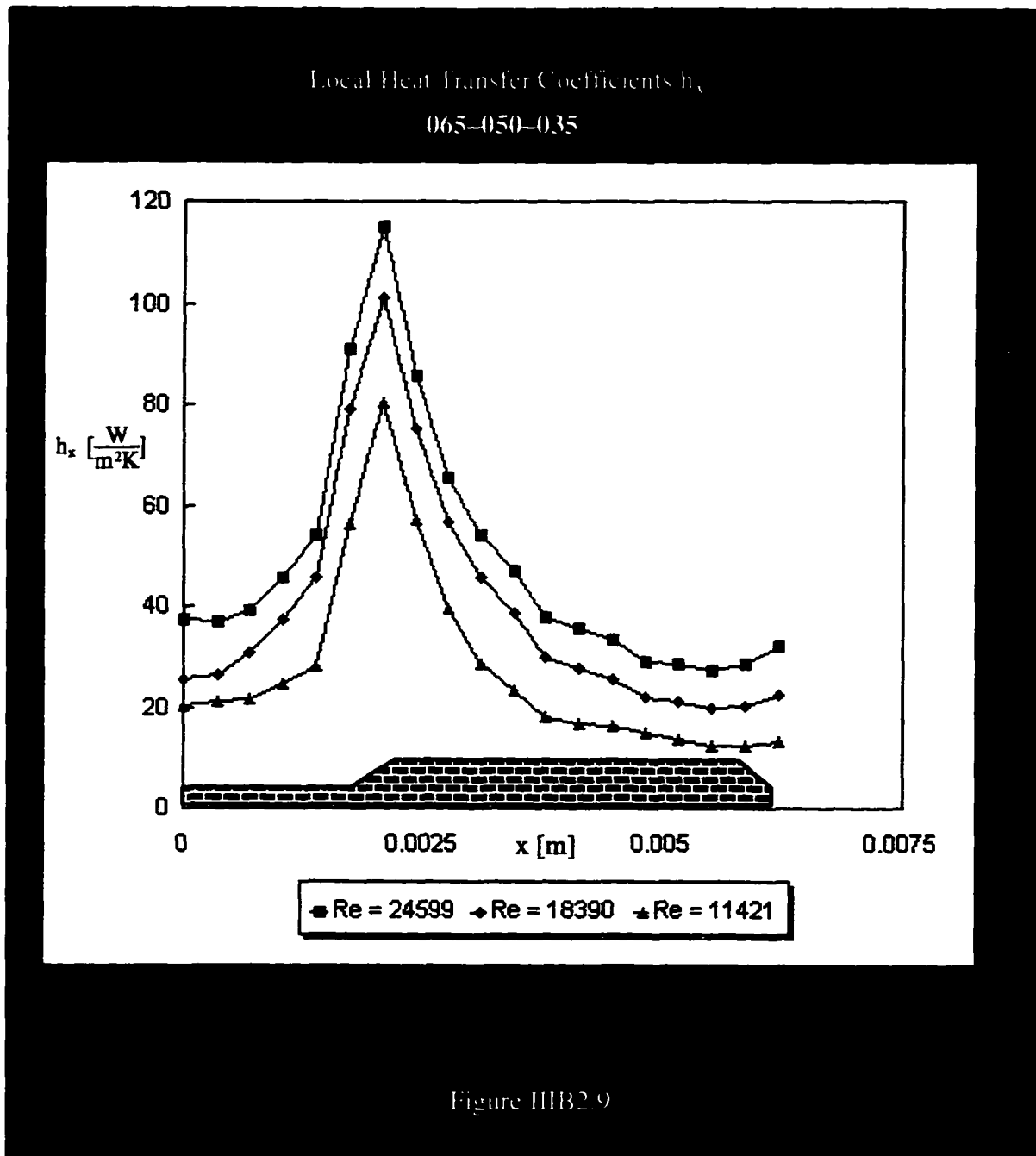


Figure HIB2.8



### III.B.3 Average heat transfer coefficients $\langle h \rangle$ from $h_x$ profiles.

Once the local heat transfer coefficients were acquired the values of the Average heat transfer coefficients were calculated for the corresponding  $N_{Re}$ . This was achieved simply by integrating numerically the values of  $h_x$  along the upper surface of the repeating units:

$$\langle h \rangle_{N_{Re}} = \frac{1}{l_0} \int_0^{l_0} h_x dx \quad \text{Where } l_0 = P - 2b + 2h$$

In this manner the average heat transfer coefficients were calculated for each pipe at each  $N_{Re}$ . Figure III.B.3.1 shows the results for the three models of pipe that were analyzed.

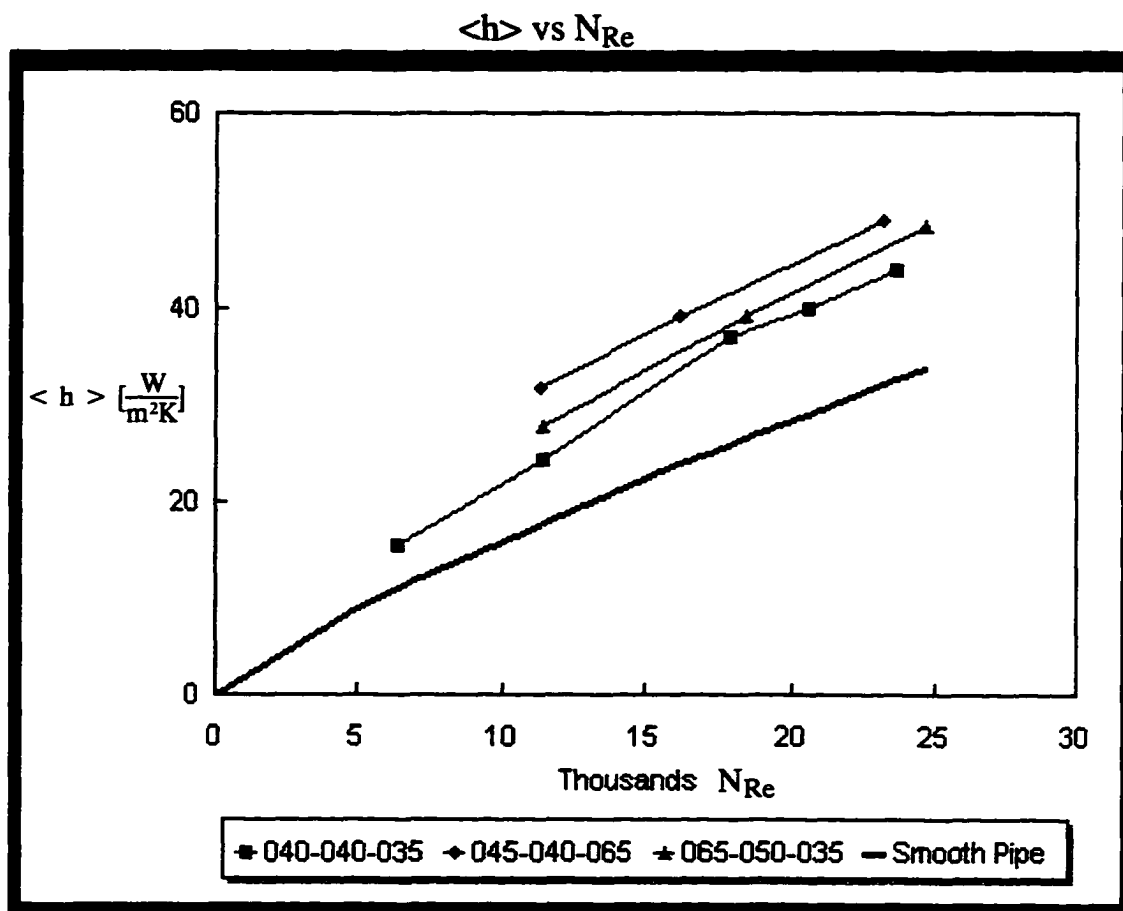


Figure III.B.3.1

For some cases like the 065–050–035 pipe, it was very difficult to get a wide span of flow rates with its corresponding  $h_x$ . The goal of the adjustment of voltage and flow rate was to get the temperature profile with the highest distribution of colors on it. Therefore, many intermediate profiles were discarded as unsuitable for the construction of a temperature profile on top of the repeating unit.

### III.C Laser Doppler Velocimetry (LDV)

#### III.C.1 Laser Doppler Velocimetry Technique

The Laser Doppler Velocimetry technique was used to analyze the fluid dynamic characteristics of both air and water flow. The complex theory behind LDV is not the purpose of this work. However, some implementation procedures will be explained as will some tips to make the measurements easier and more reliable. The reader may find this very helpful for applying the Laser Doppler technique. The instrument used for LDV was a commercial model manufactured by TSI inc. ( St. Paul, MN) . It consisted of a four beam probe model 9253–350 connected to a two dimensional flow analyzer IFA650 data processor. The processor was connected to a 486 PC GATEWAY 2000 that was the control interface. On this PC was the data acquisition program (FIND–TSI) that was the remote control of the system.

The LDV consisted of a probe with four beams that intersected at a point 350mm away from the probe (focal distance of the probe lense). This point is common for the four beams. The point called measuring volume had a dimension of  $100\ \mu$  by  $50\ \mu$  . Two of the beams were on the plane  $x,y$  and were responsible for measuring the velocity in the 'x' direction. These two beams were of the same color (same frequency) only shifted in 40MHz one to the other. This 'shift' in frequency generated moving fringes of interference at the intersection point. When the particles suspended in a liquid cross the measuring volume, they will generate a Doppler



signal or burst that will be detected by 'back scattering' on a photoreceptor inside the same probe. Like an actor going through the curtains of a theater, the particles will deform those fringes that they cross. The deformation of the curtain with respect to its vertical and natural position is the Doppler signal detected by the photoreceptor in the case of fringes. The faster the actor crosses the curtains the stronger the curtains will flap. The two remaining beams were exactly like the ones described before but on the plane  $y,z$  and were responsible for measuring the velocity in the  $z$  direction. See Figure III.C.1.1.

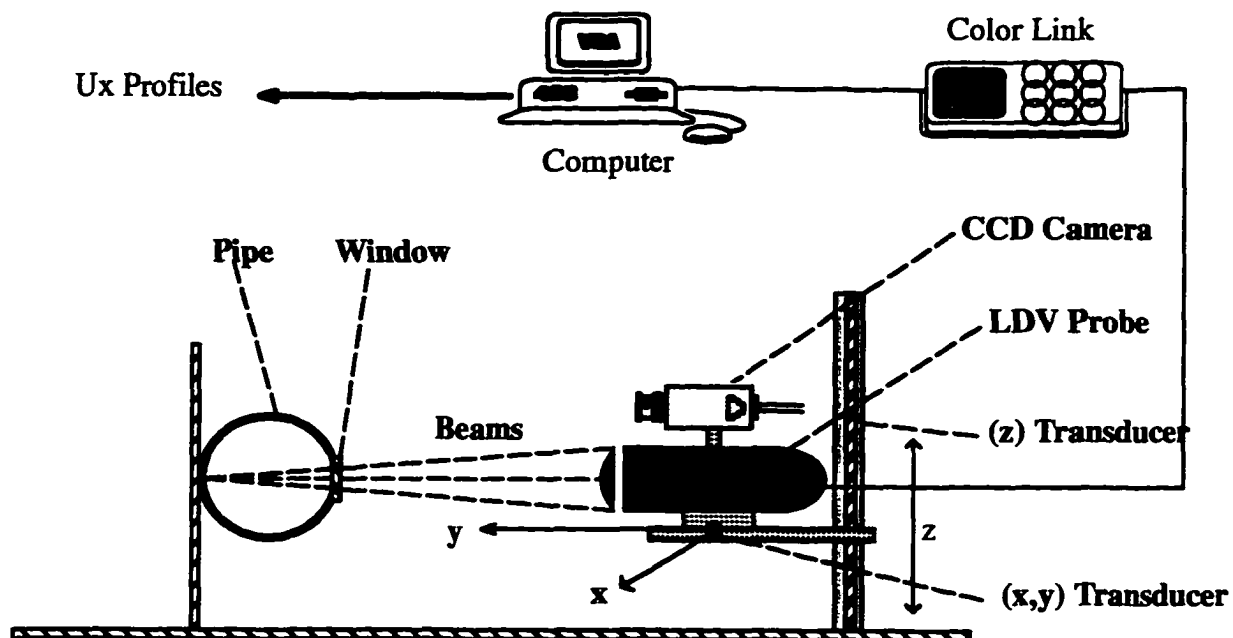


Figure III.C.1.1

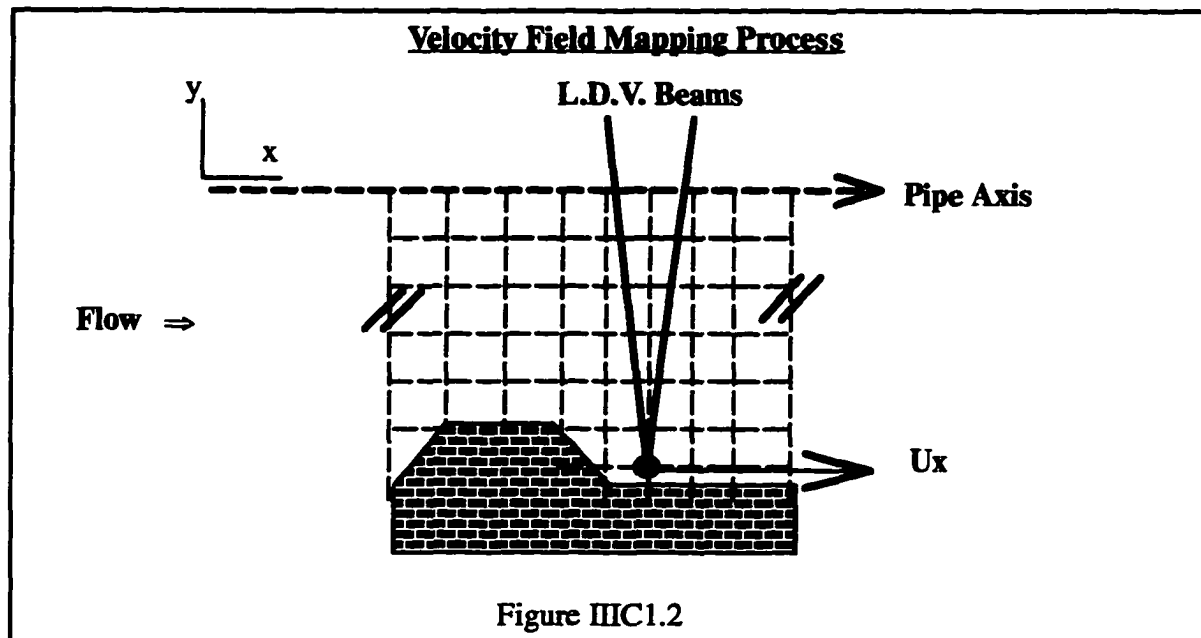
The advantage of the model of LDV used was that the photoreceptor was included in the probe that generates the beams. The signals were carried to the IF650 processor through fiber optics contributing to the the simplicity of its operation. The signals detected by the probe were shown on the screen of the computer on a %–Velocity graph. This told the operator which

percentage of the acquired bursts had which velocity. A 'good' signal in LDV is considered to be a thin pick of bursts on the computer screen with its center at the average velocity. This average must not be mistaken with the fluid flow average velocity in space. The average velocity reported by the LDV at each point, was an average in time of all the bursts occasioned by the particles in the fluid. It is the average of velocities in time on a particular point in space. Of the diverse types of data that were outputted by the processor, this work was concerned about  $U_x$  (velocity in the axial direction),  $V_y$  (angular velocity) and both  $u'$  and  $v'$  (turbulence intensities). For further explanation this system of coordinates will be the same taking  $x$ , to be the direction of the pipe axis (direction of the main flow). The measurements were done through the observation window described in section IIIA.

The way that the probe was held in front of the window is shown on Figure III.C.1.1. The probe was attached to a system of translators that allowed the probe to be moved in the plane  $(x,y)$ . These translators manufactured by Mitutoyo ( Japan ) were as accurate as 0.001 mm with a digital display indicating the position. The two translators rested on an ORIEL metal plate attached to a vertical translator that allowed movement in the direction  $z$ . This type of array was very comfortable for the mapping process and it was only possible because the LDV model used was 'state of the art' equipment. LDV measurements in the past were very difficult because the beams had to be aligned by hand and the photo detector had to be placed exactly behind the measuring point in forward scattering fashion. The whole probe stand was attached to an ORIEL anti-vibrational bench.

The mapping process consisted of measuring points along the  $y$ , direction starting with zero at the pipe wall right in front of the window. With the aid of the  $y$ , translator the measurements were taken point-by-point until reaching the center of the pipe. Once this point was reached, the probe was moved with the  $x$ , translator. Now, starting from the center of the pipe, the  $y$ , translator displaced the measuring volume until reaching the front wall. This

procedure was repeated until a whole repeating unit was swept in the 'x' direction on the rib/valley surface. Figure III.C.1.2 shows the typical mapping points on a repeating unit.



The mapping process consisted of measuring velocity profiles in the radial direction at different positions in the axial direction, from the wall to the center of the pipe. In the case of the mapping process with water flow particles were added to the solution to produce the Doppler burst. These particles, also manufactured by TSI, were aluminum coated polyethylene micro pellets of  $5\mu$  in size. They were extremely brilliant but light. These particles were added to the reservoir tank of the setup described in section III.A. Turbulence and mixing took care of keeping the particles in suspension. It was very important to keep the solution clean and translucent. For this purpose, prior to mapping, it was necessary to run the setup with the filter system on. Turbidity and debris in the solution produced a reduction in the intensity of the back scattered signal detected by the photoreceptor and, consequently, a reduction in the accuracy of the measurements. This filtration process resulted in the loss of the particles of prior sessions into

the filter; however, the amount of particles needed was so small that this was not considered a problem.

A correction to the 'y' position for refractive index was needed in the case of water flow. When the laser beams crossed the glass window from the air into the water, the phenomenon of refraction displaced the intersection point of the beams to a position closer to the probe. In this way the read-out of the translators was not indicating the real position of the measuring volume of the laser. This problem was easily solved by analyzing the beams path. This analysis is outside the interest of this work and can be found in the operation manual provided by the manufacturers of the LDV ( TSI). However the correction factor is introduced as follows:

$$y_r = y_{\text{aparent}} \times \frac{n_{\text{water}}}{n_{\text{air}}}$$

$n_{\text{water}}$  = Index of refraction of water

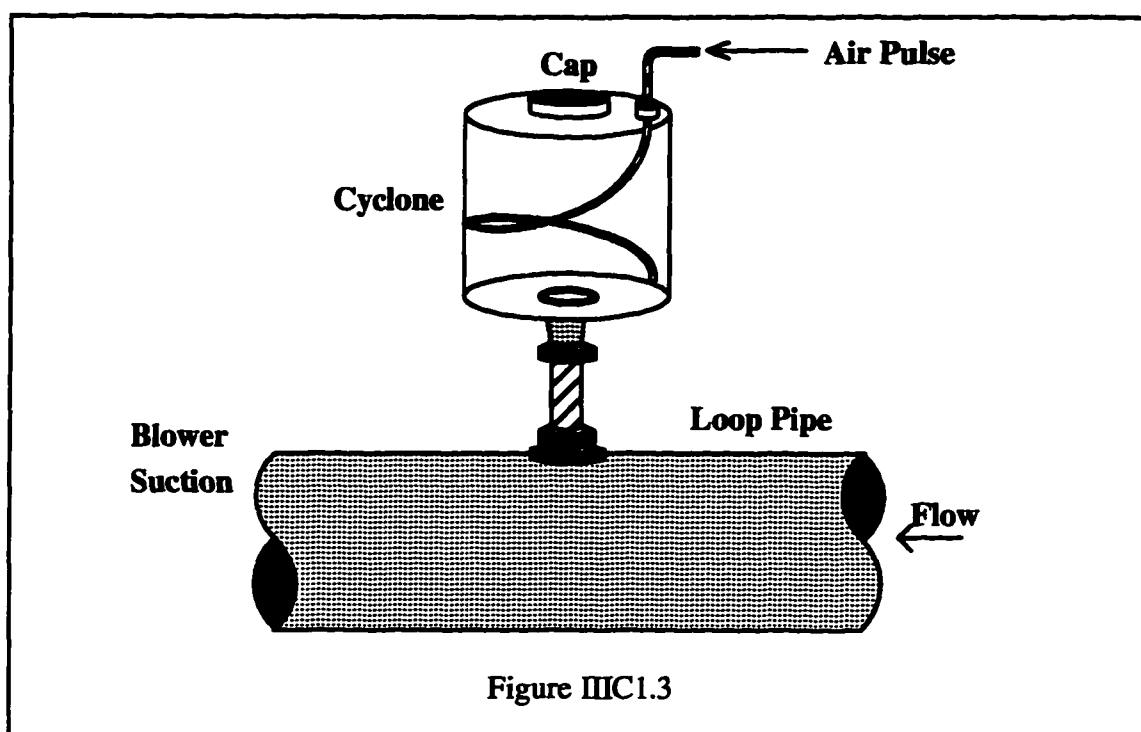
$n_{\text{air}}$  = Index of refraction of air

$y_{\text{aparent}}$  = Translator read-out.

$y_r$  = Real position of the measuring volume.

$$\frac{n_{\text{water}}}{n_{\text{air}}} = 1.3418$$

In the case of air flow, the probe array was the same as the one described for water in Figure III.C.1.1. In the air mapping process the problem of keeping particles in suspension was more difficult to solve. Given the small ID of the pipes plus the levels of turbulence in each one of the turns of the loop, the particles did not sustain in the stream but deposited on the bottom of the pipes. The particles used for the air flow mapping were 5 $\mu$  alumina powder. The problem of the suspension of the particles was solved with a simple but ingenious device. See Figure III.C.1.3.



It consisted of a small cylindrical cyclone, 10cm. high and 5cm. in diameter. In the upper lid of the vessel, an orifice allowed the entrance of a 1mm ID chromatography tubing. This tube, once inside of the cyclone, reached the bottom and made a half turn parallel to the walls of the vessel. The bottom lid of the cyclone had an orifice of 6mm, followed by a 6mm ID tube connected to the air loop prior to the blower in the suction region. The cyclone was filled with alumina through an aperture on top and sealed. Once the blower was started, a small stream of air was pumped into the cyclone through the tubing on top. This was done each time before the data acquisition with the LDV. The small air stream introduced was strong enough to induce a rotational circulation of the particles inside the cyclone. Once the particles were suspended in the cyclone they were sucked by the blower into the main stream of the loop. In this manner a high number of particles crossed the measuring volume of the LDV. Also, it was not necessary to continuously add particles, which would have resulted in having to keep an absurdly high quantity of particles in the loop.

Buildup of static electricity was also a concern in the air loop. The circulation of air through the pipe, coupled with the fact that the steel pipes were joined with plastic couplings, caused a build-up of static electricity in the loop. These charges made the particles stick to the observation window reaching points of zero back scattered signal by the LDV. The problem was solved by grounding the setup with copper wire; additionally, a small needle was attached in the interior of the pipe. Through this needle, high pressure air was blown whenever the window was too turbid. Of course, this cleaning procedure was not done simultaneously with the acquisition of data by the LDV. Finally, for both measurements of air and water the average velocity of the fluid was recorded with the mass flow meters. Also the ambient temperature and pressure drop at different flow rates for the three pipes analyzed were recorded. In the following session are introduced the results of the mapping process.

### III.2 Axial Velocities $U_x$ near wall region

Shown on Figures III.2.1,2,3,4,5,6 are the values of  $U_x$  in the near wall region at different positions on the repeating unit for air flow. These figures also include a small diagram of the repeating unit showing the positions to which each individual graph belongs. Figures III.2.7,8,9,10 are also measurements of  $U_x$  but with water flow.

Air 040-040-035

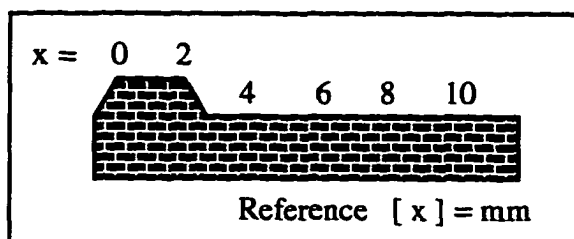
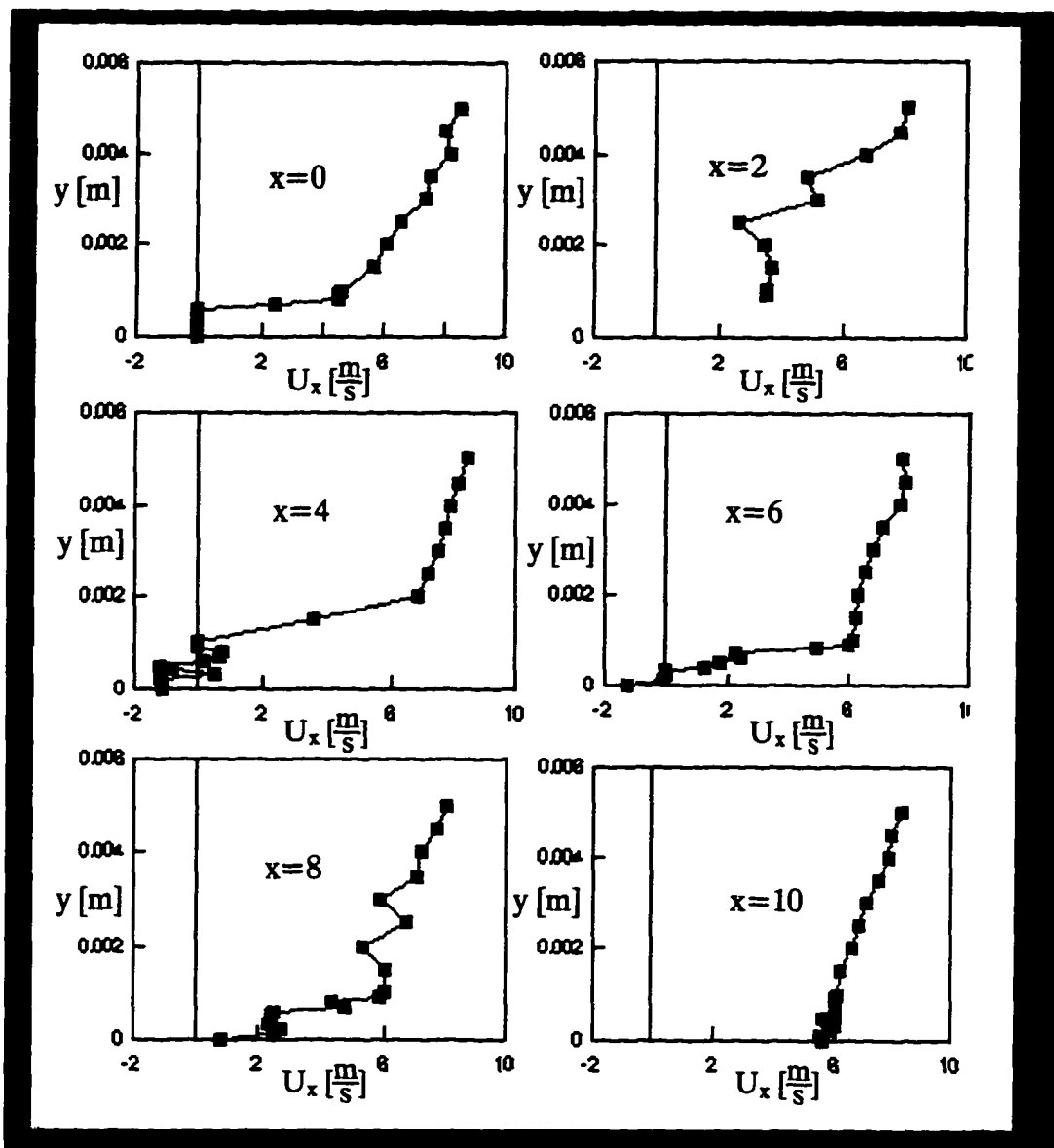
 $N_{Re} = 23000$ 

Figure III C2.1

## Air 040-040-035

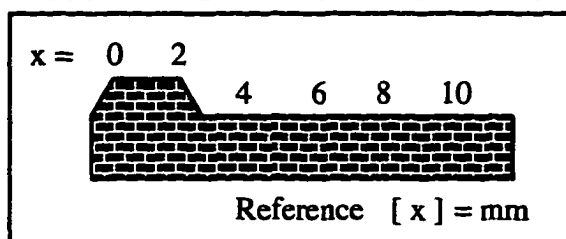
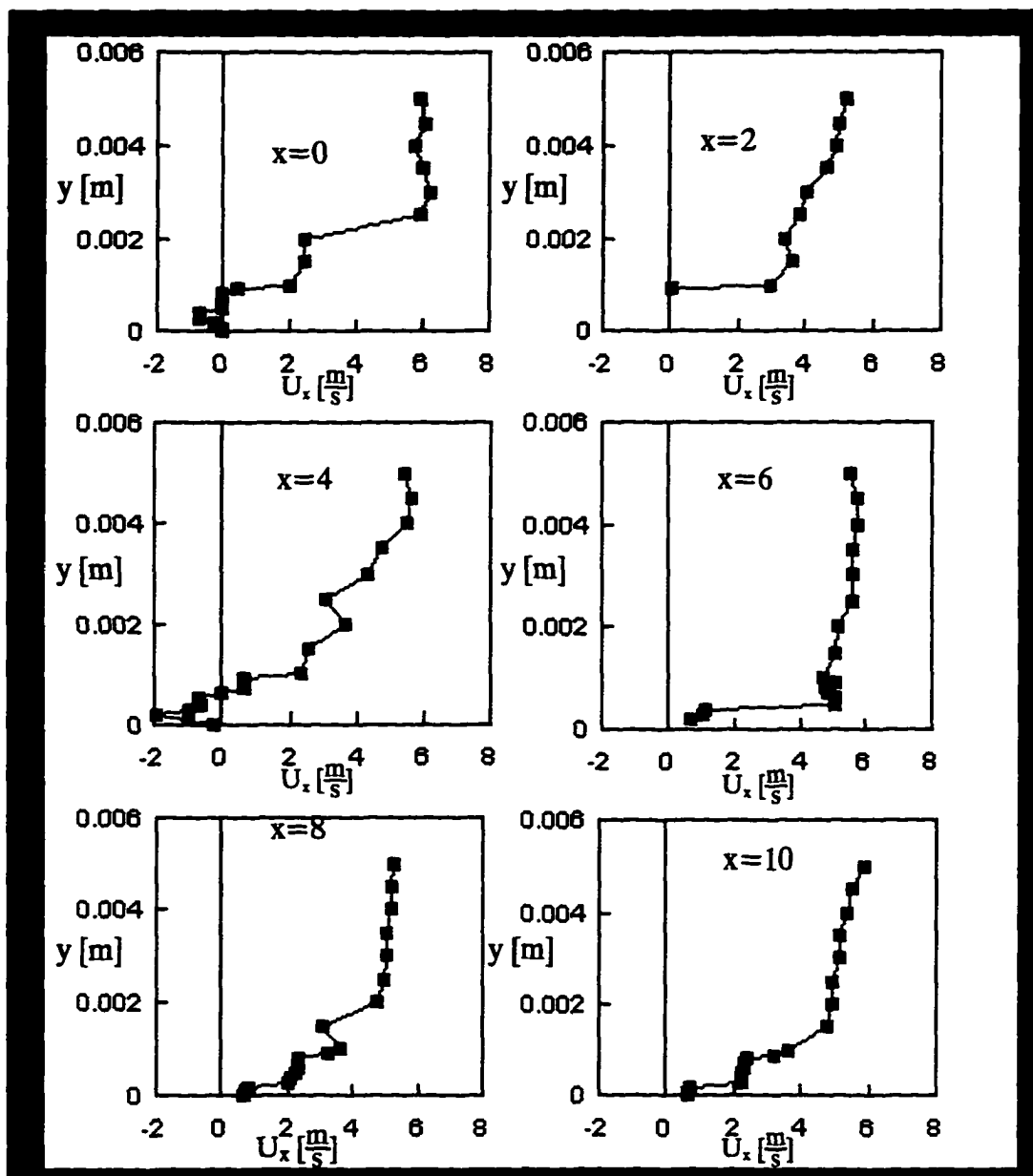

 $Re = 15500$ 

Figure IIC2.2



Air 045-040-065

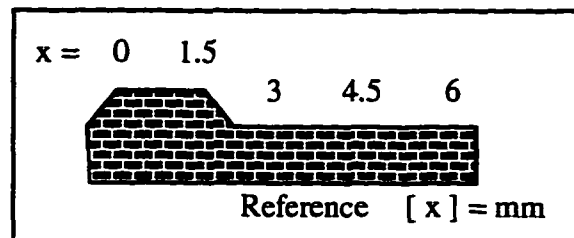
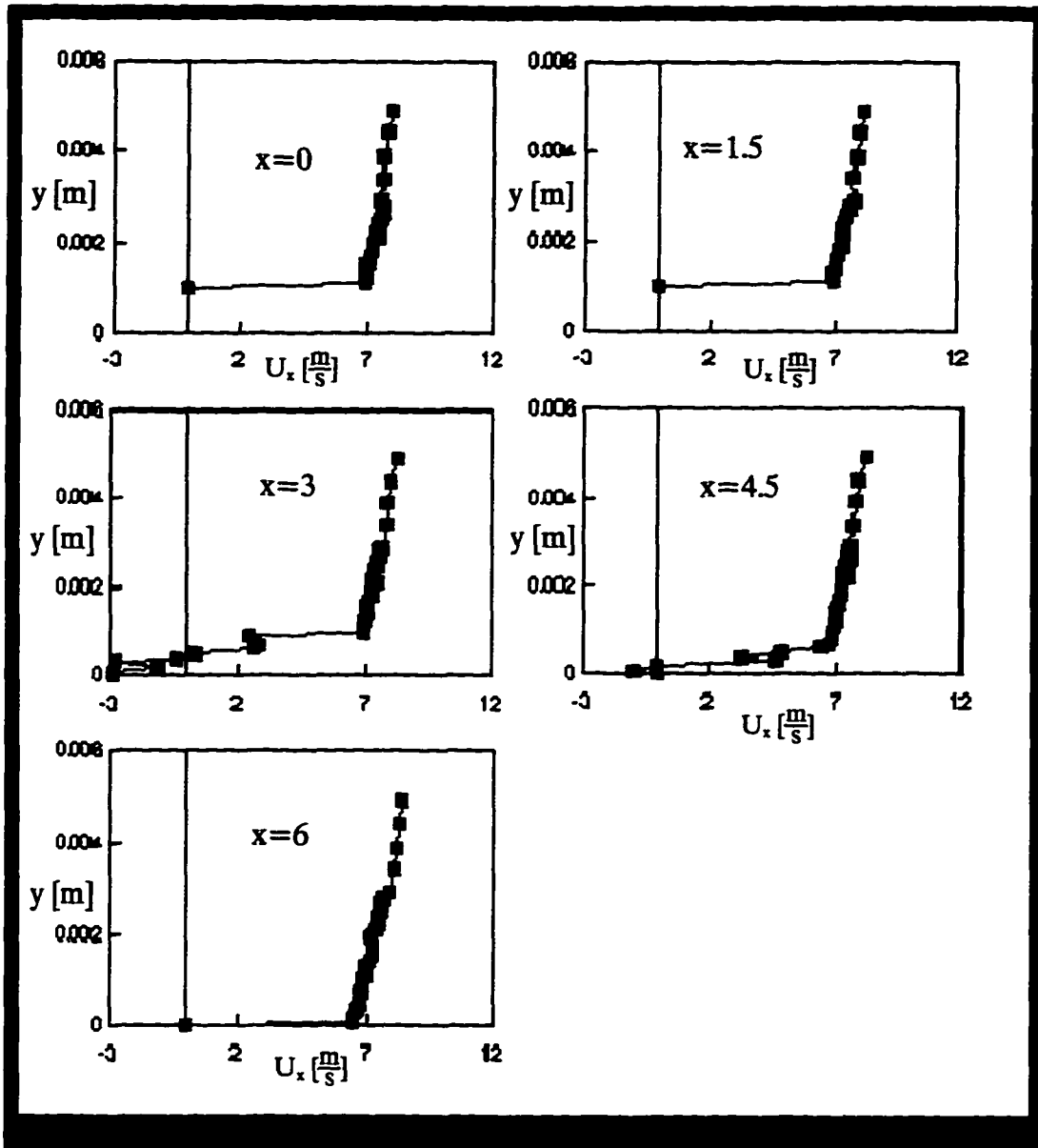
 $N_{Re} = 23000$ 

Figure IIC2.3

## Air 045-040-065

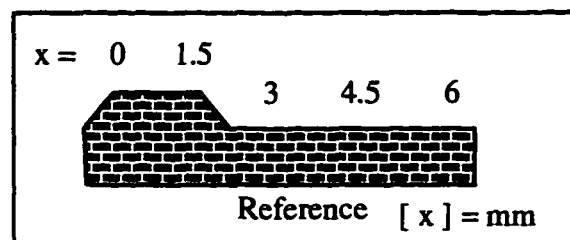
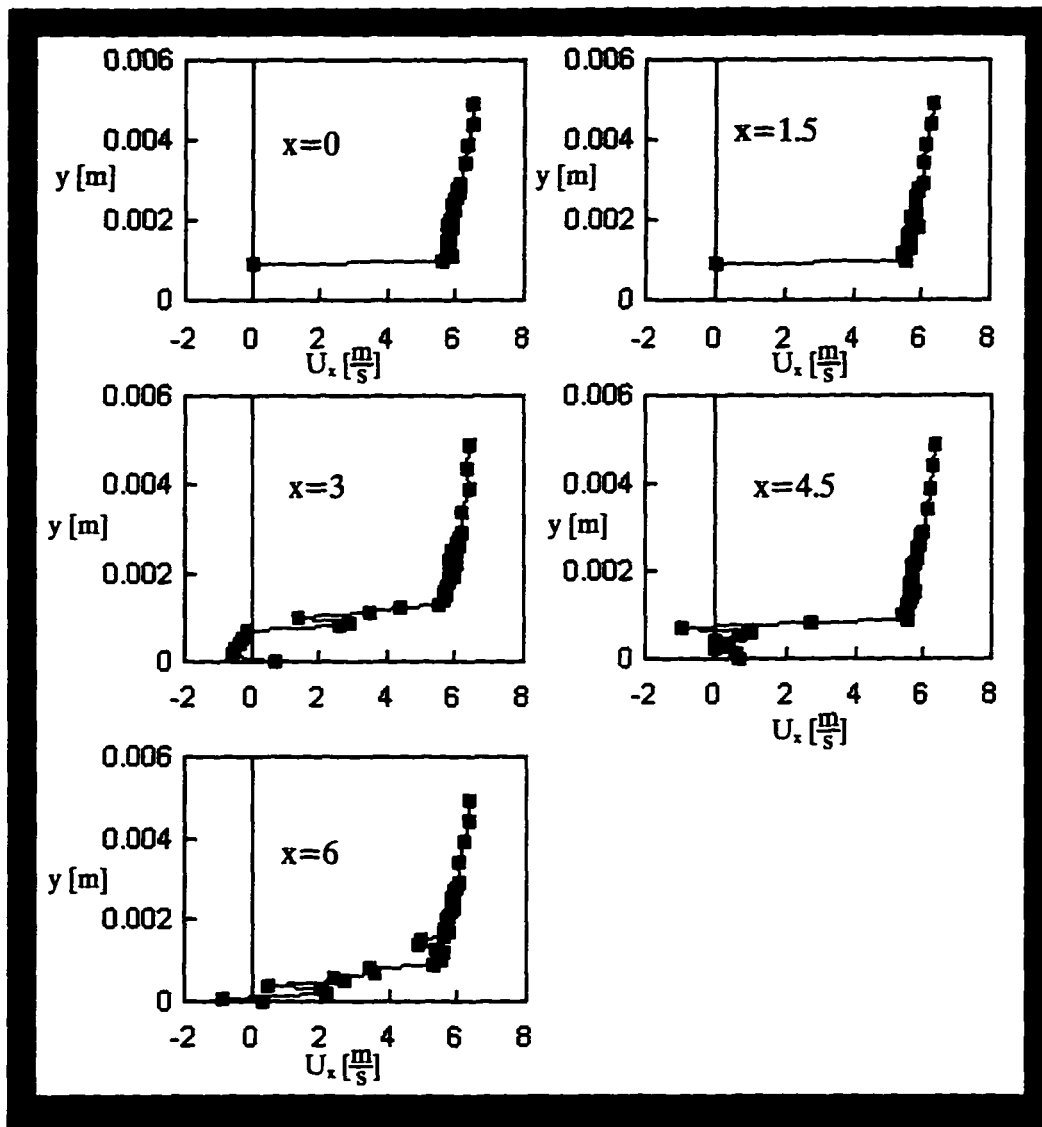
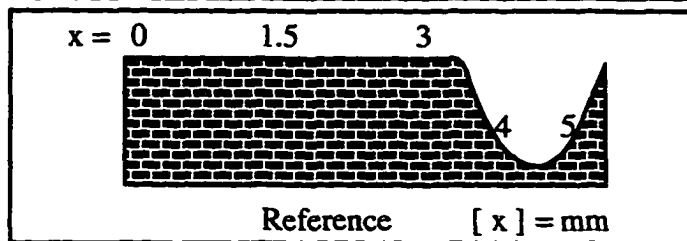
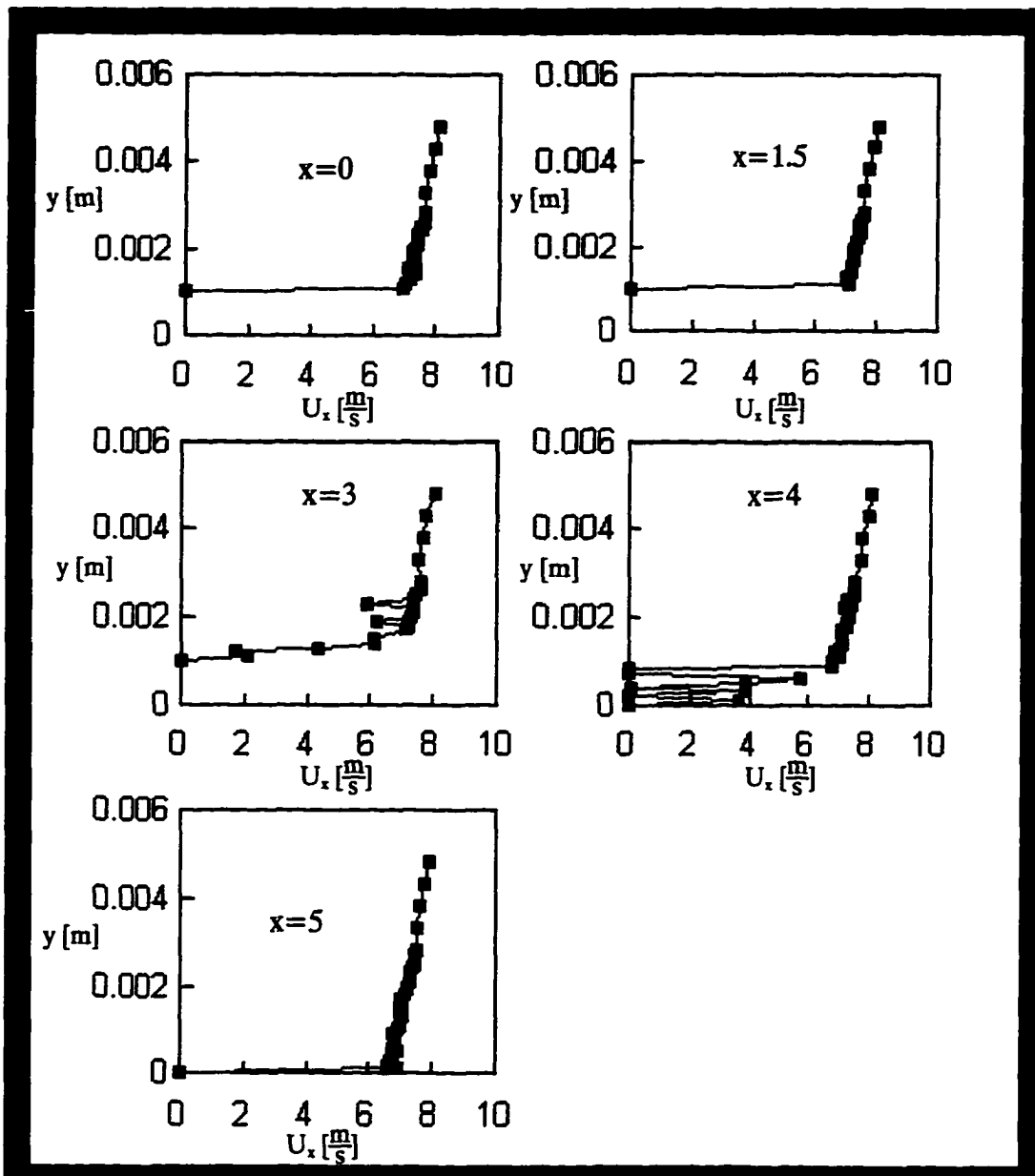

 $N_{Re} = 17500$ 

Figure III C2.4

Air 065-050-035



$N_{Re} = 22100$

Figure IIC2.5

Air 065-050-035

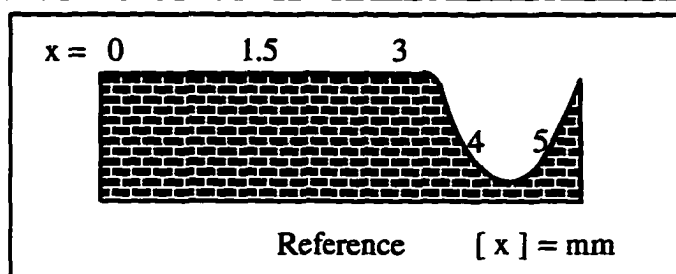
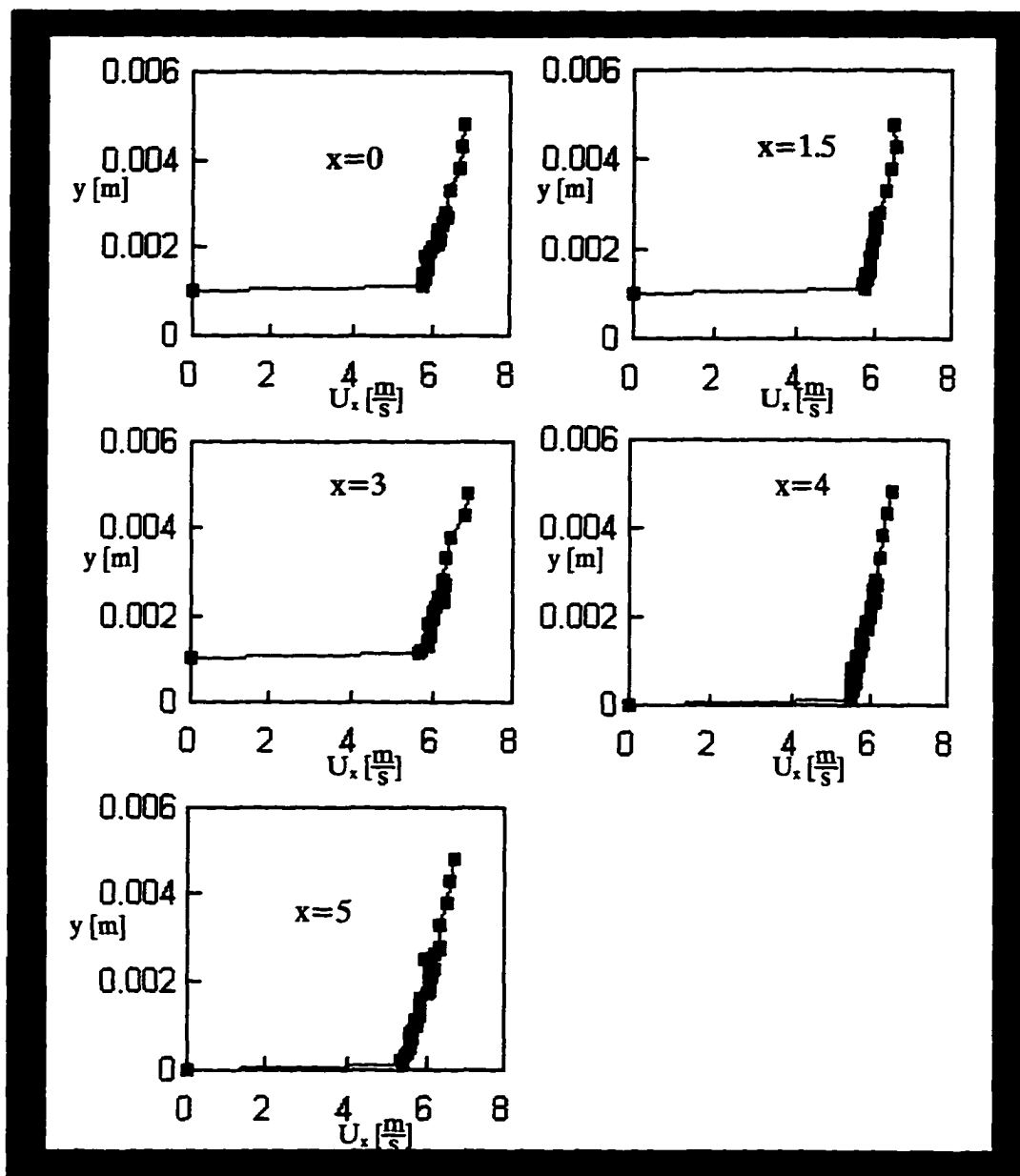
 $N_{Re} = 18500$ 

Figure III C2.6

## Water 065-050-035

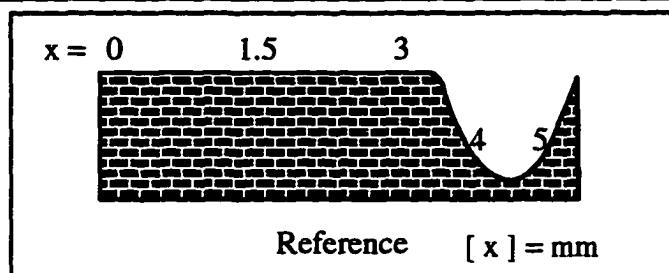
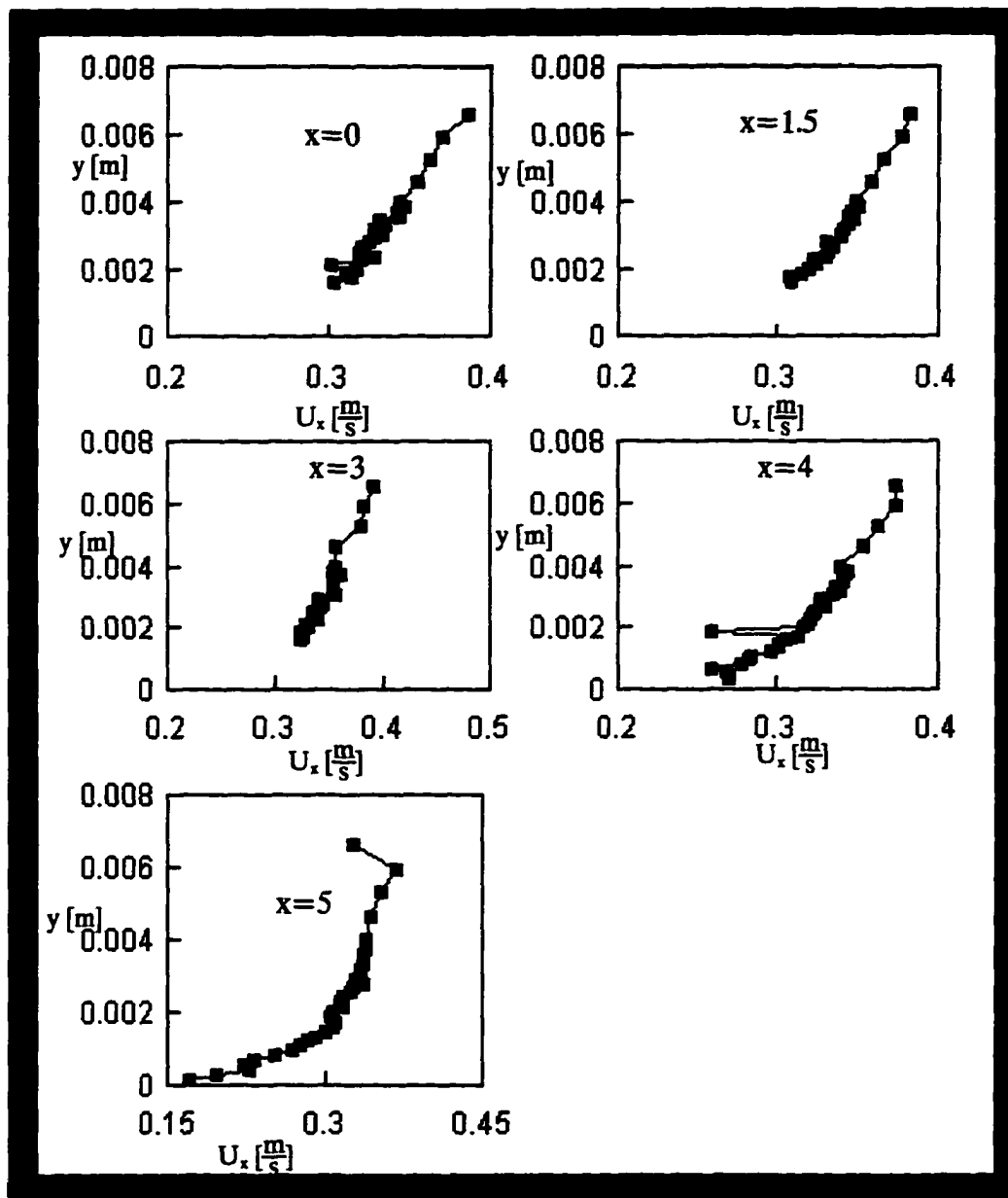

 $N_{Re} = 17000$ 

Figure IIC2.7

## Water 065-050-035

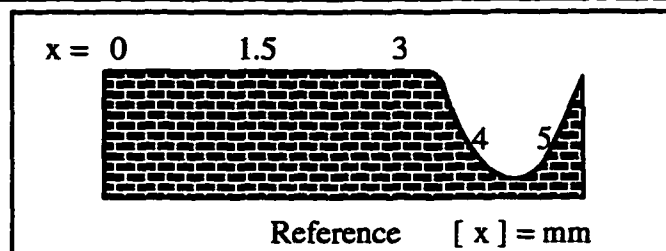
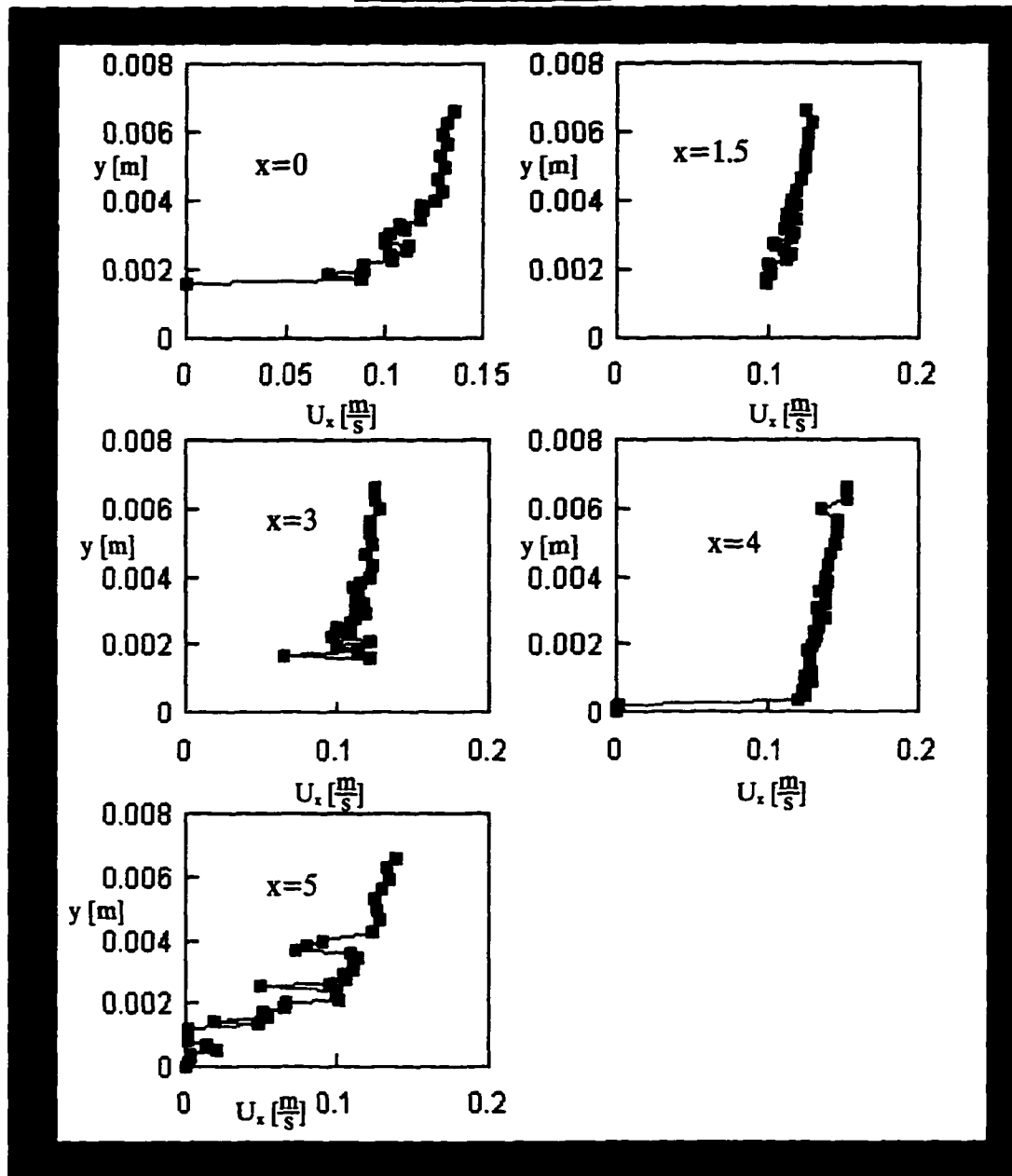

 $N_{Re} = 5500$ 

Figure IIC2.8

## Water 045-040-065

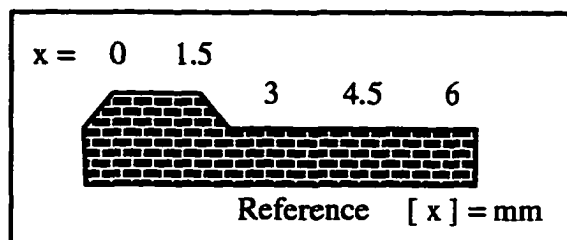
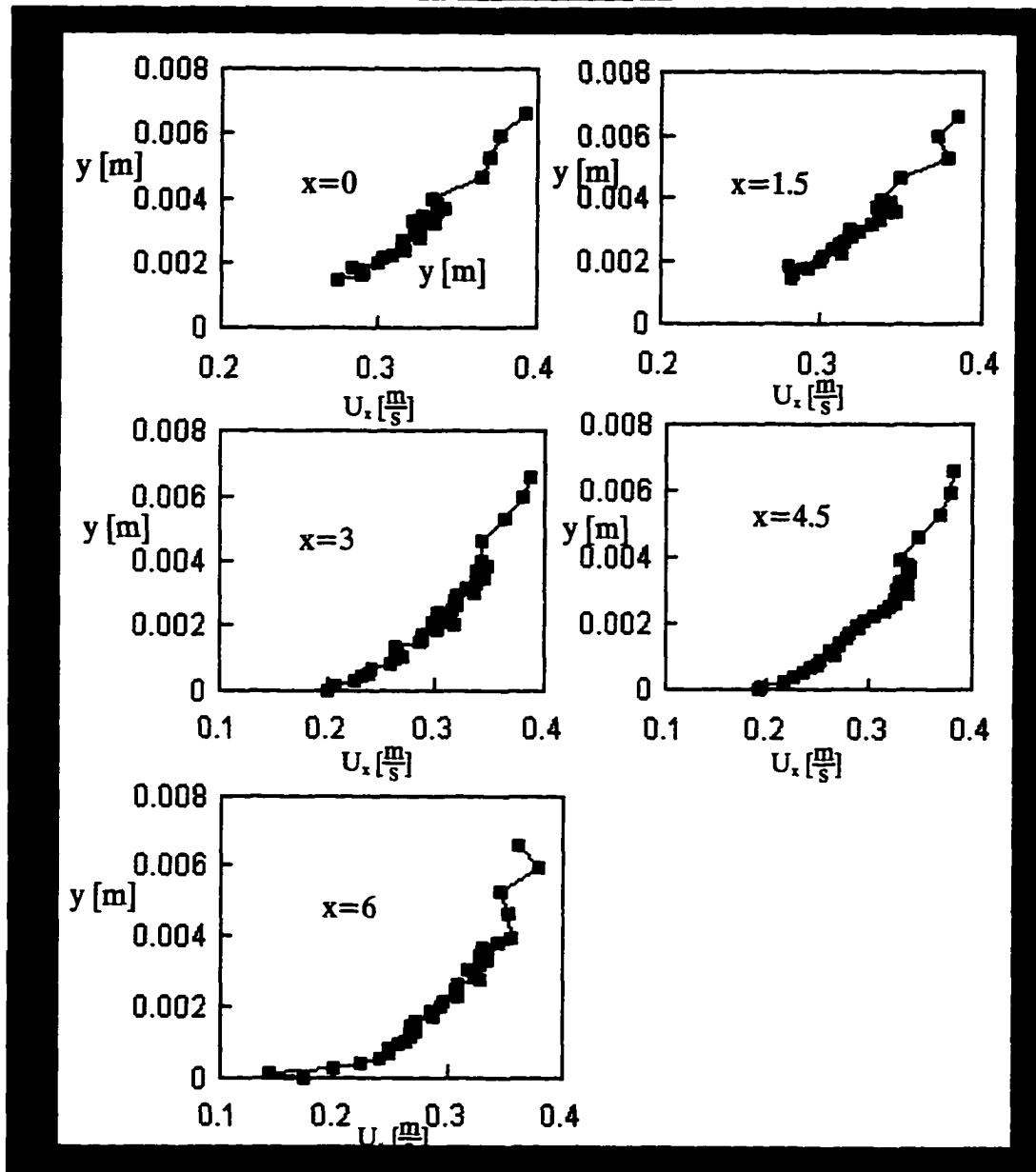

 $N_{Re} = 20000$ 

Figure IIC2.9

## Water 045-040-065

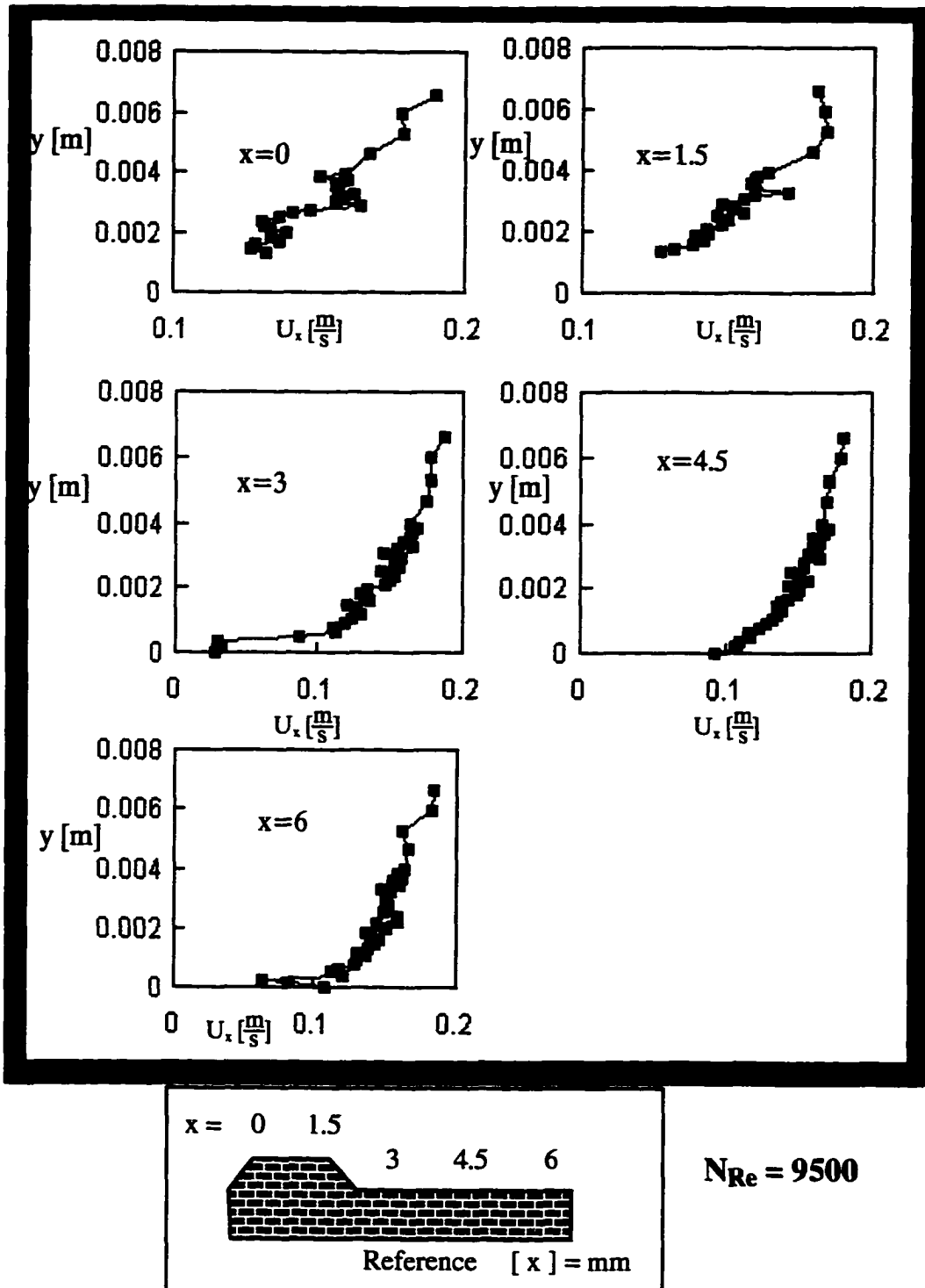
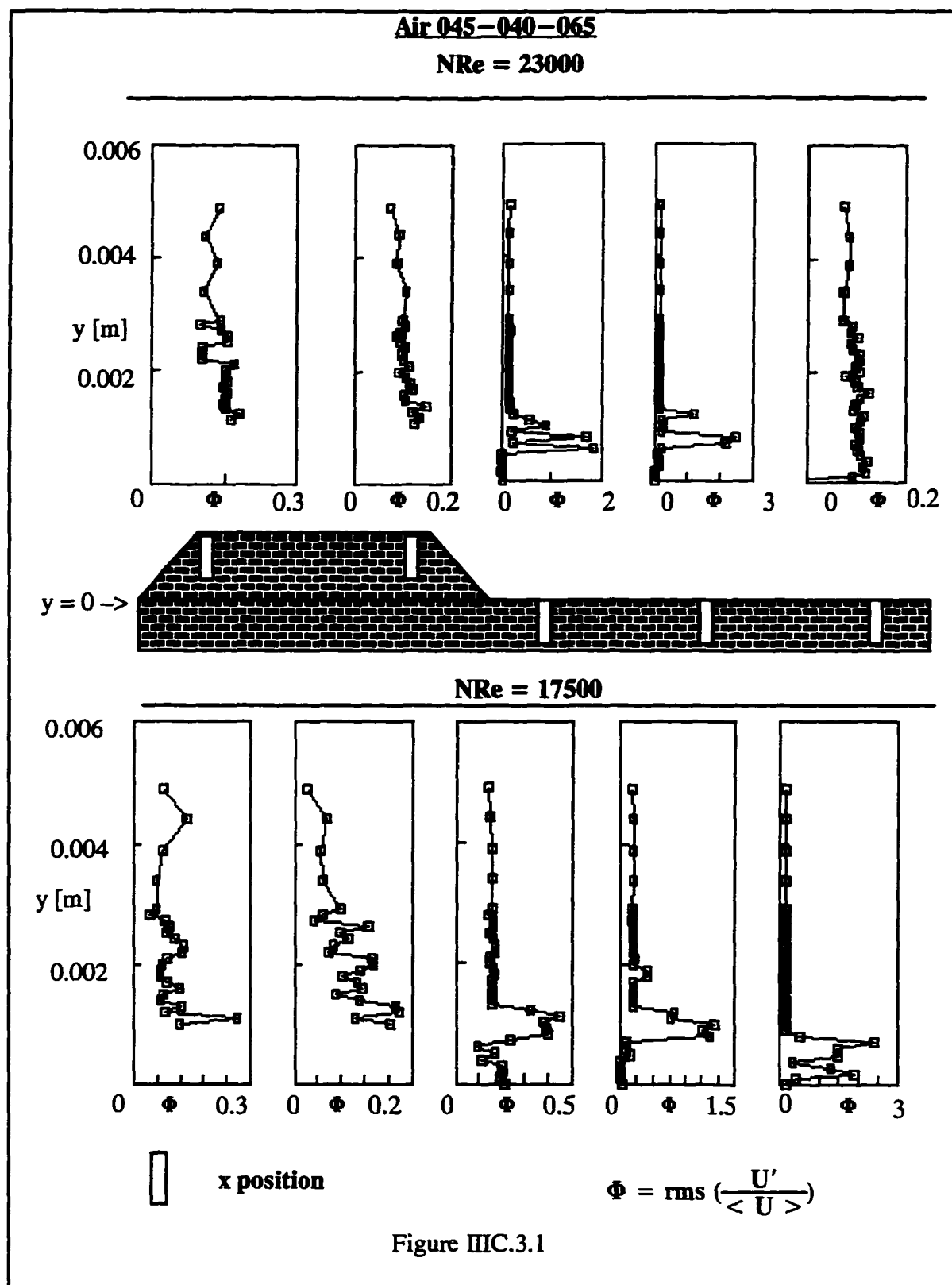


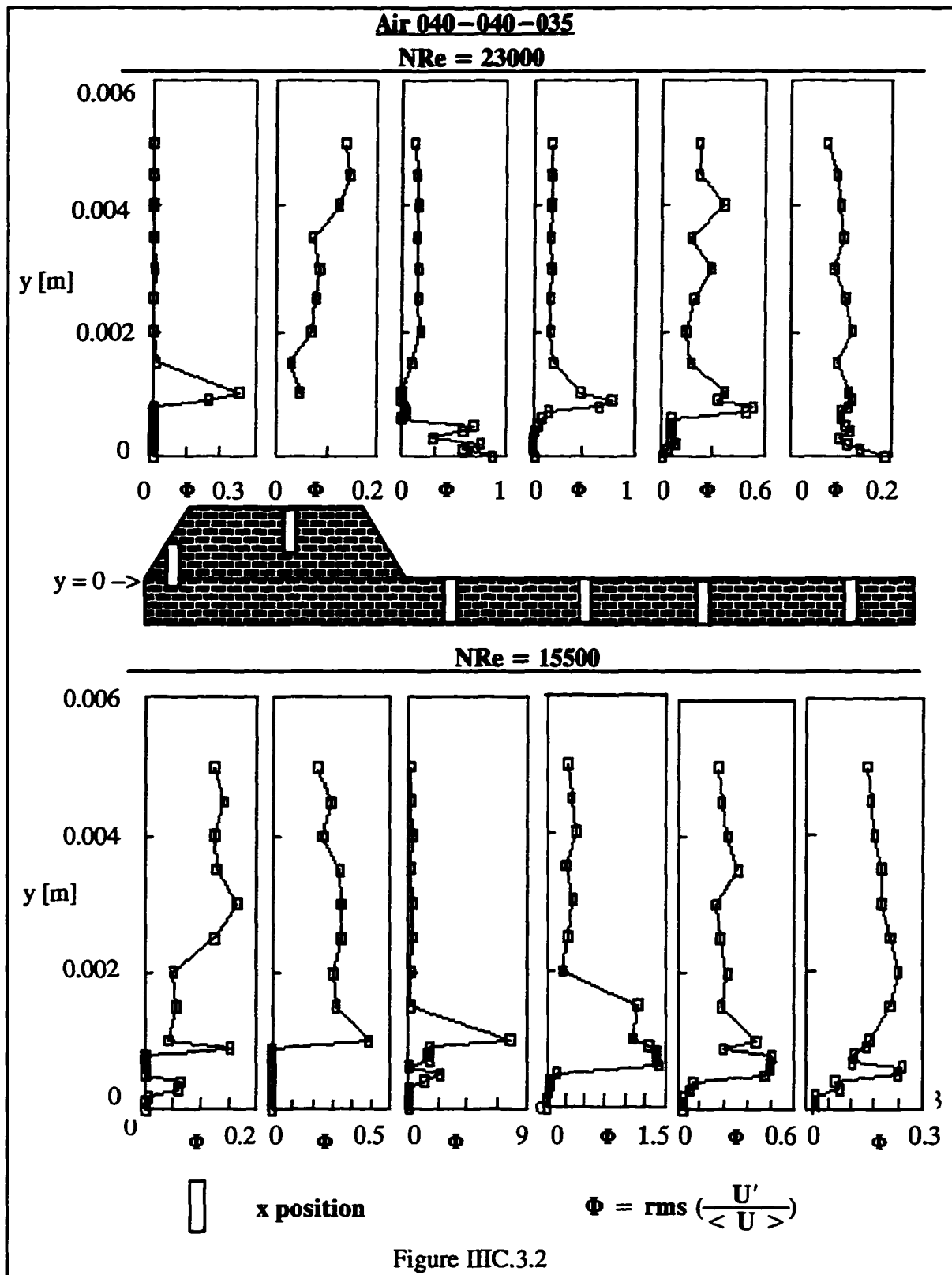
Figure IIC2.10

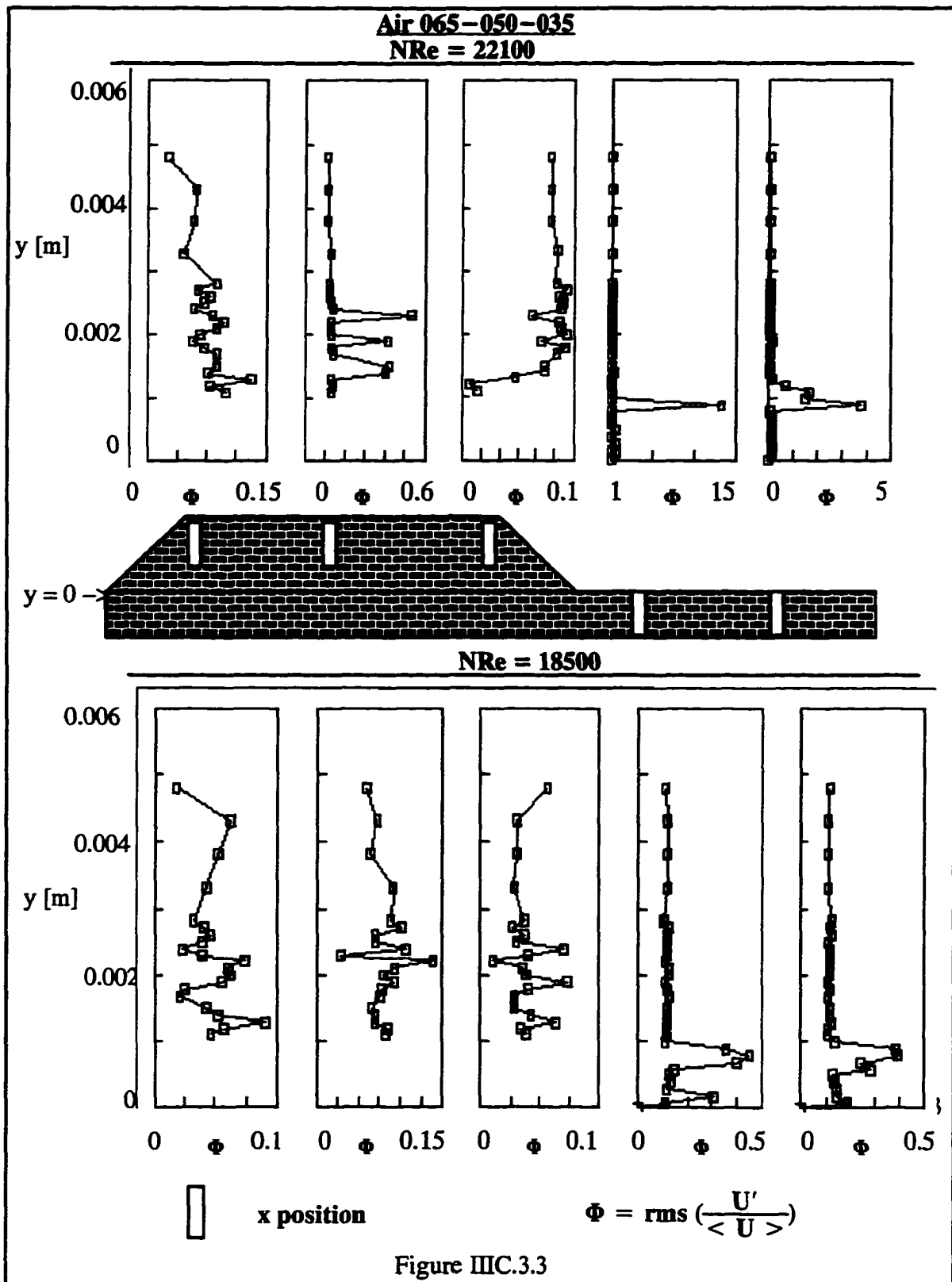


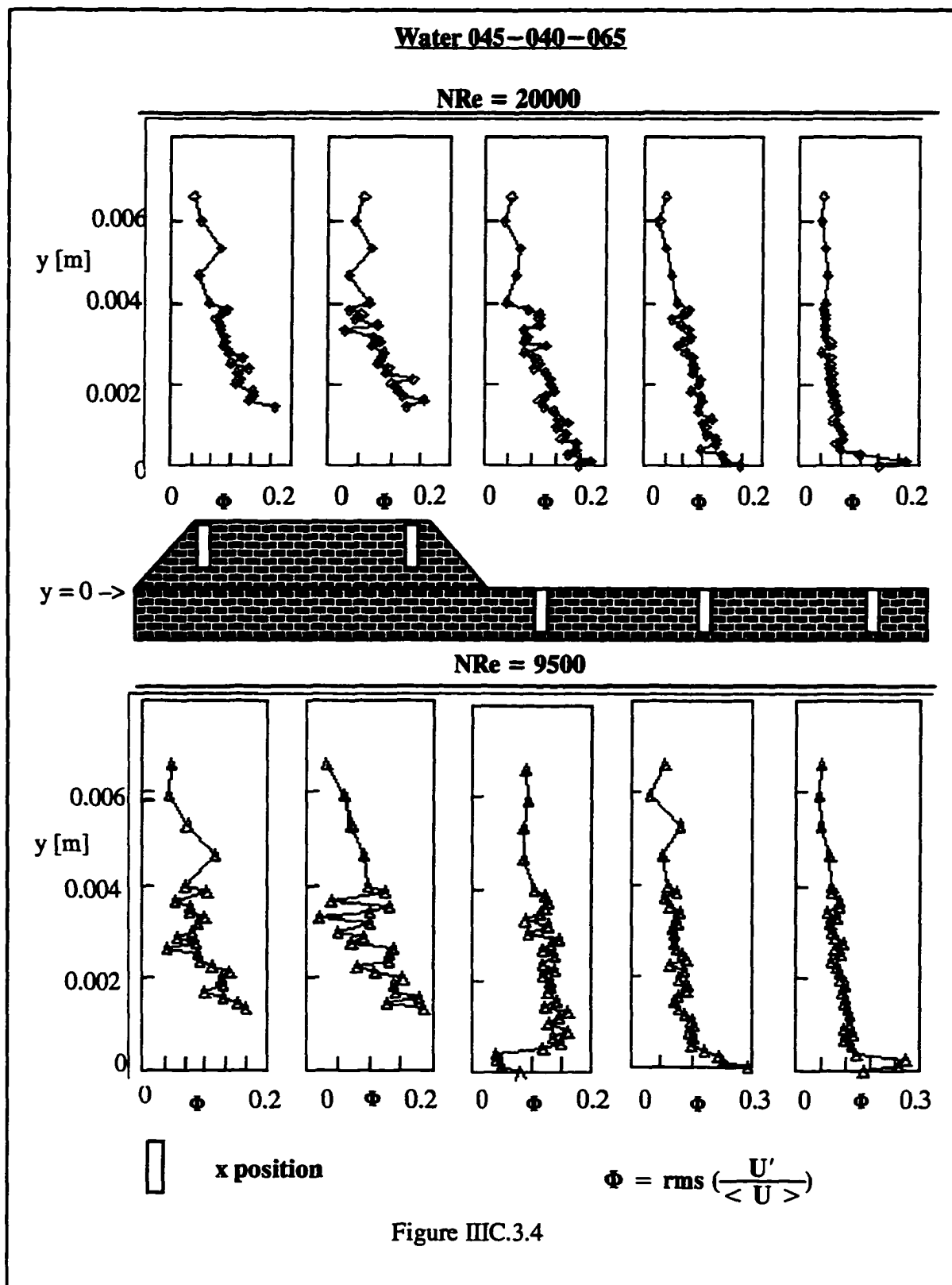
### III.C.3 Turbulence Intensities $\text{rms}(u'/\langle U \rangle)$

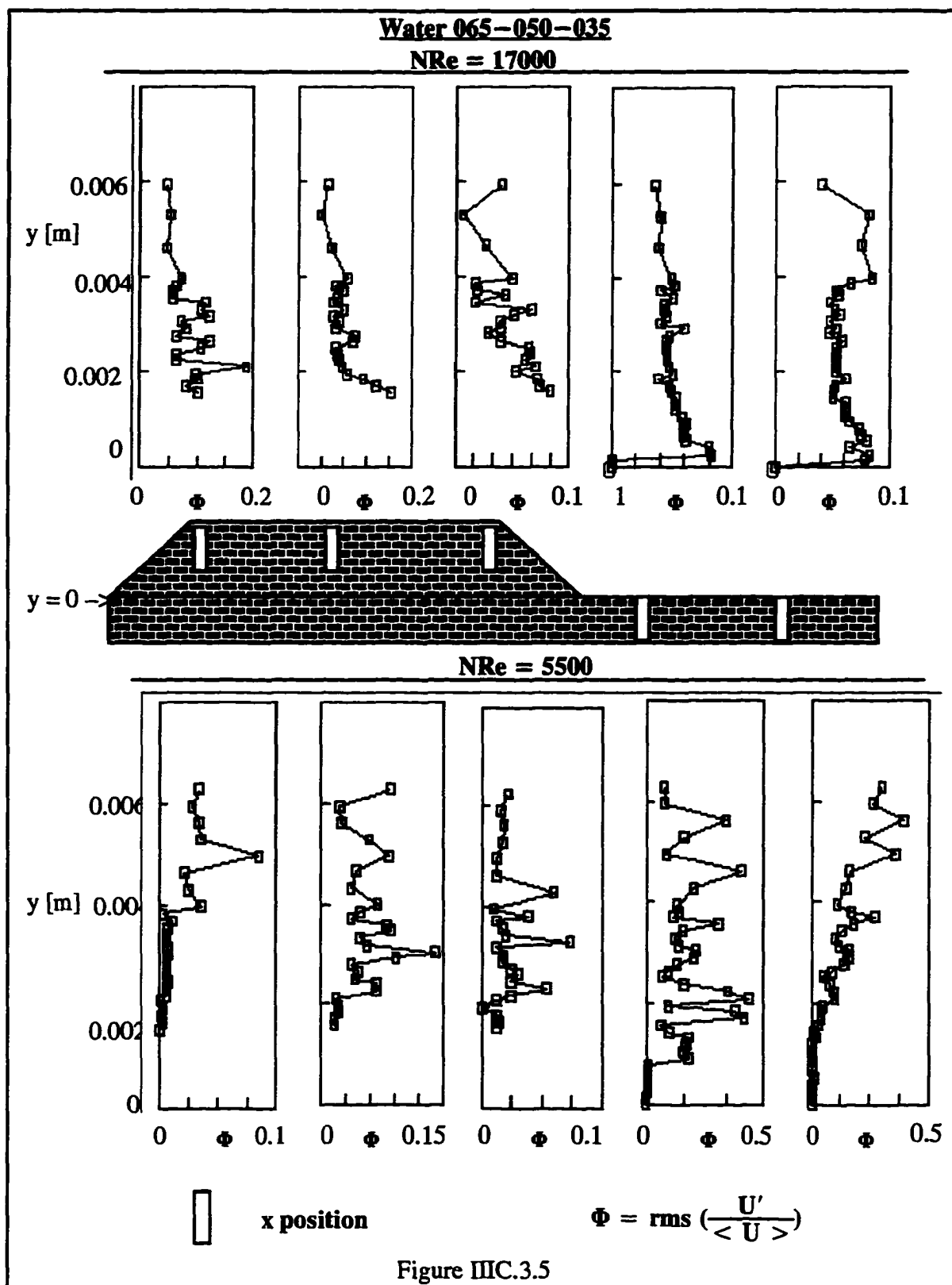
Figures III.C.3.1,2,3 show the values of turbulence intensities at two different flow rates of air on the three pipes. Figures III.C.3.4,5 are also turbulence intensities but for water flow.





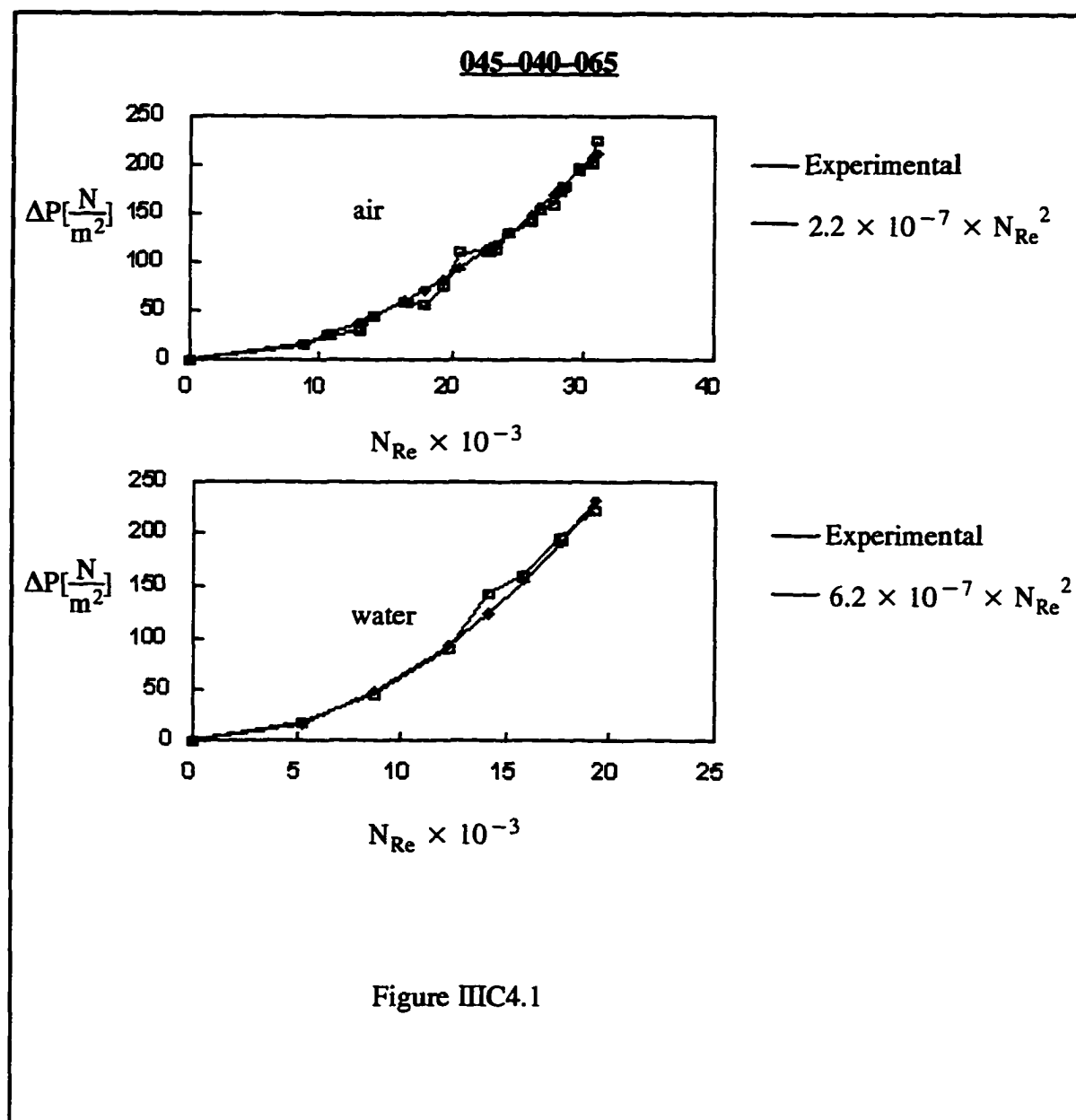


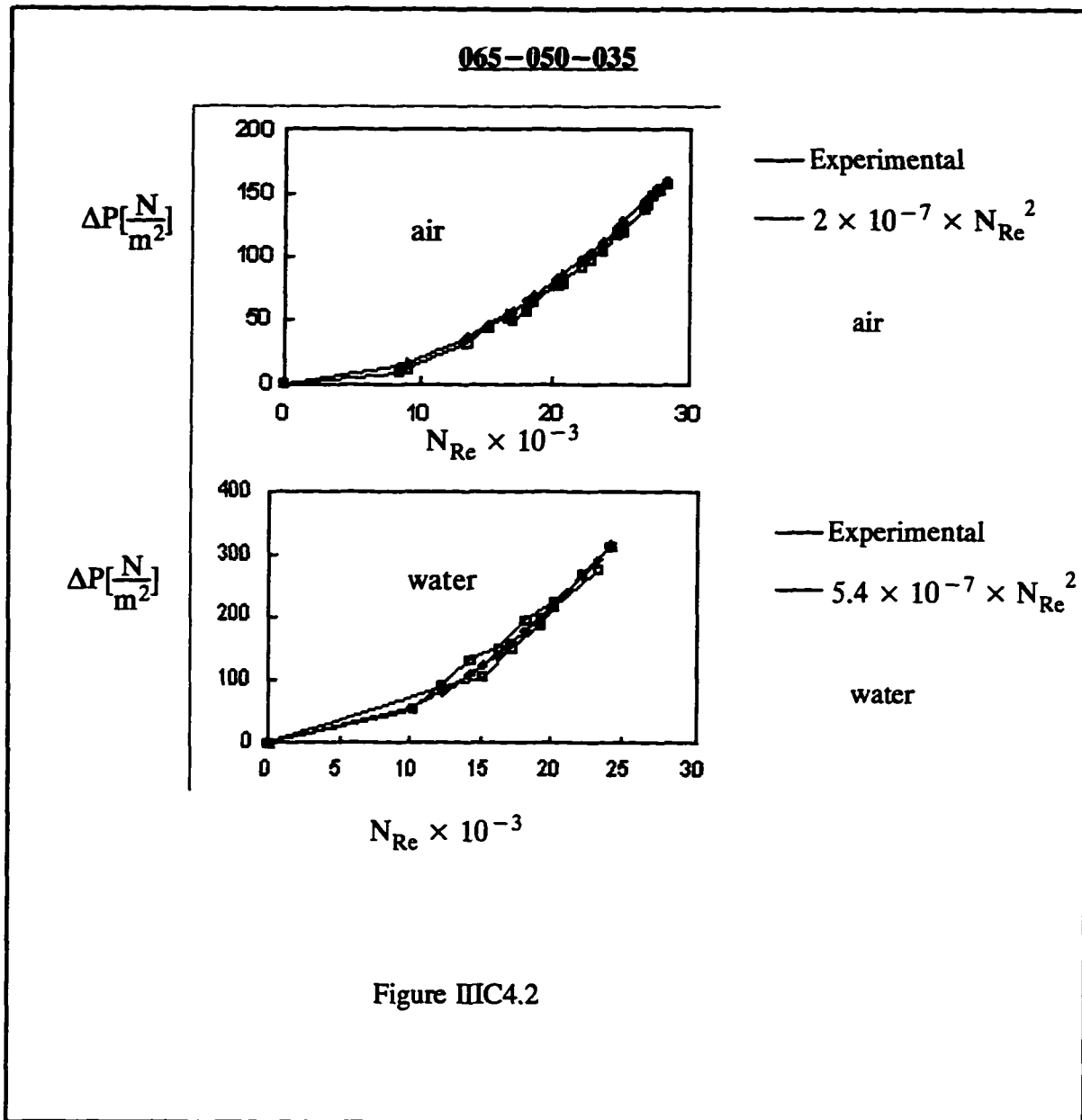




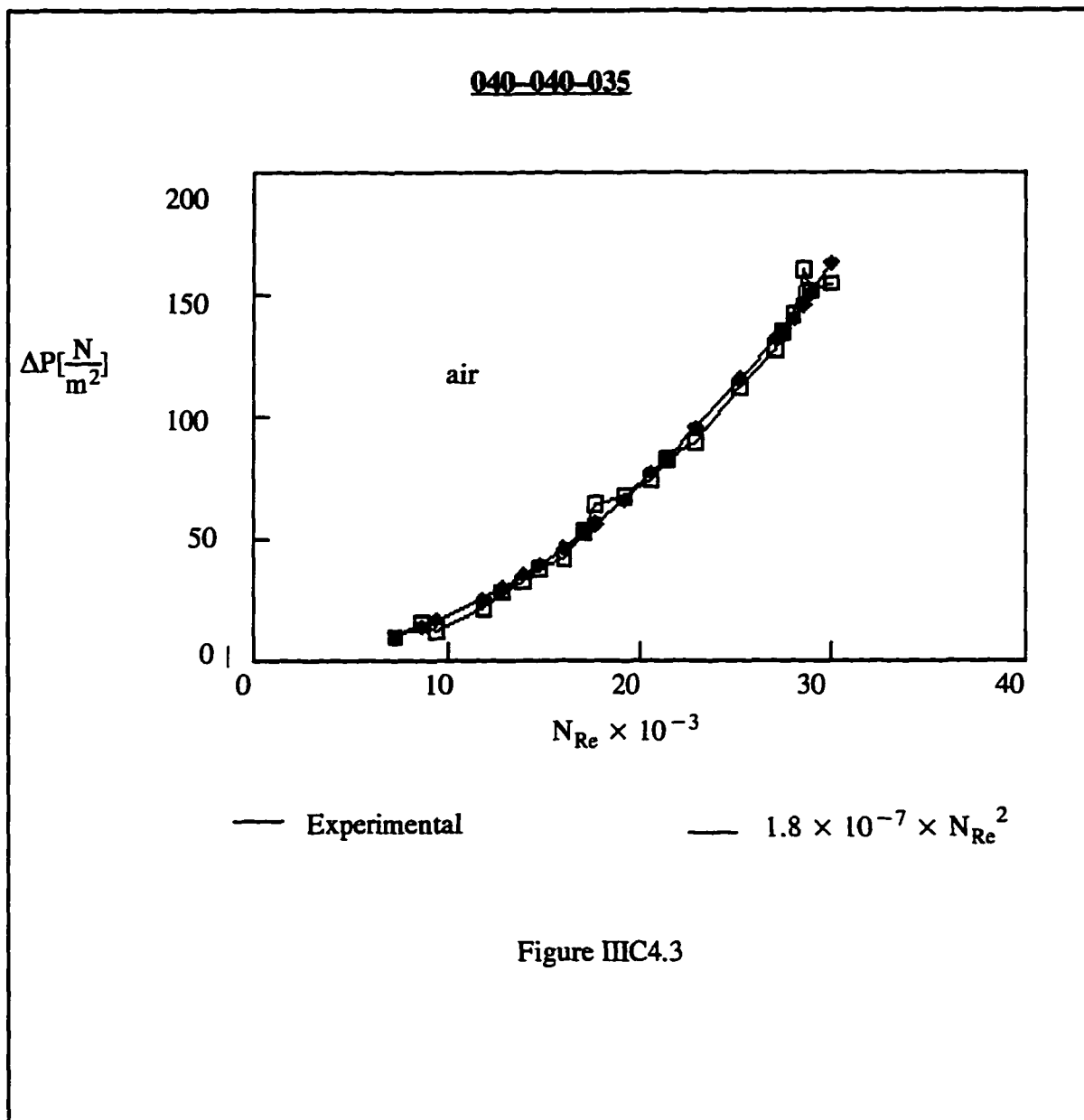
### III.C.4 Pressure drop versus Reynolds

Figure III.C.4.1,2,3 are the results of the measurements of pressure drop for different  $N_{Re}$ .









## **REFERENCES**

**Baughn, J. W., Liquid Crystals Methods for Studying Turbulent Heat Transfer, Turbulence, Heat and Mass Transfer Symposium. Lisbon, ( 1994).**

**Ferguson, J. L., Liquid Crystals, Scientific American, Vol. 210, pp. 64 – 77 ( 1964 ).**

## IV ANALYSIS OF RESULTS

The process of separation and reattachment of the boundary layer is depicted in Figure IV.1. This figure shows how the design variables might alter the flow characteristics. The first drawing shows a sequence of ribs and valleys in which the value of pitch 'P' is too small to allow for separation or reattachment. In this case there is a recirculation within the cavity and straight stream lines on top of the ribs.

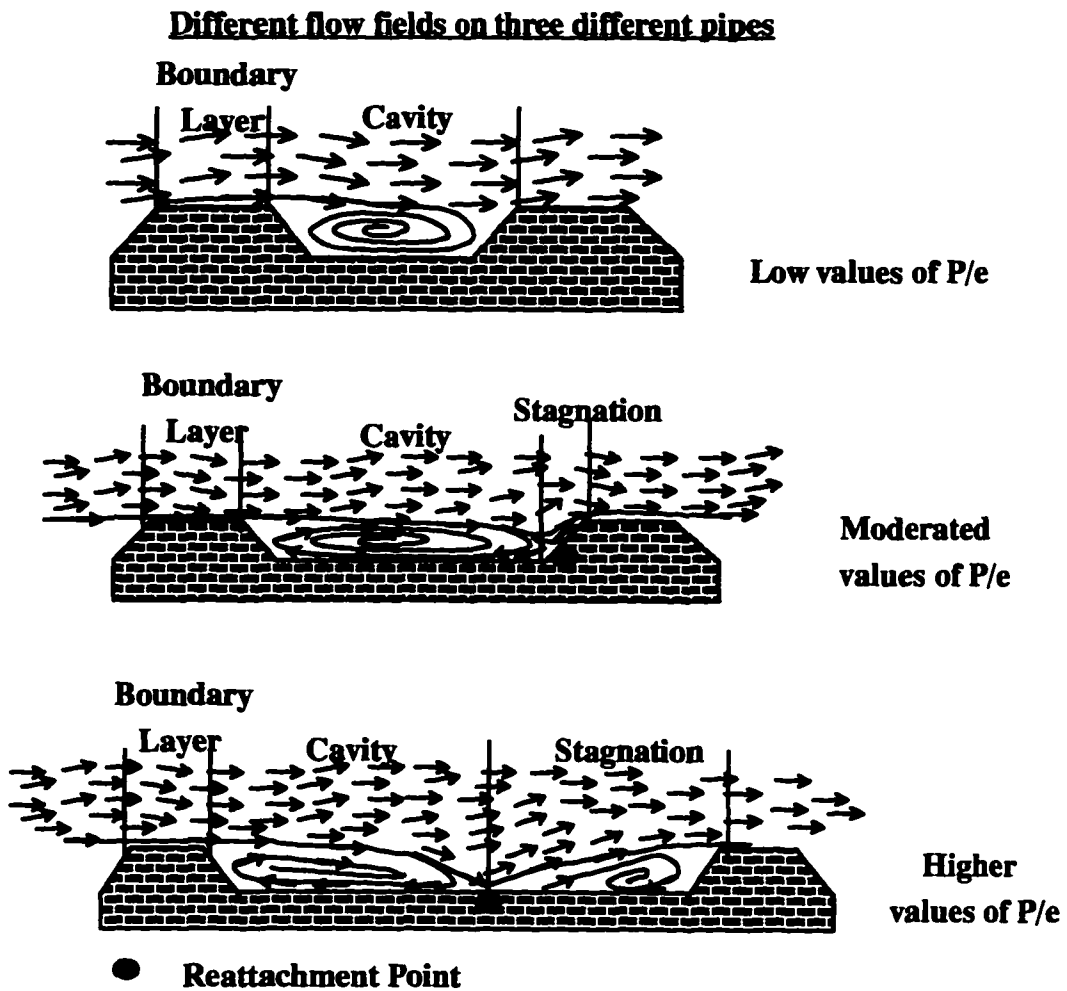
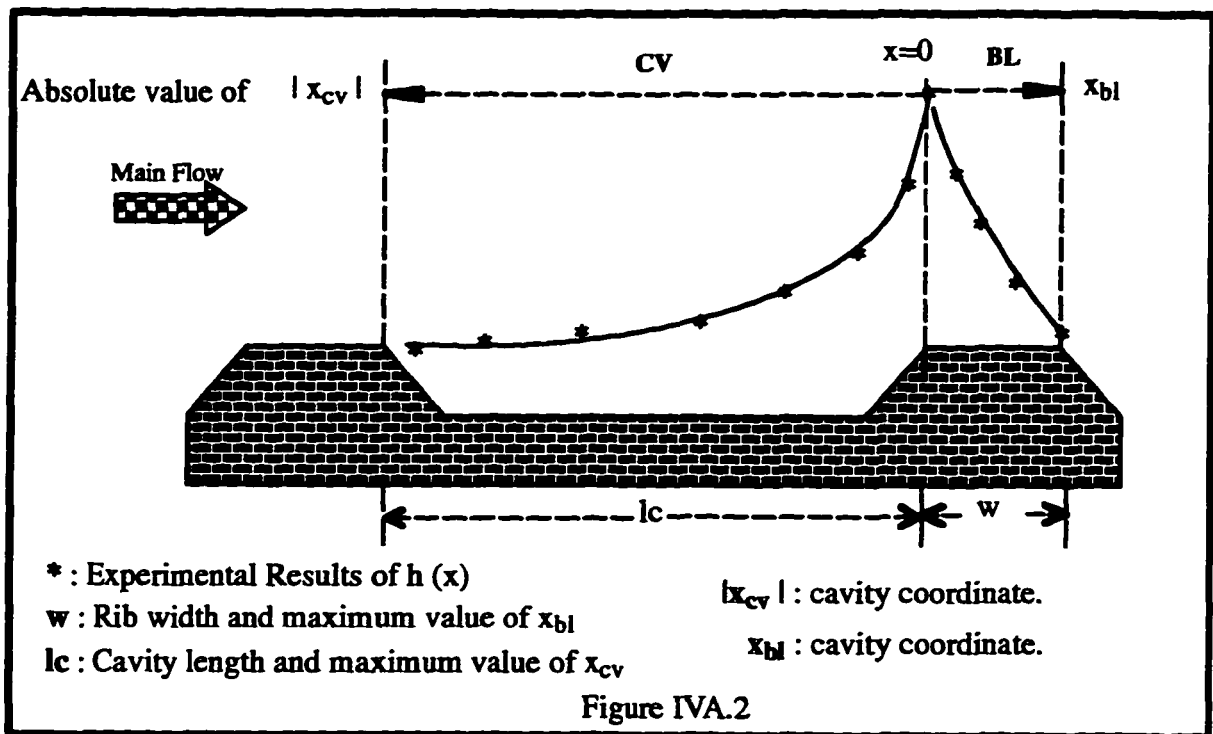


Figure IV.1

If the value of  $P$  is increased slightly, as shown in the second drawing, the boundary layer that separates at the end of the first rib reattaches on the inclined face of the second rib. After this, the boundary layer starts developing again on top of the second rib. The third and last drawing shows the case in which the value of ' $P$ ' is large enough to allow for reattachment on the valley surface. At this point, another boundary layer starts developing until it collides with the inclined face of the second rib. The aspect of the experimental results of  $h_x$  in the present work suggested that the intermediate case could be the type of flow that could describe the phenomenon on the three pipes analyzed.

The following section is divided into the analysis of heat transfer coefficients and LDV results. The overwhelming evidence of the  $h_x$  experiments (Figure IIIB2.7,8,9) suggested that the  $h_x$  profiles could be divided in two regions. The division point between these two regions was at the maximum of  $h_x$  for all three cases, which was at the leading edge of the rib. One region was the top of the rib of length ' $w$ ' (boundary layer – BL). The other region was the valley of length  $P-w$  (cavity – CV). These two regions were analyzed separately as if they were ruled by two independent mechanisms. These two mechanisms were nothing but two different flow regimes that were responsible for the shape of the  $h_x$ . Figure IVA.2 illustrates the division of the problem as well as space variables that will help to understand following sections. A good example of this line of thought could be the solution of the boundary layer equations on a flat plate under turbulent regime: The approach consisted of considering a developing laminar boundary layer that is coupled, downstream, with a turbulent boundary layer. Somehow the next sections follow the same approach. After this analysis was performed, the two independent solutions were put together to describe the global phenomenon. The results were satisfactory from the theoretical point of view and in good agreement with the experimental results.



### IVA Analysis of Local Heat Transfer Coefficients

#### IVA1 Heat Transfer on Developing Boundary Layer Region

One of the two regions in which the  $h_x$  profiles was divided, was the one on top of the rib. This region had a length of 'w' and was called boundary layer (BL) region. Equation IIC.15 of section IIC can be written as:

$$h_{(x)} = k \Theta'(\eta = 0) \left[ \frac{U_\infty}{\nu} \right]^{1/2} x_{bl}^{-1/2} \quad \text{IVA.1.1}$$

$U_\infty$  = average velocity of the main flow.

$\nu$  = kinematic viscosity of the fluid.

$x_{bl}$  = position along the boundary layer.

$k$  = thermal conductivity of the fluid.

Equation IVA1.1 can also be written as:

$$\frac{h(x)}{(\frac{U_{\infty}}{v})^{1/2}} = k \Theta'(\eta = 0)(x_{bl})^{-\frac{1}{2}} \quad \text{IVA1.2}$$

$$\ln\left(\frac{h(x)}{(\frac{U_{\infty}}{v})^{1/2}}\right) = \ln[k \Theta'(\eta = 0)] - \frac{1}{2} \ln(x_{bl}) \quad \text{IVA1.3}$$

Calling  $H_{bl}(x) = \frac{h(x)}{(\frac{U_{\infty}}{v})^{1/2}}$  and  $k \Theta'(\eta = 0) = C_{bl}$

Equation IVA1.3 yields:

$$\ln(H_{bl}(x)) = \ln(C_{bl}) - \frac{1}{2} \ln(x_{bl}) \quad \text{IVA1.4}$$

The values of  $H_{bl}(x)$  were calculated from the experimental  $h(x)$  profiles on the BL region on top of the rib ( points at the right of the maximum of  $h(x)$ . See Figure IVA.2 ) This was done for the three pipes analyzed and for all the flow rates. The origin of the BL (  $x_{bl}=0$  ) was at the position of the maximum of  $h(x)$  and the end at a distance 'w' from  $x_{bl}=0$ . The values of Hbl were plotted vs 'x<sub>bl</sub>' on a log-log graph. See Figure IVA1.1. Also on this graph, eq. IVA1.4 was plotted together with the experimental values of Hbl(x). This was possible by choosing the adequate value of Cbl (  $C_{bl,exp} = 0.0018 \text{ w/m}^2\text{K}$  ). Using  $k_{air} = 0.0262 \text{ w/mK}$  it was calculated:

$$\Theta'(\eta = 0) = \frac{C_{bl}}{k} = 0.0687$$

According to section IIC:

$$\frac{\partial T}{\partial y} \Big|_{y=0} = \frac{(T_{\infty} - T_0)}{L^{\frac{1}{2}}} \left( \frac{N_{Re}|_L}{x} \right)^{\frac{1}{2}} \frac{d\Theta}{d\eta} \Big|_{\eta=0}$$

The order of magnitude of  $\frac{\partial T}{\partial y} \Big|_{y=0}$  can be estimated using typical values of:

$$O(L) = O(w) = O(x) \approx 0.0015\text{m} \quad O(U_{\infty}) \approx 5\text{m/s}$$

$$O(T_0 - T_{\infty}) \approx 20\text{C}^{\circ} \quad O(N_{Re}|_L) \approx 500$$

$$\frac{\partial T}{\partial y} \Big|_{y=0} = \frac{20}{0.0015^{0.5}} \left( \frac{500}{0.0015} \right)^{0.5} 0.0687 = 20480 \text{ C}^{\circ}/\text{m} = 20.48 \text{ C}^{\circ}/\text{mm}$$

For this type of flow the BL thickness will be:

$$\delta_m(L) = 5 L (N_{Re}|_L)^{-\frac{1}{2}} = 5 \times 1.5\text{mm} \times (500)^{-\frac{1}{2}} = 0.33\text{mm}$$

This makes  $\Delta T$  across the boundary layer:

$$\Delta T = 20.48 \frac{\text{C}^{\circ}}{\text{mm}} \times 0.33\text{mm} = 6.7\text{C}^{\circ}$$

This temperature difference is much smaller than the average temperature difference of  $20 \text{ C}^{\circ}$ . This result is reasonable and validates again the assumption of constant air temperature.

The result of this analysis yielded the equation that described the values of  $h_{(x)}$  on top of the rib:

$$H_{bl}(x) = C_{bl} k x_{bl}^{-b} \quad \text{IVA1.5}$$

or

$$h_{(x)} = C_{bl} k \left[ \frac{U_{\infty}}{v} \right]^b x_{bl}^{-1/2} \quad \text{IVA1.6}$$

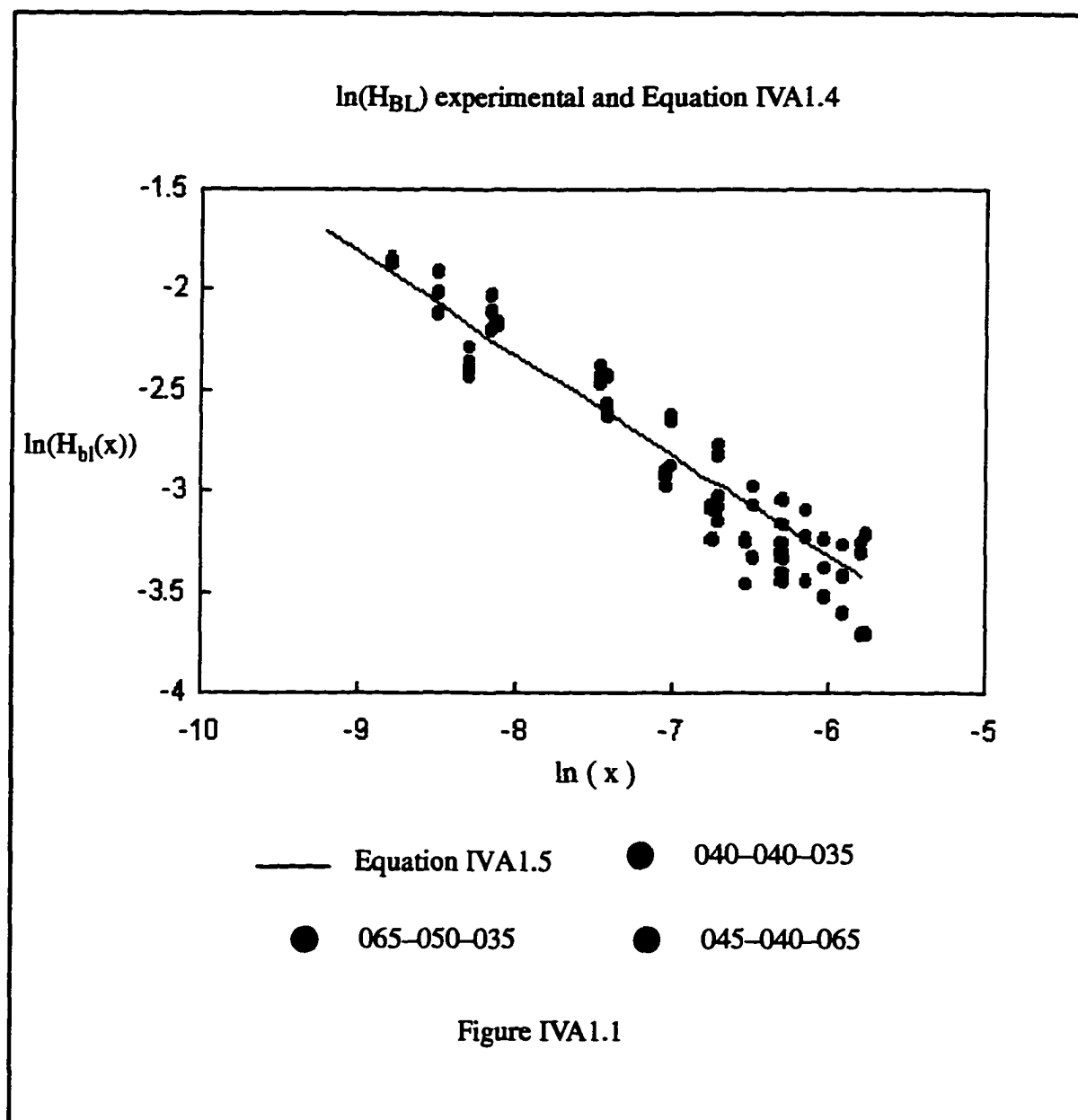
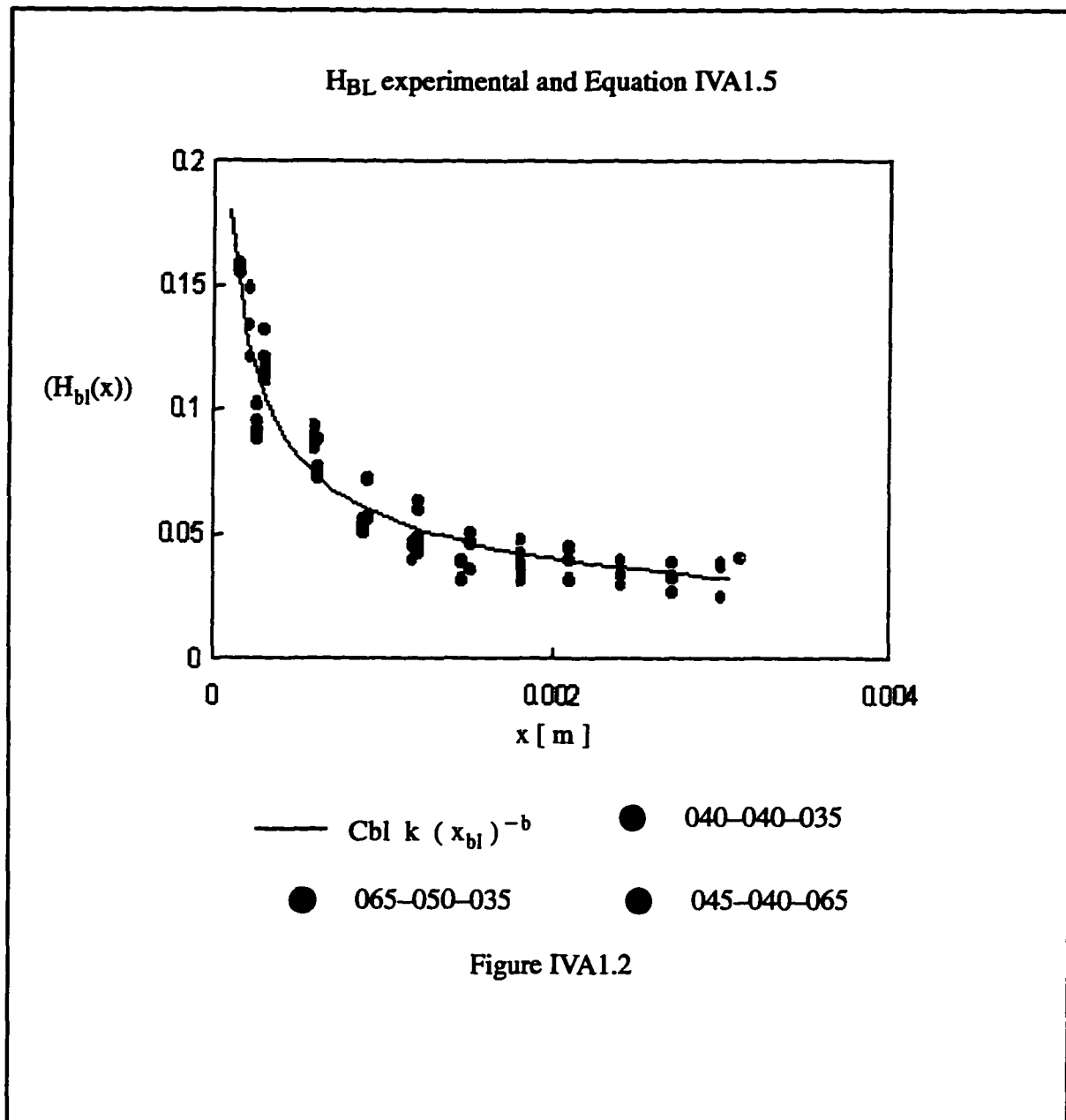


Figure IVA1.2 shows equation IVA1.5 and the experimental values of  $H_{bl}(x)$  for the BL region on a linear plot.





Equation IVA1.6 was integrated along 'w' ( top of the rib) to obtain the average value of the BL heat transfer coefficient:

$$\langle h \rangle_{bl} = \frac{1}{w} \int_0^w h_{(x)} dx = Cbl \frac{k}{w} \left[ \frac{U_\infty}{v} \right]^{1/2} \int_0^w x_{bl}^{-b} dx$$

Defining:  $(N_{Re}|_w) = \frac{w U_\infty}{v}$  and  $N_{Nu}|_w = \frac{\langle h \rangle_{bl} w}{k}$

$$\langle h \rangle_{bl} = a \frac{k}{w} (N_{Re}|_w)^{b'}$$
IVA1.7

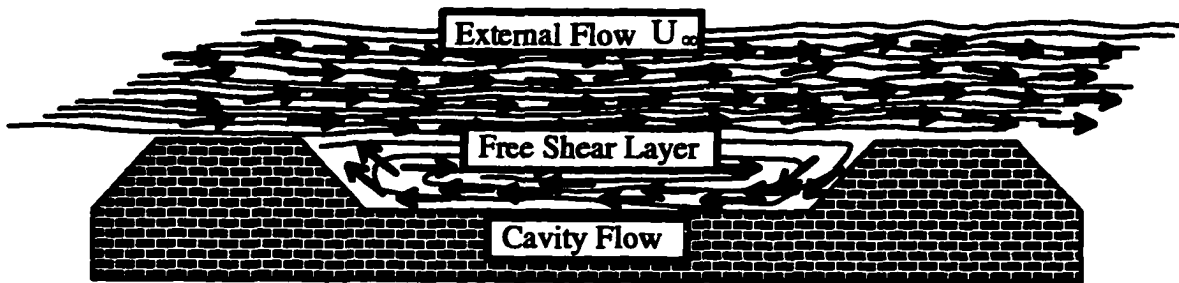
$$N_{Nu}|_w = a (N_{Re}|_w)^{b'}$$
IVA1.8

Equation IVA1.6 is the corollary of the heat transfer analysis in the BL region. This equation was of extreme importance for the elaboration of an expression of the overall heat transfer coefficient.

#### IVA2 Heat Transfer on Cavity Surface

The valley region between the ribs was called cavity (CV). This region is characterized by the existence of a free shear layer. When the flow detaches at the second edge of the rib, a free shear layer is produced that separates the main flow from the low velocity region between the ribs. Evidence of this phenomenon is shown in Figures IIIC.3,1,2,3 where turbulence intensities are depicted. On these figures it is clear that an increase in turbulence intensity is produced at a distance of a rib height from the pipe wall within the valley. This increase in turbulence is caused by the free shear layer. The free shear layer is the boundary between the main flow and the cavity flow. In fact, this is coincident with the work performed by Seban on shallow rectangular cavities. Seban proposes a solution for  $h_{(x)}$  in the cavity similar to that one of Colburn of turbulent flow on an isothermal plate. This author also reports that the maximum of heat transfer occurs at the leading edge of the rib. The results shown on Figures IIIB2.7,8,9

of the present work agree with those of Seban. These results show clearly that the maximum value of  $h_{(x)}$  is found, in fact, at the leading edge of the ribs in the three pipes that were studied. The following figure is an schematic of the cavity showing the free shear layer and the main stream.



Seban proposes a solution for the local heat transfer coefficient within the cavity of the form:

$$h_{(x)} = C_{cv} \left( \frac{U_\infty}{\nu} \right)^{\frac{4}{3}} x_{cv}^{-\frac{1}{3}} \quad \text{IVA2.1}$$

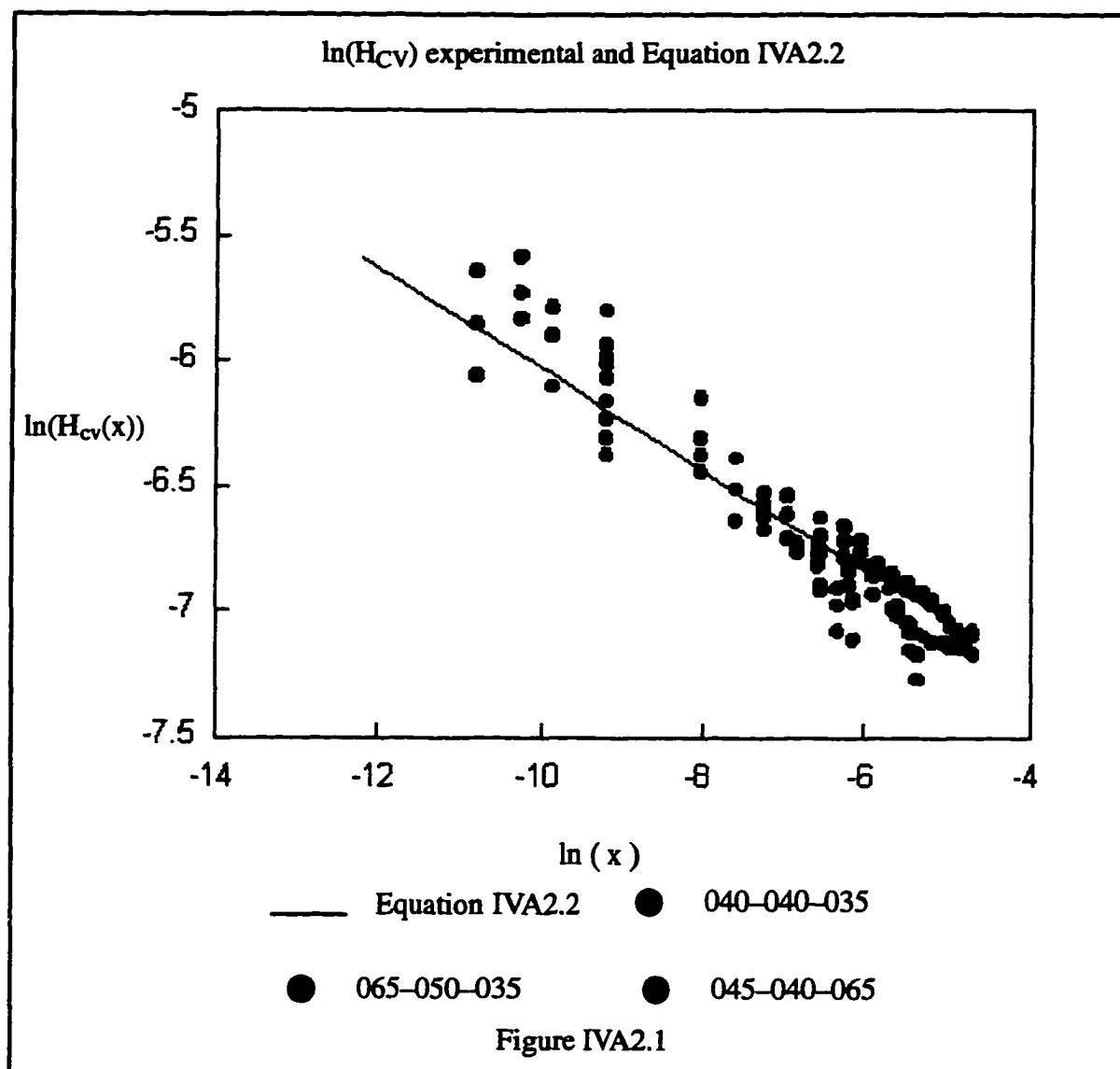
$C_{cv}$  is an experimental constant and according to Seban:  $C_{cv} = 0.034$ . In the present work, ' $x_{cv}$ ' was measured from the rib edge where the maximum  $h_{(x)}$  occurs at the edge downstream. In other words, from the right to the left on the cavity according to Figure IVA1 taking the absolute value of  $x$ . The analysis of the results of  $h_{(x)}$  in the cavity was performed in the same manner as the BL analysis. Equation IVA2.1 can be written as:

$$\ln\left(\frac{h(x)}{\left(\frac{U_m}{v}\right)^{4/5}}\right) = \ln(C_{cv}) - \frac{1}{5}\ln(x_{bl}) \quad \text{IVA2.2}$$

Calling  $H_{cv}(x) = \frac{h(x)}{\left(\frac{U_m}{v}\right)^{4/5}}$  then :

$$\ln(H_{cv}(x)) = \ln(C_{cv}) - \frac{1}{5}\ln(x_{bl}) \quad \text{IVA2.3}$$

The values of  $H_{cv}(x)$  were calculated from the experimental  $h(x)$  profiles on the CV region within the valley ( absolute value of 'x' at the left of the maximum of  $h(x)$  . See Figure IVA1). The values of  $H_{cv}$  were plotted vs 'x<sub>cv</sub>' on a log–log graph. See Figure IVA2.1.



Also on this graph, eq. IVA2.3 was plotted together with the experimental values of  $H_{cv}(x)$  and an experimental value of  $C_{cv}$ . Similar to section IVA1 and using  $k_{air} = 0.0262 \text{ w/mk}$  eq. IVA2.1 can be written as:

$$h_{(x)} = A k \left( \frac{U_{\infty}}{v} \right)^4 x_{cv}^{-B} \quad \text{IVA2.4}$$

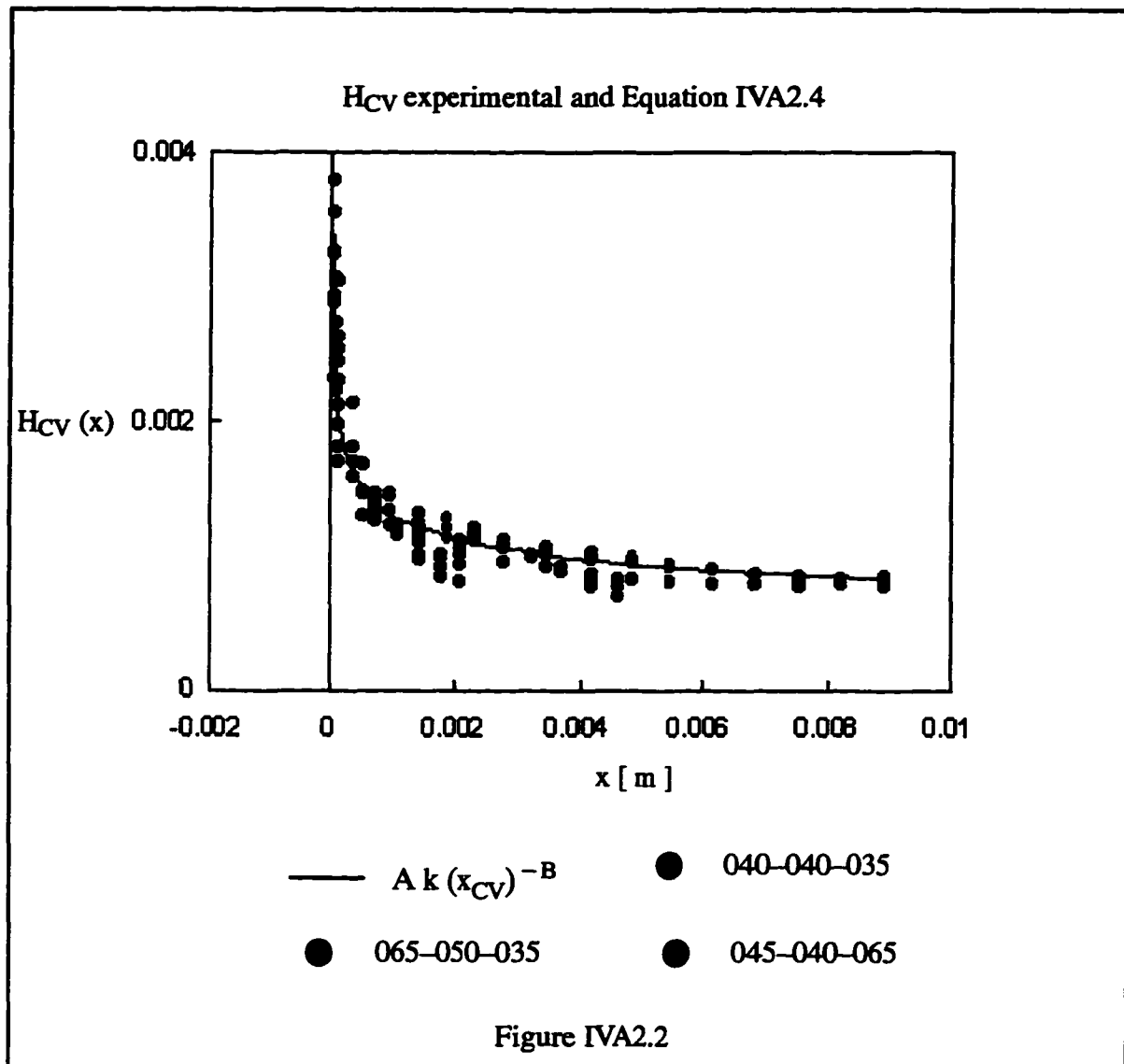
To calculate the average heat transfer coefficient in the cavity, eq. IVA2.4 was integrated along the cavity :

$$\langle h \rangle_{cv} = \frac{1}{l_c} \int_0^{l_c} h(x) dx = A \frac{k}{l_c} \left[ \frac{U_\infty}{v} \right]^{4/5} \int_0^{l_c} x_{cv}^{-B} dx$$

$$\langle h \rangle_{cv} = A \frac{k}{l_c} (N_{Re'l_c})^{B'} \quad \text{IVA2.5}$$

$$N_{Nu'l_c} = A (N_{Re'l_c})^{B'} \quad \text{IVA2.6}$$

As well as eq. IVA1.7 in section IVA1, eq. IVA2.5 was the second component of the expression for the overall heat transfer coefficient of a repeating unit. Figure IVA2.2 shows equation IVA2.4 and the experimental values of  $H_{cv}(x)$  for the CV region on a linear plot, showing the good description of the phenomenon by eq. IVA2.4.

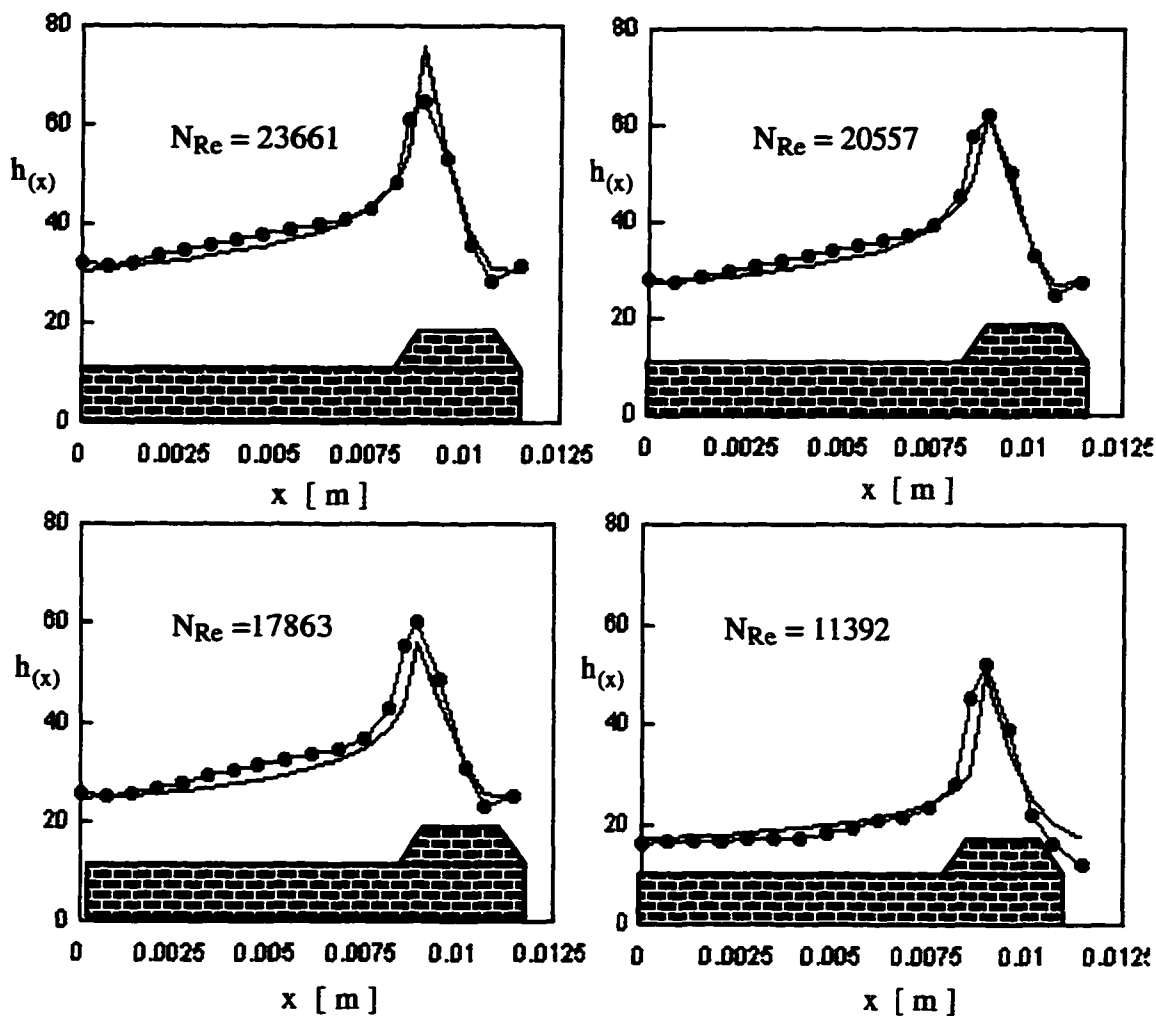


### IVA3 Average Heat Transfer Coefficient AHTC $\langle\langle h \rangle\rangle$

In this section the concepts of cavity flow and developing boundary layer were put together to define the AHTC. Prior to this, eq IVA1.6 and IVA2.4 were plotted together with the experimental results of  $h(x)$  and shown on Figures IVA2.3,4,5. These plots correspond to  $h(x)$  experimental profiles for a complete repeating unit in all the experiments carried out.

Local Heat Transfer Coefficients and BL, CV Correlations

040-040-035



● Experimental Results

$h_{(x)}$  [  $\frac{\text{watts}}{\text{m}^2\text{K}}$  ]

{  $h_{(x)} = A k (\frac{U_{\infty}}{\nu})^{\frac{1}{2}} x_{cv}^{-B}$

Cavity  $|x| < l_c$

$h_{(x)} = Cbl k [\frac{U_{\infty}}{\nu}]^{\frac{1}{2}} x_{bl}^{-b}$

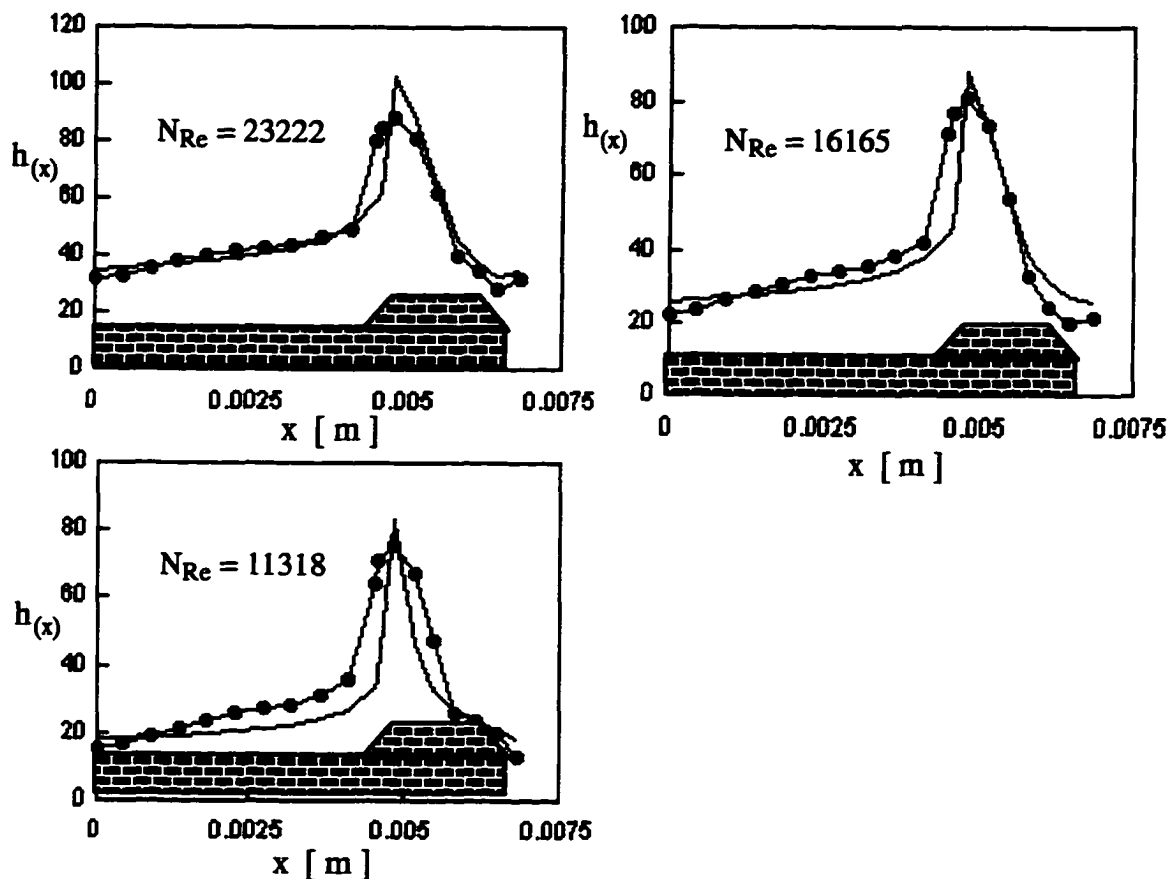
Boundary Layer  $x > l_c$

Figure IVA2.3



Local Heat Transfer Coefficients and BL, CV Correlations

045-040-065



● Experimental Results  $h_{(x)} \left[ \frac{\text{watts}}{\text{m}^2\text{K}} \right]$

$$\left\{ \begin{array}{l} h_{(x)} = A k \left( \frac{U_{\infty}}{\nu} \right)^{\frac{4}{5}} x_{cv}^{-B} \quad \text{Cavity } |x| < l_c \\ h_{(x)} = C b l k \left[ \frac{U_{\infty}}{\nu} \right]^{\frac{1}{2}} x_{bl}^{-b} \quad \text{Boundary Layer } x > l_c \end{array} \right.$$

Figure IVA2.4

Local Heat Transfer Coefficients and BL, CV Correlations

045-040-065

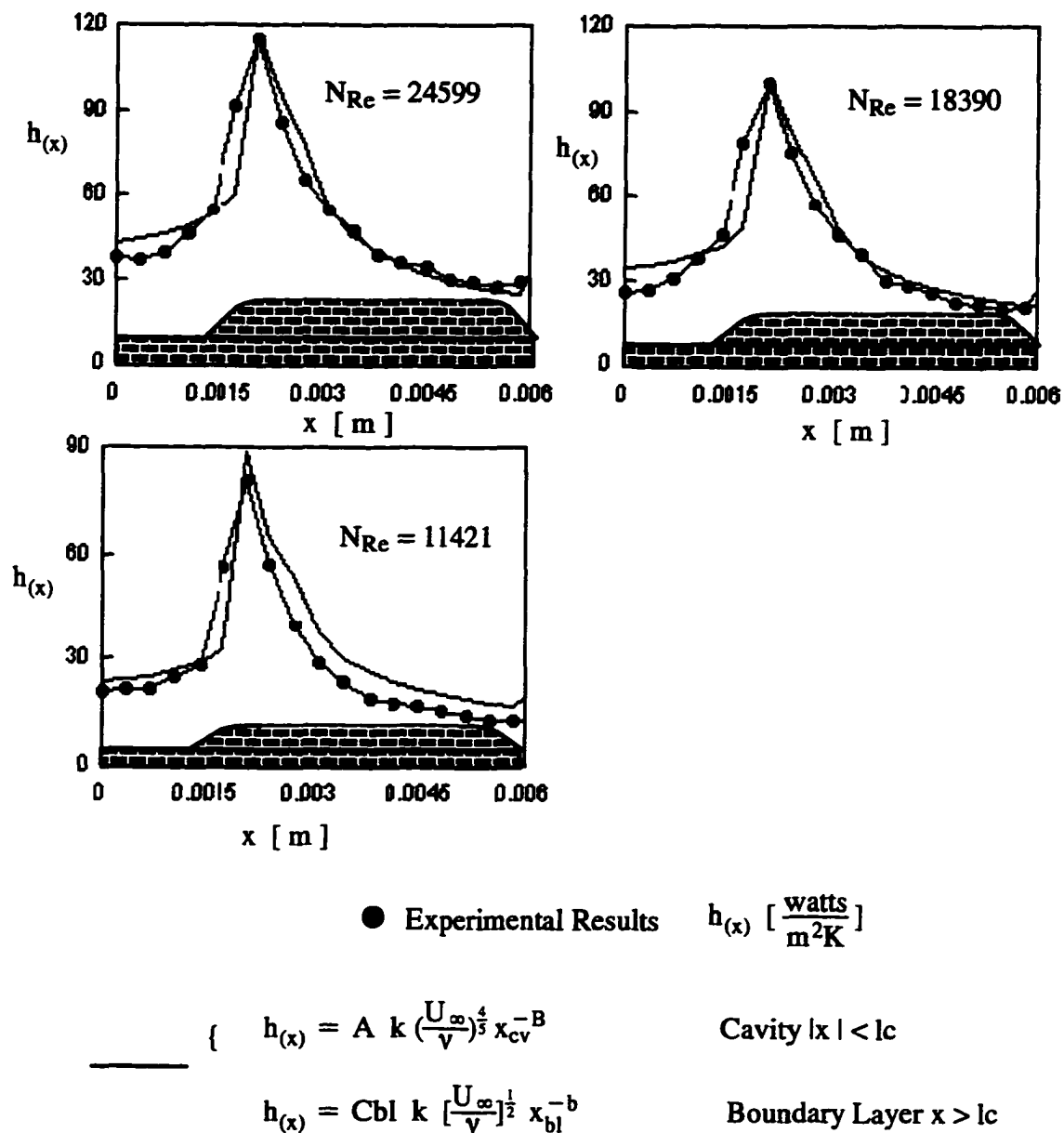


Figure IVA2.5

As it is clear from the characteristics of eq. IVA1.6 and IVA2.4, they had a singularity at the point  $x=0$ . Theoretically at this point, the values of  $h(x)$  should go to infinity. The plots shown on Figures IVA2.3,4,5. were done assigning a small but finite value to 'x' in the neighborhood of  $x=0$ . Depending on which value was chosen, the two equations will meet or not at the experimental value of  $h(x)$ . In fact, the values of 'x' that were chosen were those that made the two expressions coincide at the maximum experimental value of  $h(x)$ . The purpose of the calculation of the AHTC was : first, to verify that the two approaches of eq IVA1.7 and IVA2.5 could be put together in a general correlation to describe a global phenomenon, and , to compare the values predicted by the overall correlation with those overall measurements done by the manufacturers of the pipes and the computations of the present work.

The first step in joining eq IVA1.7 and IVA2.5 was to define the AHTC:

$$\langle\langle h \rangle\rangle = \frac{\langle h \rangle_{cv} l_s + \langle h \rangle_{bl} w}{l_o} \quad \text{IVA3.1}$$

where:

w : Rib Width

$l_o = P-2b+2h$  Total upper surface area of the repeating unit.

$l_s = P-w-2b+2h$  Surface area contained within the cavity.

Notice that the contribution of  $\langle h \rangle_{cv}$  to the average was through 'ls' and not 'lc'. The value 'ls' is the surface contained within the cavity through which  $\langle h \rangle_{cv}$  performs. Equations IVA1.7 and IVA2.5 were applied to the definition of the AHTC in eq. IVA3.1 as follows:

$$\ll h \gg = \frac{A \frac{k}{lc} (N_{Re|lc})^{\frac{4}{5}} ls + a \frac{k}{w} (N_{Re|w})^{\frac{1}{2}} w}{lo} \quad \text{IVA3.2}$$

$$N_{Nu|l_s} = A \frac{1}{lc} (N_{Re|lc})^{\frac{4}{5}} ls + a \frac{1}{w} (N_{Re|w})^{\frac{1}{2}} w \quad \text{IVA3.2'}$$

The definition of AHTC of the present work was different from the one of the manufacturers. Because of this and prior to comparing results, a final refinement was necessary on eq. IVA3.2. It is more convenient from a design standpoint, and this practice is followed by the manufacturers to define an AHTC based on the smooth pipe. In the case of the present work the AHTC is referred to 'lo' that is the total area on top of a repeating unit. Defining the AHTC with respect to the smooth pipe is equivalent to defining it per unit pitch (P). What both definitions have in common is the fact that when applied, they have to yield the same value of heat flux through the pipe wall. This is:

$$q = \ll h \gg_{\text{man}} P \Delta T_{\text{man}} = \ll h \gg_{\text{IVA3.2}} lo \Delta T_{\text{crystals}} \quad \text{IVA3.3}$$

$$\Delta T_{\text{man}} = (T_{\text{wall}} - T_{\text{air}})$$

$$\Delta T_{\text{crystals}} = (\langle T_{\text{crystals}} \rangle - T_{\text{air}})$$

The sub index 'man' stands for : manufacturers. The use of  $\langle T_{\text{crystals}} \rangle$  in IVA3.3 as it is was possible because of the small differences in temperature on top of a repeating unit. Although helpful to find the distribution of  $h(x)$ , the  $T_c$  profiles were almost constant from the point of view of a  $\Delta T_{\text{air}}$ . With this precaution, the following analysis was done:

$$\Delta T_{\text{man}} = \Delta T_{\text{crystals}} \quad \text{therefore:}$$

$$\ll h \gg_{\text{man}} = \ll h \gg_{\text{IVA3.2}} \frac{lo}{P} \quad \text{that applied to IVA3.2 gives :}$$

$$\ll h \gg_{\text{man}} = \frac{A \frac{k}{lc} (N_{Re|lc})^{\frac{4}{5}} ls + a \frac{k}{w} (N_{Re|w})^{\frac{1}{2}} w}{P} \quad \text{IVA3.4}$$

Finally eq. IVA3.4 was able to predict the AHTC of any pipe design provided the geometrical parameters were known. The agreement with the manufacturers calculations was satisfactory and the discrepancies never exceeded 15% in the values of  $\langle\langle h \rangle\rangle$ . Figures IVA2.6 and 7 show both eq. IVA3.4 and the experimental measurements of AHTC performed by the manufacturers for two different  $N_{Re}$ .

### Heat Transfer Augmentation on Different Models

$$\underline{N_{Re} = 25000}$$

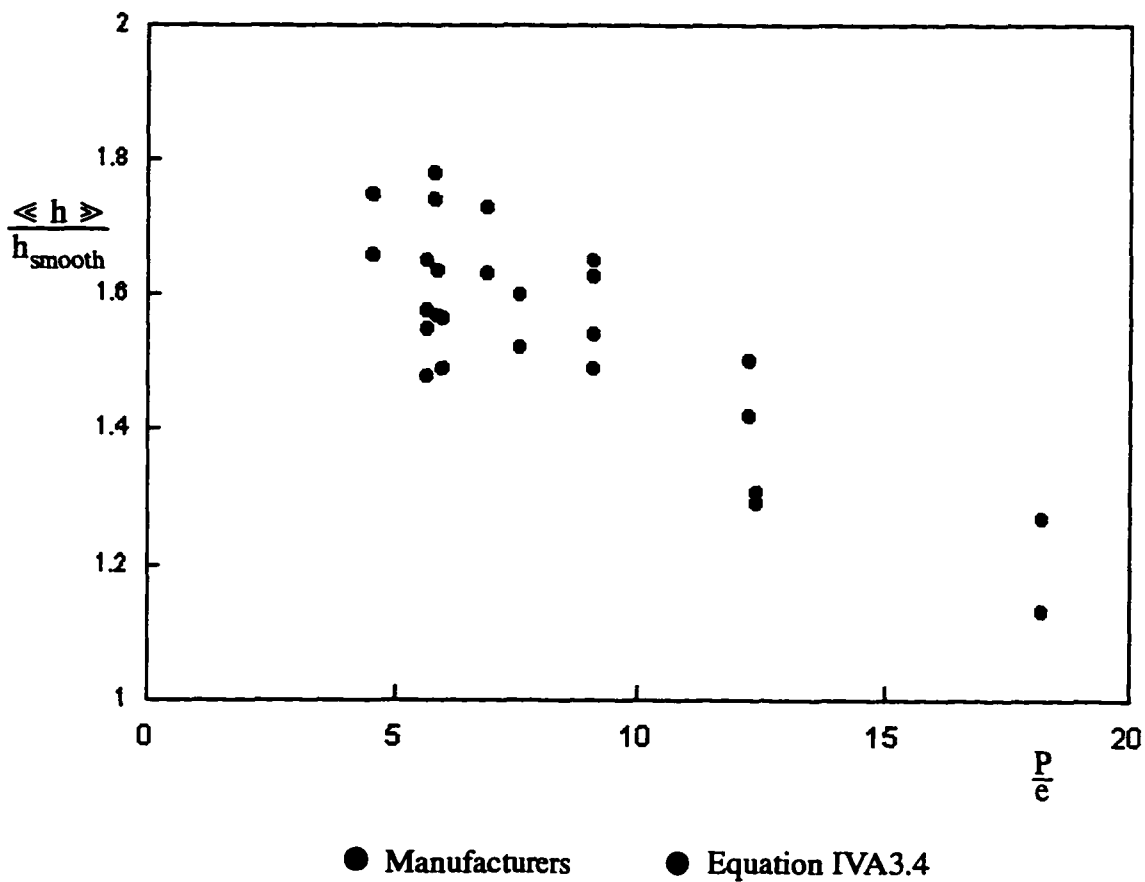


Figure IVA2.6

Heat Transfer Augmentation on Different Models

$N_{Re} = 35000$

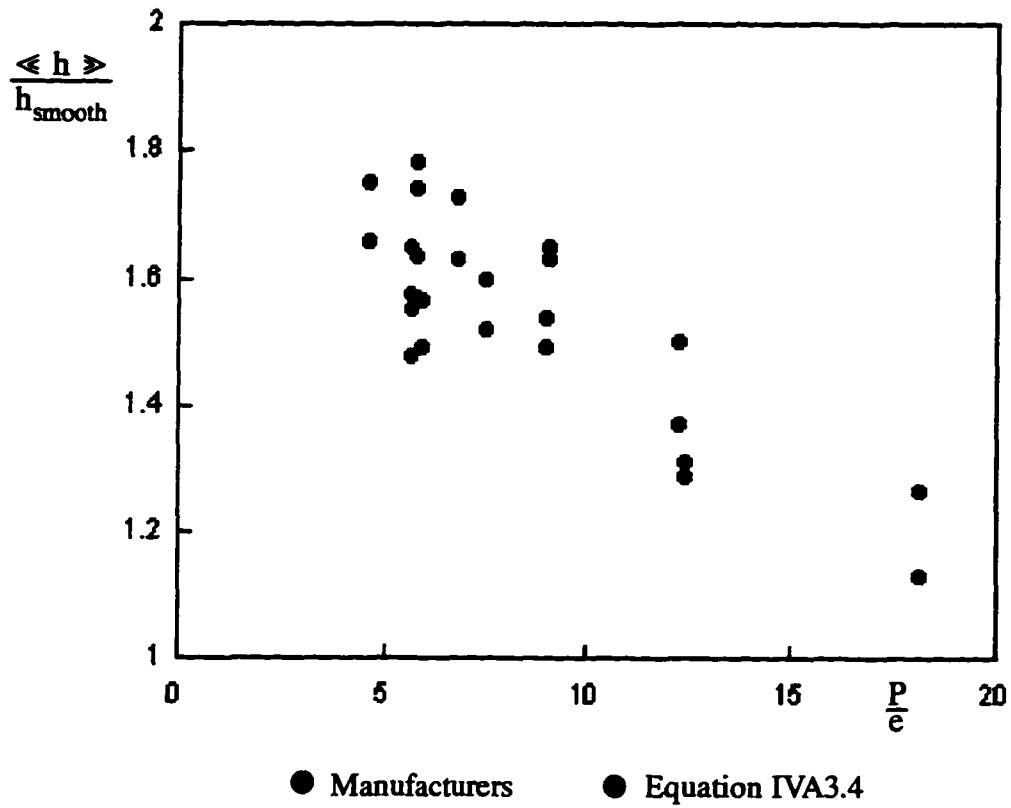


Figure IVA2.7

### IVB Analysis on Friction Factors

Heat transfer enhancement with turbulence promoters also results in an increase of the pipe friction factor. If performance is what is wanted from a certain pipe design, the AHTC has to be maximized without increasing the friction factor of the pipe to impractical levels.

The analysis of friction factors followed a scheme similar to the analysis of local heat transfer coefficients. The values of friction factor 'f' were analyzed for the two separated regions (BL and CV). After this analysis was performed the two solutions were put together to construct an expression for the average friction factor ( $\langle f \rangle$ ).

#### IVB.1 Friction Factors from LDV Velocity Profiles

The friction factors along the repeating units were calculated from the results of the LDV velocity profiles and the concepts elaborated in section IIC and IID. For the evaluation of 'f' the value of  $U^*$  was needed:

from section IIC:

$$f_{(x)} = \frac{\tau_{xy}}{\frac{U_{\infty}^2}{2}}$$

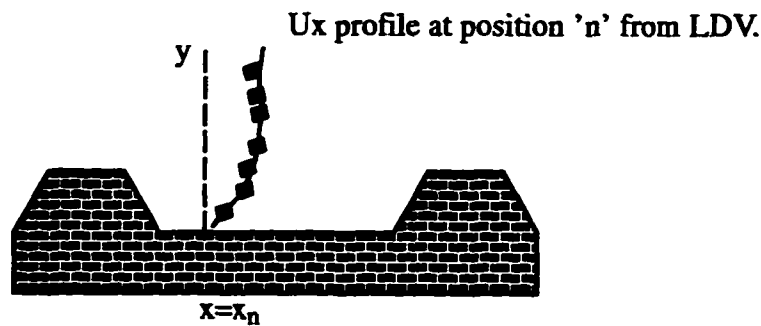
from section IID:

$$U^* = \left(\frac{\tau_w}{\rho}\right)^{\frac{1}{2}} \quad \text{frictional velocity and}$$

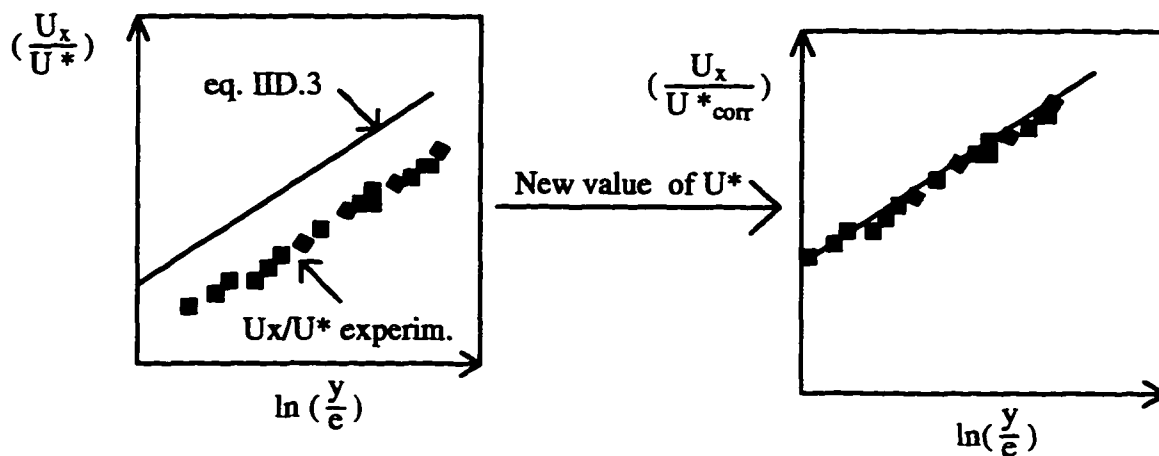
$$f_{(x)} = 2 \left(\frac{U^*}{U_{\infty}}\right)^2 \quad \text{IVB.1}$$

To apply equation IV it was necessary first to calculate the value of  $U^*$  of each velocity profile along the repeating unit. This was done using eq. IID.3. The procedure consisted of a sequence of iterations. A value of  $U^*$  was guessed from the values of  $\Delta P$ . With this value of  $U^*$  the corresponding  $\epsilon^*$  (section IID) was calculated. With this  $\epsilon^*$  the value of 'B' in eq. IID.3 was extracted from the Figure IID.1. The values of  $U_x$  from the LDV measurements were plotted

as  $U_x / U^*$  vs.  $\ln(y/e)$  using the guessed value of  $U^*$ . On the same graph eq.IID.3 was plotted with the value of 'B' extracted from Figure IID.1. The equation and the experimental data were compared and if they were not on the same line, a new value of  $U^*$  was guessed repeating the iteration until equation and data were coincident on the same line. Figure IVB1 shows a scheme of the procedure that might clarify the steps of the iteration process.



- 1) Assume  $U^*$  and calculate  $e^*$
- 2) Get the value of 'B' from Figure IID.1
- 3) Plot  $U_x/U^*$  and eq. IID.3



- 4) Calculate 'f' from  $U^*$ corr and eq.IVB.1

Figure IVB1



In this manner the values of  $f$ , were calculated for the three pipes. These results were compared with eq. IIC.8 for the developing BL an Seban's correlation for friction factor in the cavity section. Seban takes the results of Abramovich of flow down stream of a step and applies them to the shallow rectangular cavity. It is not the purpose of this work to analyze in detail Avramovich's solution. The expression used by Seban for the local friction factor in the cavity was:

$$f_{(x)} = 0.0332 (N_{Re}|_x)^{-\frac{1}{5}} \quad \text{IVB2.1}$$

That integrated along the cavity length yields:

$$\langle f \rangle_{cv} = \frac{1}{lc} \int_0^{lc} f_{(x)} = \frac{0.0332}{lc} \left(\frac{U_\infty}{v}\right)^{-\frac{1}{5}} \int_0^{lc} x^{-\frac{1}{5}} dx$$

$$\langle f \rangle_{cv} = 0.0415 (N_{Re}|_{lc})^{-\frac{1}{5}} \quad \text{IVB2.2}$$

Figures IVB1.1 to 5 show the plots eq.IIC.8 and eq.IVB2.1. together with the values of  $f$ , calculated from the LDV velocity profiles and  $U^*$  correction. The same distinction that was made in the calculations of  $h(x)$  was made with  $X_{BL}$  and  $X_{CV}$ . Within the cavity,  $X_{cv}$ , sweeps from the point of maximum heat transfer to the left in Figure IVA.1. To plot  $X_{cv}$ , the absolute value of this variable is taken on the left of  $x=0$  in Figure IVA.1. The boundary layer coordinate moved from the same zero as the cavity but to the right. Figures IVB1.1 to 5 show these results for water and air flow in the three models analyzed.

**Water 065-050-035**

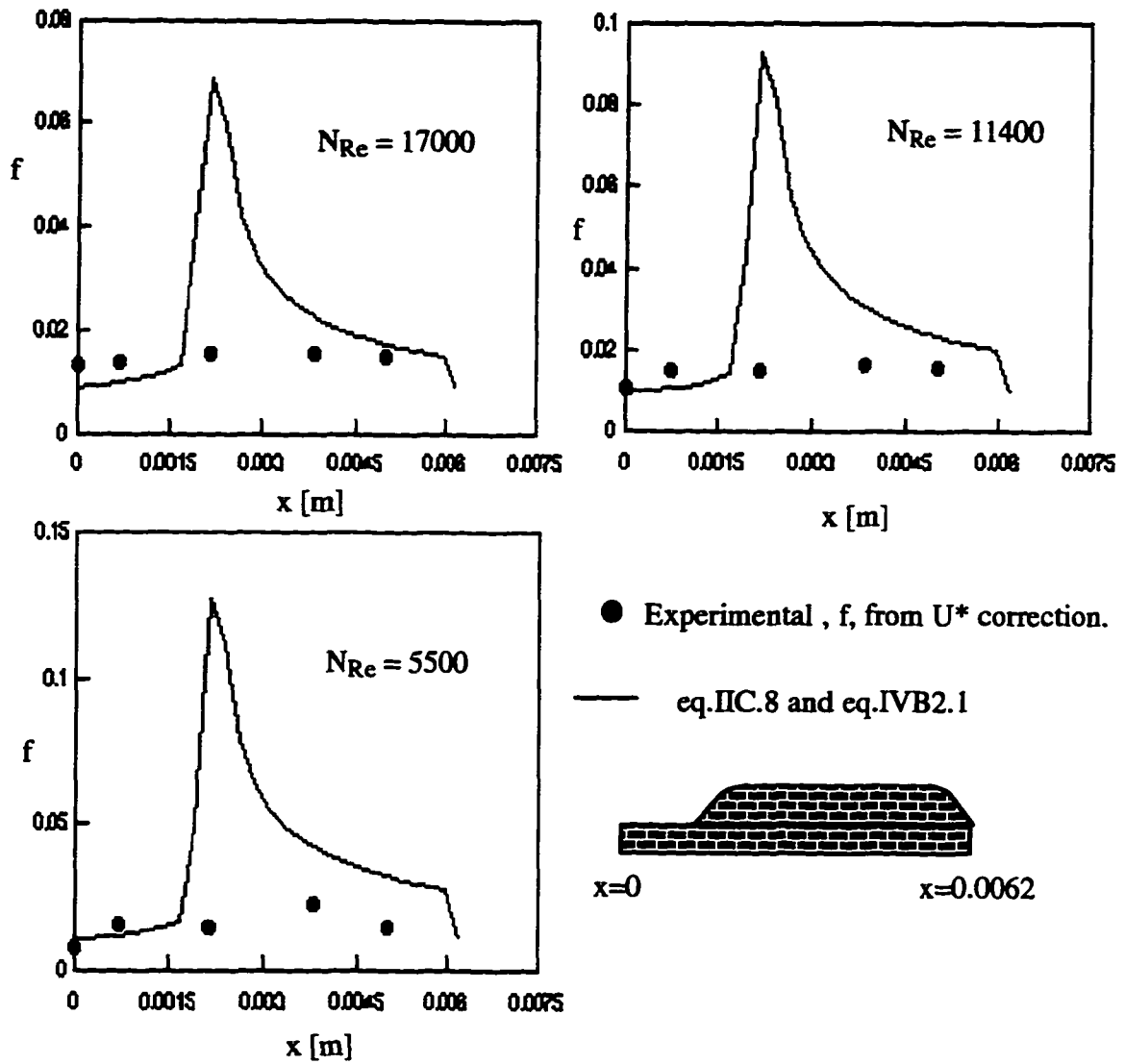


Figure IVB1.1

Water 045-040-065

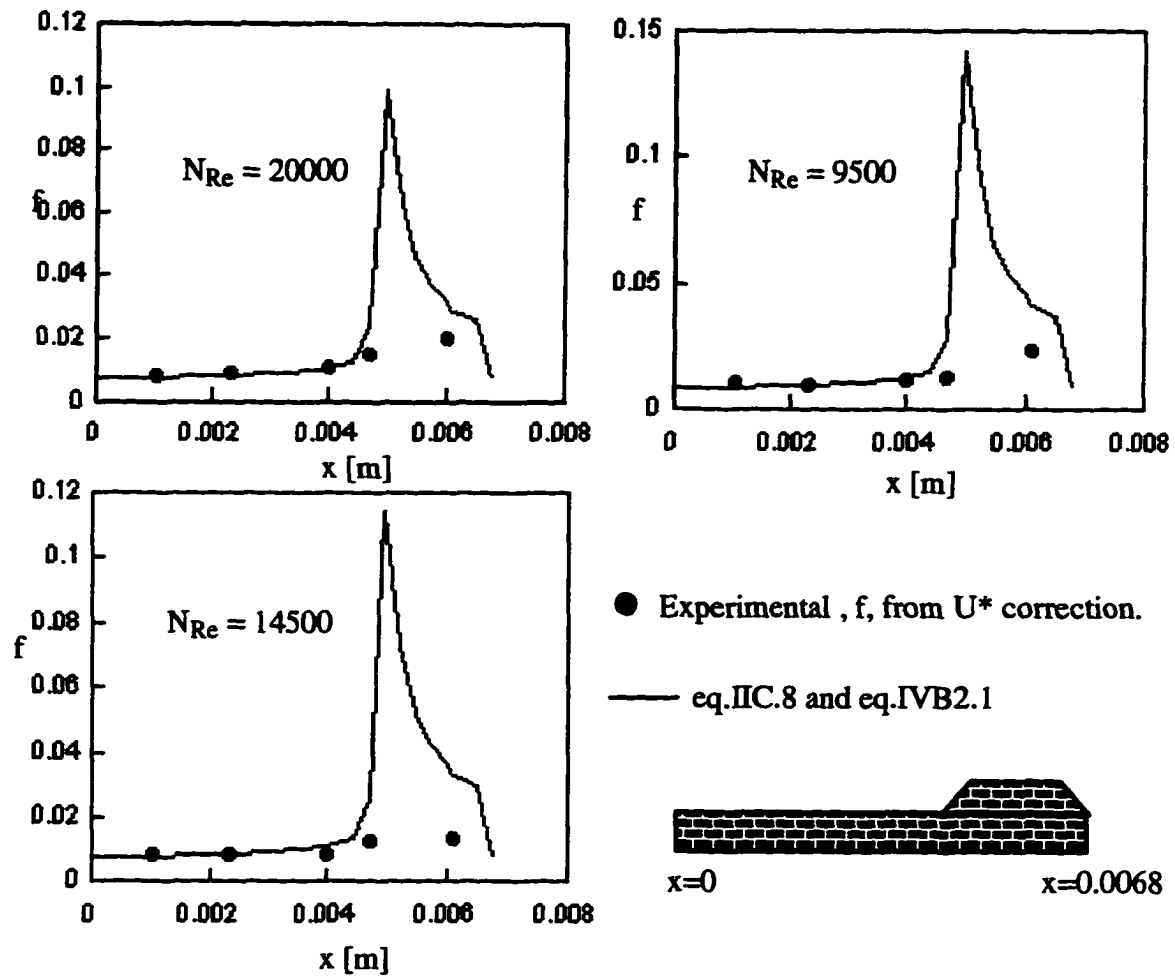
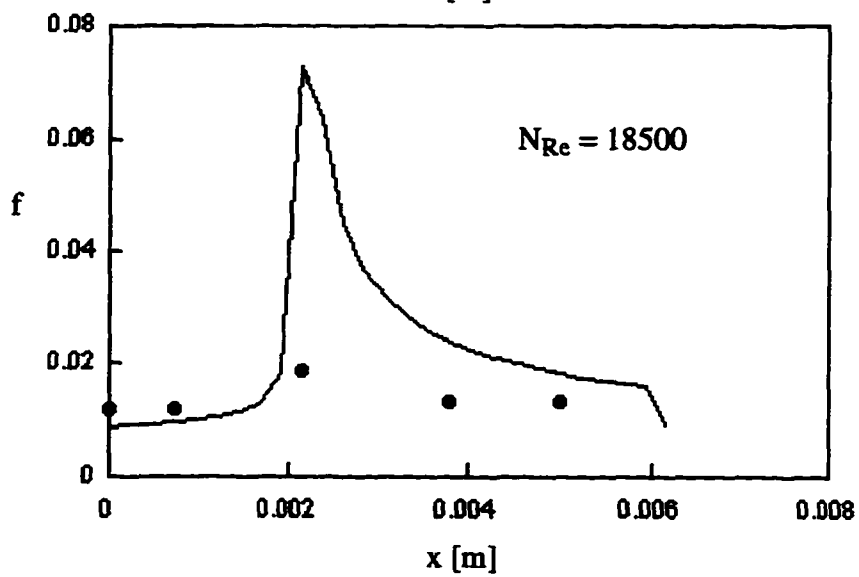
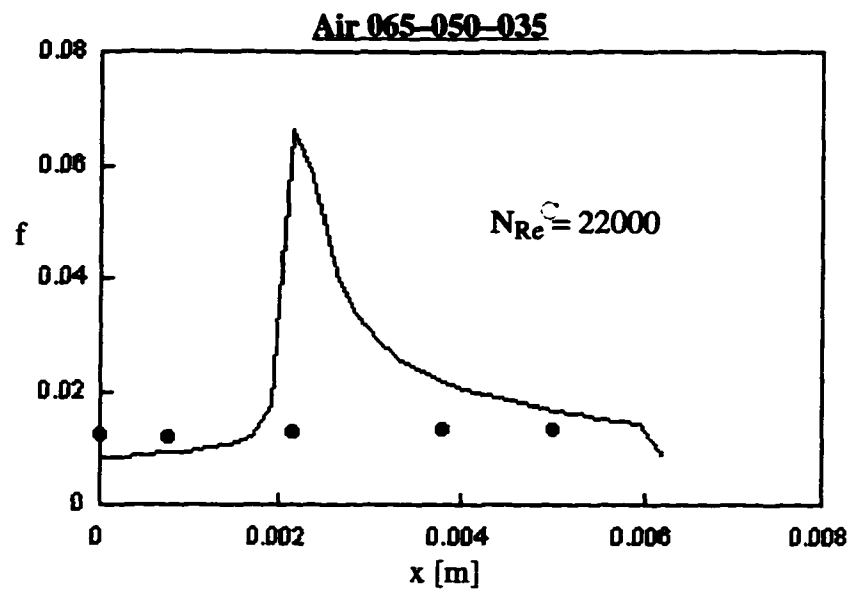


Figure IVB1.2



● Experimental , f, from  $U^*$  correction.

— eq.IIC.8 and eq.IVB2.1

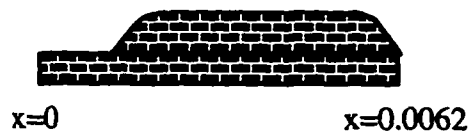


Figure IVB1.3

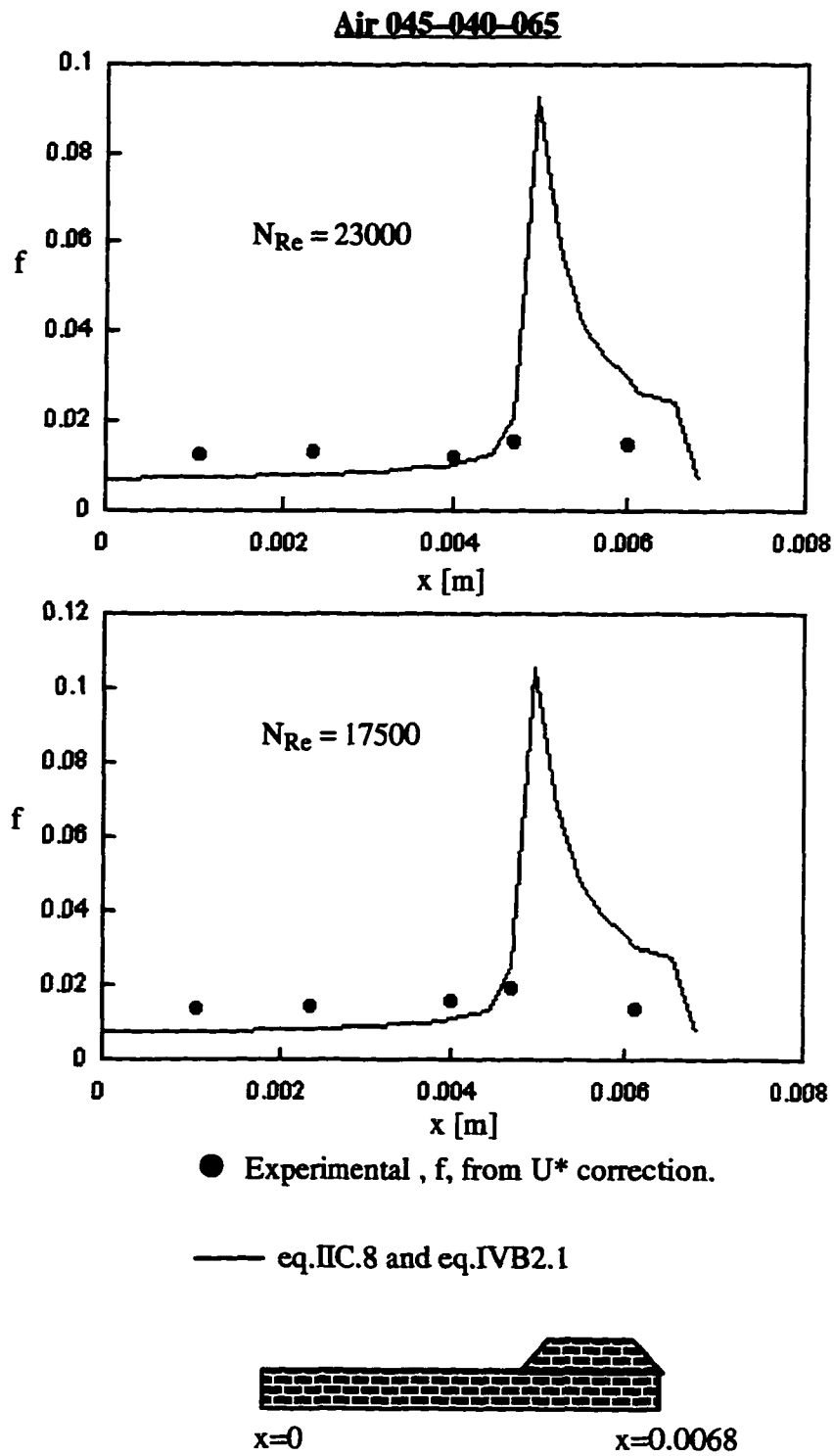
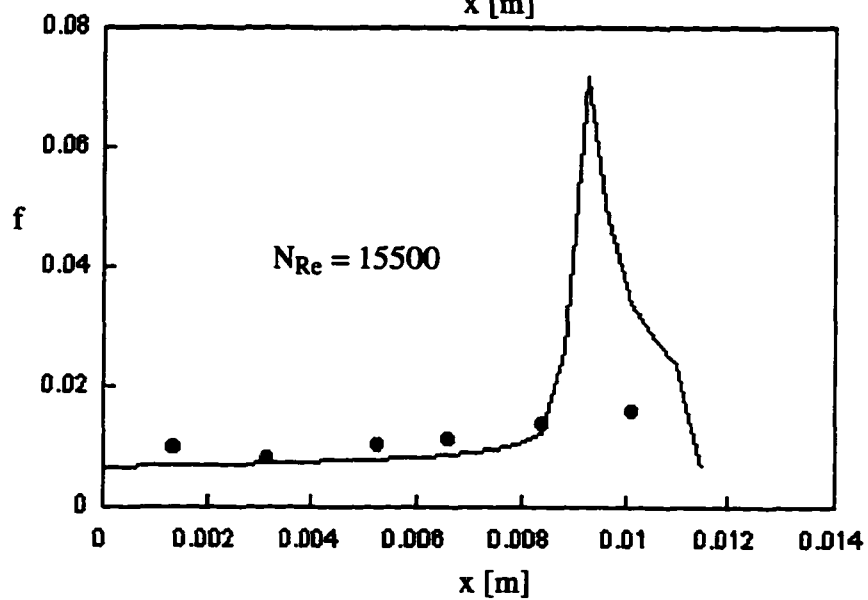
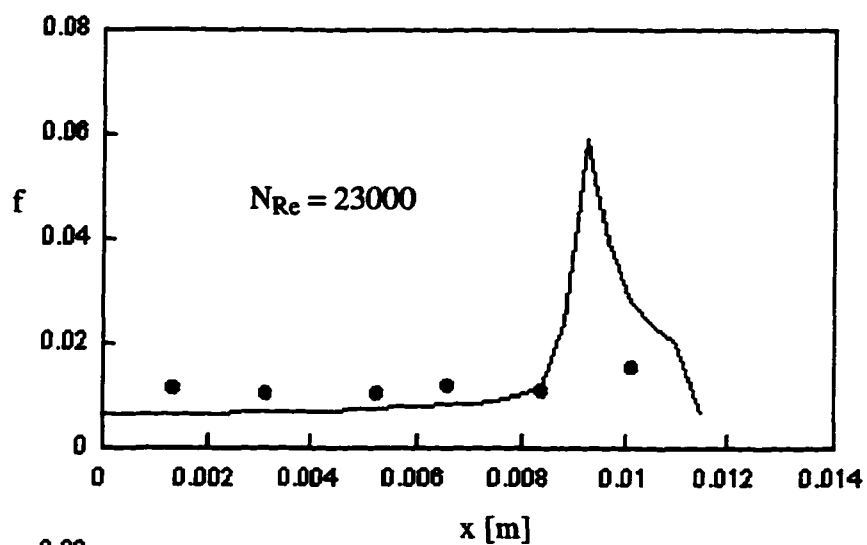


Figure IVB1.4

Air 040-040-035

● Experimental ,  $f$ , from  $U^*$  correction.

— eq.IIC.8 and eq.IVB2.1

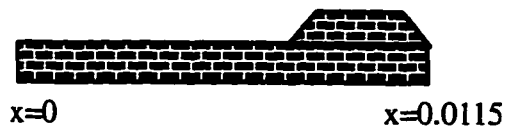


Figure IVB1.5

There is an apparent disagreement between the experimental friction factors and the theoretical formulation in Figures IVB2.1 to 5. The friction factors predicted by Eq. IVB2.1 and Eq. IIC.8 are descriptions of the friction phenomenon in the near wall region. On the contrary, the experimental friction factors calculated with Nikuradse's equation were calculated using a complete velocity profile from the wall to the center of the pipe. Because of this, the experimental points are representative of the friction phenomenon in a global scale. The Eq. IVB2.1 and Eq. IIC.8 are representative of the flow characteristics close to the wall. Probably the solution to the disagreement between the experiments and the theory would have been to modify the method of calculation of the experimental friction factors. The velocity profiles used with Nikuradse's equation should include only those points very close to the wall. In fact this approach was attempted. The local friction factors were calculated using only the velocities within 1 mm away from the pipe wall. This approach failed to show any difference in the values of friction factors calculated with the entire velocity profile. The reason for this was that the definition of the LDV measurements close to the wall was not enough to show a difference between those velocity points close to the wall and those in the core region. In other words, all the points of the velocity profiles were aligned with Nikuradse's equation for a given value of  $U^*$ . This value of  $U^*$  was the same for the points close to the wall than the points in the main flow. The slope of the line  $U_x / U^*$  remained constant for any position in the radial direction. The cause for this behavior could be attributed to the small values of the boundary layer thickness ( $\delta = 0.33$  mm Section IVA.1 ). For this boundary layer dimensions the LDV was at the limit of its sensitivity. Only one or two points were usually measured within this range not providing enough information about the flow behavior near the wall.

A better agreement between theory and experiments was found when the average friction factors calculated from integration of Eq. IVB2.1 and Eq. IIC.8 was compared with the average friction factors calculated from the experimental points. This agreement shows that the

theoretical distribution of  $f(x)$  did not have its experimental counterpart, however the average friction factor calculated from the theoretical distribution did.

The AFF was calculated using IIC.9 for the boundary layer and IVB2.2 for the cavity. The procedure was analogous to that one of AHTC in section IVA3. The definition of the OFF was:

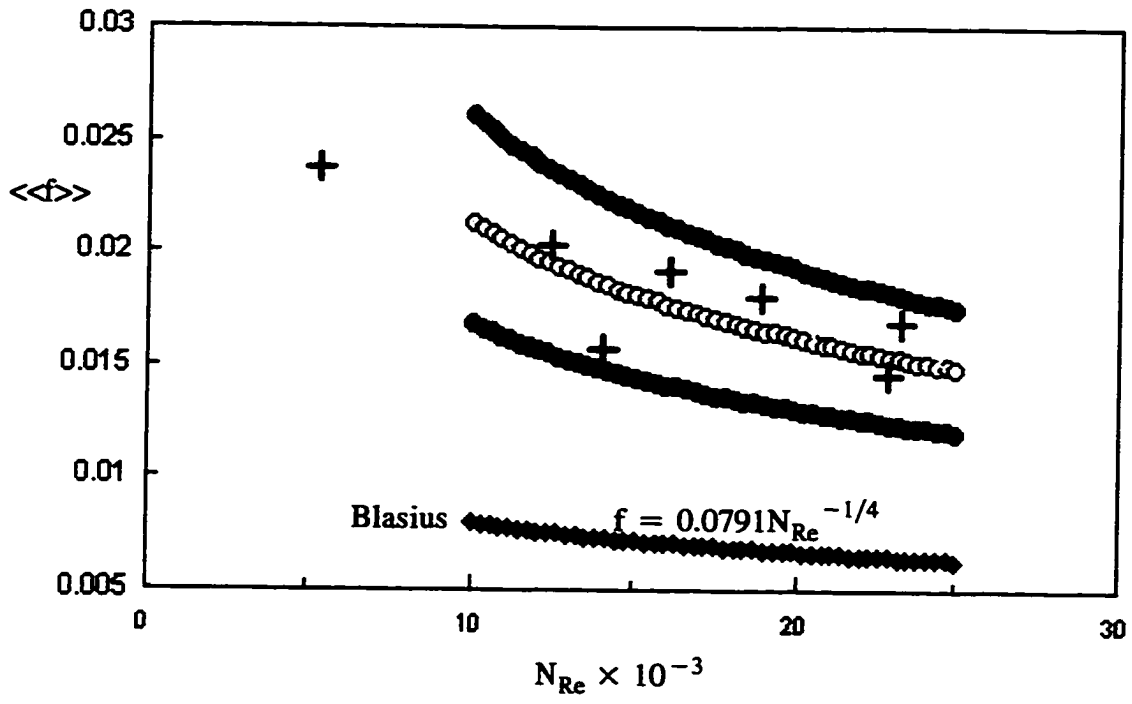
$$\llcorner f \gg = \frac{\langle f \rangle_{cv} l_s + \langle f \rangle_{bl} w}{l_o}$$

Replacing with IIC.9 and IVB2.2 :

$$\llcorner f \gg = \frac{0.0415 (N_{Re}^{lc})^{-\frac{1}{3}} l_s + 1.328 (N_{Re}^{lL})^{-\frac{1}{2}} w}{l_o} \quad \text{IVB2.3}$$

Figure IVB1.6 shows the  $\llcorner f \gg$  versus NRe for the three pipes and the average friction factors calculated from the experimental results. The correlation for smooth pipe of Blasius is included in the graph.





	Eq. IVB2.3	Experimental
065-050-035	●	+
045-040-065		
040-040-035	●	+

Figure IVB1.6

## V CONCLUSIONS AND RECOMMENDATIONS

The experiments carried out with liquid crystals (LC) allowed us to obtain the local distribution of heat transfer coefficients on top of a repeating unit. The LC technique proved to be an excellent way to obtain temperature profiles. It would have been extremely difficult, if not impossible, to measure with some other method the small differences in temperature that develop on top of the repeating unit. Also, the length in which these temperature profiles developed was so small that the alternative of using thermocouples would have been impossible. An important characteristic of the LC technique was the capability of amplification of the phenomenon of temperature distribution on top of a repeating unit. The LC on top of the repeating unit acted like an amplifier for heat flux between the solid of the repeating unit and the air. The reason for this behavior was the difference in thermal conductivity of steel with respect to the LC ( 1 : 500 ) and the comparative thickness of the LC coating to the steel repeating unit ( 1 : 50 ). If the temperatures would have been measured by any other method on top of the repeating unit, surely zero difference in temperature would have been found. A small difference in temperature through a highly conductive solid will not cause a variation of heat fluxes in the direction of flow or axial direction. However, a small temperature difference through a thin layer of quasi-insulating material like the LC will produce the distribution seen in the present work. A thin layer of low conductivity material conducts heat mainly in the , y, direction. The question that follows could be : what would have to be done if more accuracy is needed for smaller temperature differences? Probably the answer would be that prior to covering the surface of the highly conductive solid with LC, another insulating material could be coated on top of the highly conductive material ( i.e. polyethylene ) as long as it is a thin coating. The insulating material would ensure that the temperature profiles would have a wide distribution on the surface even

for high values of heat flux. This could be an important consideration for future experiments with Liquid Crystals.

In the computations of the local heat transfer coefficients it was decided to use a piecewise temperature profile over a smooth one. The reason for this choice was to avoid the numerical noises that were noticed in the first computations that were carried out. Many attempts were done to prevent the noisy profiles of local heat fluxes. The corners and abrupt changes on the repeating unit geometry were carefully rounded with splines and curves, the meshing of the mathematical domain was refined to the maximum that the software allowed with no favorable results. Only when a piecewise profile was used instead of the smooth one, the distribution of heat fluxes turned to be a smooth one. The reasons for this phenomenon are not clear yet. The only clear point is that, apparently, when the physical domain is described by a piece wise boundary, applying a smooth boundary condition on it, creates an overshooting of the solution at the corners.

The validity of the correlations that described the phenomenon of enhancement can be verified by comparison of the dimensionless numbers anticipated in section IIB with those of section IVA :

$$\ll N_{Nu} \gg = \frac{\langle N_{Nu}^I \rangle h + \langle N_{Nu}^{II} \rangle w + \langle N_{Nu}^{III} \rangle h + \langle N_{Nu}^{IV} \rangle (P - w - 2b)}{(P - 2b + 2h)}$$

$$\langle N_{Nu}^{Ic} \rangle = 0.015 \frac{1}{lc} (N_{Re}^{Ic})^{\frac{4}{3}} l_s + 0.1374 \frac{1}{w} (N_{Re}^{Iw})^{\frac{1}{2}} w$$

A careful observation shows that all the dimensionless variables of the dimensionless analysis are included in the correlations. Including  $N_{Pr}$  that is included in the pre-exponential factor of the BL correlation, through the dependency of  $\Theta'$  ( see section IIC) with the Prandtl number. From the values of  $\Theta'$  the order of magnitude of the temperature gradient at the boundary ( $dT/dy$ ) was estimated. This value was consistent with the differences in temperature that were used. In the case of the cavity correlation, it is probable that  $N_{Pr}$  is also included in the pre-exponential factor. However, this can not be proved since the CV correlation was obtained using a purely experimental approach and because the experiments of heat transfer were carried out only for air ( i.e. one value of  $N_{Pr}$  ). The difference found between the dimensionless analysis and the proposed solutions for BL and CV is in the characteristic length that defines the  $N_{Nu}$ . The characteristic length in all the regions of the dimensionless analysis was  $e$ , the rib height. In the results of the present work each correlation has its own characteristic length. For the BL it is the rib width  $w$ , the one that defines the  $N_{Nu}$ . In the cavity,  $l_c$ , is the characteristic length that defines the  $N_{Nu}$ . This result is more logical than assuming that regardless of which zone is analyzed, the rib height will be the characteristic length. It is much more logical to define  $N_{Nu}$  at the boundary layer region through the boundary layer length,  $w$ . In the case of the CV it is evident that the cavity length is more appropriate to define  $N_{Nu}$  than the rib height.

The effect of the angle  $\alpha$  was only present in the geometrical parameters and not as a variable in the correlations. This was because the approach of the present work was a two dimensional representation of a process that certainly happened in three dimensions. However, the effect of the angle  $\alpha$  is clearly seen in the evolution of the geometric variables of a repeating unit. The present work analyzed pipes with  $35^\circ < \alpha < 65^\circ$ . It needs to be determined if the correlations will hold for different values of  $\alpha$  than those that were analyzed. The correlations of the present work have  $\sin(\alpha)$  as the geometric correction for angle. In the work of Webb et

al. ( $\alpha / 45$ ) could be considered as the geometric correction. The application of the present correlations to values of  $\alpha < 35^\circ$  or  $\alpha > 65^\circ$  could be an interesting subject for future research.

The basis of the separation of the  $h_x$  profiles into two regions, was the maximum found at the leading edge of the rib. This maximum was indicating that in all three cases analyzed the reattachment point was somewhere at the leading edge of the rib. This indicates that a maximum in the local heat transfer coefficient is not a sharp point but a region of smooth inflexion on the  $h_x$  profiles. The reason for this is the capability of heat conduction to spread the heat along the surface preventing the existence of sharp profiles at the maximum.. In the present work the position of  $x=0$  was taken to be the one that made the correlation for cavity to be asymptotic to the boundary layer correlation.

If the value of pitch is increased the boundary layer will reattach between the ribs and not at the leading edge of the rib. Under this circumstances a maximum of  $h_x$  will be found at the point of reattachment. However, it is probable that another local maximum could be found at the leading edge of the rib too. In this case, two maximums will be expected: one at the point of reattachment between the ribs and another at the leading edge of the rib. There is very little information about what happened with the flow after the reattachment point. If a new boundary layer develops in the valley it will have to collide with the inclined face of the downstream rib. After this collision it is probable that that a new BL could develop on top of the rib. If that is the case, a similar situation as at the point of reattachment can be found. When the BL starts developing on top of the rib, it can be as thin as at the reattachment point. In fact the BL thickness could be zero. The possibility of two local maxima can be explored. If two maxima exist, the relative value of one maximum with respect to the other will be reflected in the computations. If they have the same order of magnitude probably two peaks will be found in the computations of  $h_x$ . If one of them is considerably higher than the other the computations will show only one. The reason for this is that conduction will spread the heat around the local maximum of lower

value. The largest local maximum will be the one that will shape the profiles of  $h_x$ . This is only a hypothesis that is intended to prove that results similar to the present work could be found if pipes with wider pitches are measured. This result may suggest that heat conduction could be hiding local values of  $h_x$  by homogenization of the heat flux distribution. None of the existing correlations take into consideration the phenomenon of conduction. This assumption can be extended to the point, as it is done in the analysis of fin efficiency, that not the  $N_{Nu}$  but the number of Biot ( $N_{Bi}$ ) could be the representative dimensionless number of the phenomenon:

$$N_{Nu} = \frac{e h}{k_{fluid}} \qquad N_{Bi} = \frac{e h}{k_{solid}}$$

The order of magnitude of both numbers is:

$$O(N_{Nu}) = \frac{0.001 \times 50}{0.0262} = O(1)$$

$$O(N_{Bi}) = \frac{0.001 \times 50}{50} = O(10^{-3})$$

This results could suggest that an analysis of rib efficiency could be carried out to analyze the competition of the process of conduction with respect to convection. Both dimensionless numbers describe the same phenomenon. However, depending on their relative value, convection will prevail over conduction or *vice versa*. This theoretical analysis is suggested for future works that will be done on structured promoters.

From the process of coupling of the two flow regions eq.IVA3.2 was derived. Within a reasonable margin of error, eq. IVA3.2 predicted the values of the AHTC for both the models analyzed in the present work and for others provided by the manufacturers. Probably this was the most important achievement of the present work. A global phenomenon was separated into individual and theoretically based problems. Equation IVA3.4 proved that the two schemes

could be combined to describe the phenomenon in its totality. These correlations were not the product of curve fitting but the application of well described phenomena like developing boundary layer equations and experimental correlations for cavity flow, that have been derived by other researchers.

The experimental results of local heat transfer coefficients on top of the rib were treated as a developing boundary layer. The experiments and the analytical description of the phenomenon were in very good agreement. The extension of this approach to wider ribs could be done with the precaution to keep the values of  $P$  within the range of the present work. If the pitch is increased the reattachment point may or may not fall at the leading edge of the rib. If the rib width became too wide, and if the approach of developing BL is still valid, a new type of flow could develop on top of the rib. The approach of laminar boundary layer of this work must consider the fact that if the rib width is long enough, a turbulent boundary layer would develop down stream of the laminar one. It would be very interesting to include this third flow regime. For wider values of rib width it would be interesting to apply a cavity flow, developing laminar BL and developing turbulent BL.

A similar, but more empirical approach, was performed on the experimental values of  $h_x$  on the cavity surface. The correlation of Seban described successfully the behavior of  $h_x$  within the cavity. The existence of a free shear layer was verified through the measurements of turbulence intensities within the cavity. This measurements showed a maximum of turbulence intensity at the point where the free shear layer was expected. The free shear layer was the zone that separated the main flow from the cavity flow. This evidence support the fact that the characteristic length of the cavity was measured backwards. This means, the variable  $x_{CV}$  was zero at the leading edge of the rib and evolved upstream until reaching the first rib. If the flow between the cavity was in fact a recirculating one, the velocities near to the cavity bottom had to be backwards. This flow on the cavity surface was considered to be a turbulent boundary layer.

This turbulent boundary layer flow is in a direction opposite to the main stream on top of the cavity surface. The existence of a free shear layer was verified with the results of LDV that supports the existence of a recirculating region.

An original method of calculation of friction factors was developed from the measurements carried out with the Laser Doppler Velocimeter. The  $U_x$  velocity profiles were compared with the rough function  $B(e U^*/\nu)$  of Nikuradse by adjusting the value of  $U^*$ . The friction factors were calculated with this adjusted value of  $U^*$ . In this manner a series of values of friction factors were calculated along the repeating units. There was very little difference between this friction factors and the results were an almost constant profile of friction factors on top of the repeating units. The constant values of friction factors at different positions on the repeating unit was attributed to the high kinetic energy of the main stream. The energy of dissipation of the main flow prevented the friction to have distinctive values on top of the repeating unit. Finally, the corresponding equations for boundary layer and cavity flow were compared with the resulting friction factors it was seen that the order of magnitude was in agreement, however the shape of the theoretical values was different than that of the experimental values.

The correlations found for average heat transfer coefficients and friction factors can be used to define an optimum pipe model. Given the operating conditions such as  $N_{Re}$ , a pipe can be designed to achieve a desired heat transfer enhancement with a minimum of friction losses. In other words, eq IVA3.4 and IVB2.3 can be used as the basis for a new pipe geometry of improved performance.